

IEEE

microwave

for the Microwave & Wireless Engineer



MAGAZINE

Volume 22 • Number 2 • February 2021

Passive Component Technologies and Applications



IEEE Transactions on Microwave Theory and Techniques

Special Issue on

Microwave and Millimeter-Wave Communication and Sensor Systems

NEW Submission Date: 26 February 2021, Publication Date: October 2021

Motivation

The aim of this Special Issue is to publish technical papers in microwave and millimeter-wave communication and sensor systems. In recent years, we have seen a strong resurgence in such systems due to 5G and satellite communications, automotive radars, precise location services, UAV tracking, imaging radars, STAR (simultaneous transmit and receive systems also known as self-duplex), power amplifiers with digital pre-distortion, antenna tuning with closed loop functions, etc. Also, silicon chips are becoming more complex with multiple transmit and receive beamforming channels, up and down-conversion mixers, synthesizers, ADCs and DACs and even digital signal processing decision circuitry all on the same die. The silicon (and III-V front-end) solutions can be considered as stand-alone and are connected to antennas (or antenna arrays) for operation. For such complex systems, it is not required to know the detailed operation of every circuit or component, and it is more important to look at the solution from a systems perspective, such as co-design of the RF blocks with the antennas and with the DSP back-end, and the decision algorithms for the respective application areas. Also, calibration and test of such complex systems is critical, and novel techniques are needed to reduce the calibration cost which can lead to a reduction in system cost. The increased impact of microwave and millimeter-wave systems is noticeable throughout society, especially in 5G communications, automotive radars, safety/security applications, and in bio-medical sensors.

Topics of interest to be covered by the Special Issue include, but are not limited to

- *Systems and system-level demonstrations for communications and radar sensing*, including but not limited to: active and passive phased arrays using different beamforming technologies, MIMO arrays, repeaters, self-duplex and active nulling arrays, polarization diversity, closed-loop antenna tuning solutions, dual- or multi-band arrays, reconfigurable arrays, calibration and test techniques, etc. Applications for 5G, point-to-point links, SATCOM, automotive radars, position sensing, and other standards are especially welcome.
- *System-level integrated circuits and/or sub-systems using multiple chips*, including but not limited to: communication and radar chips with multi-channel transceivers, power amplifiers with wideband digital pre-distortion and envelope tracking, signal cancelling chips for self-duplex systems at the RF, IF and DSP level, and other complex systems on a chip. Circuits using solid-state (BiCMOS, SiGe, CMOS, SOI CMOS, GaAs, GaN and any combination) and non-solid-state technologies (RF MEMS, BST, liquid crystal, phase-change, etc.) are solicited.
- *Packaging and module technologies*, including but not limited to: complex packaging design for multifunction wideband systems, high power/thermal considerations, module technologies for receivers and transmitters, antennas-in-package and wafer-scale systems.
- *Review papers*, including but not limited to: papers summarizing the state of the art in automotive radars, SATCOM, 5G, point-to-point links, sensing systems, power amplifier digital predistortion, etc. are also encouraged. Potential authors should contact the editors to discuss their submission and to get approval for this special category.

Authors must consult the link <https://www.mtt.org/author-information-transactions/> for submission instructions.

Guest Editors

Prof. Gabriel M. Rebeiz
University of California, San Diego, USA
rebeiz@ece.ucsd.edu

Prof. James F. Buckwalter
University of California, Santa Barbara, USA
buckwalter@ece.ucsb.edu



DC TO MMWAVE

Preferred by 20,000+

More than Just a Supplier

Selection and Solutions

- 27 product lines from one source
- 7500+ models in stock and growing
- Coverage from VHF to mmWave
- Custom components, integrated systems and test solutions with fast turnaround

Peace of Mind

- Award-winning quality excellence
- Easy troubleshooting and RMA process
- Supply chain security through the life of your system—no EOL target

Service

- Global presence, local service
- Accessible engineering and support
- Same-day shipping and on-time delivery
- Short lead times and low minimums

Constant Innovation

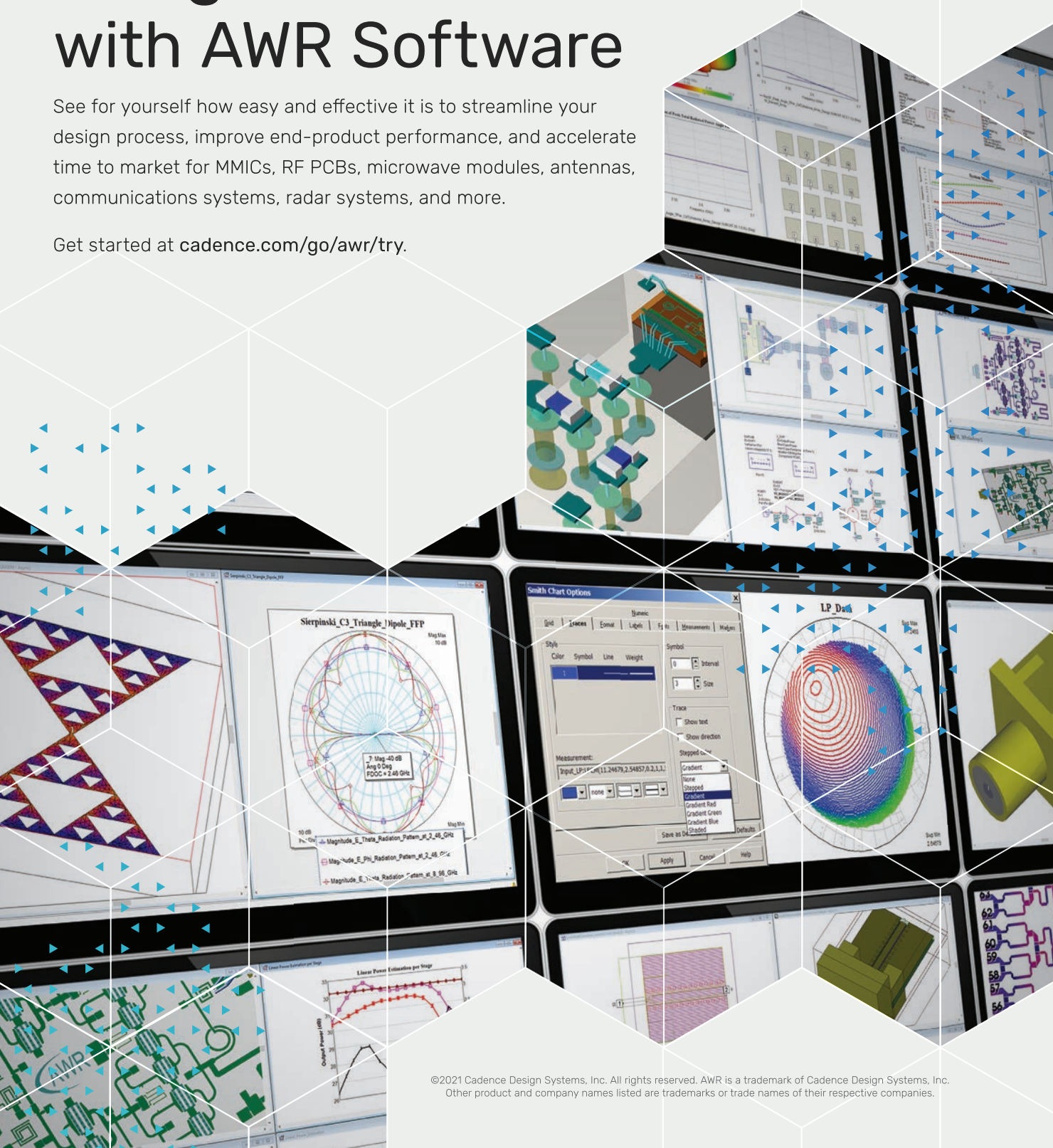
- Relentless investment in new products and design capabilities
- 400+ catalog introductions per year
- Patented technologies

cadence®

Design Smarter with AWR Software

See for yourself how easy and effective it is to streamline your design process, improve end-product performance, and accelerate time to market for MMICs, RF PCBs, microwave modules, antennas, communications systems, radar systems, and more.

Get started at [cadence.com/go/awr/try](https://www.cadence.com/go/awr/try).



Editor

Robert H. Caverly, Villanova University, USA,
microwave.editor@ieee.org

Assistant Editor

Sharri Shaw, JWM Consulting LLC,
microedt@outlook.com

Associate Editors

Nuño Borges Carvalho, University of Aveiro,
Portugal, nbcarvalho@ua.pt

Simone Bastioli, RS Microwave, New Jersey,
USA, sbastioli@rsmicro.com

Chia-Chan Chang, National Chung-Cheng
University, Taiwan, ccchang@ee.ccu.edu.tw

Ali Darwish, American University in Cairo,
Egypt, ali@darwish.org

Christian Fager, Chalmers University of Technology,
Sweden, christian.fager@chalmers.se

Jianguo Ma, Guangdong University of
Technology, China, mjg@gdut.edu.cn

Alfy Riddle, Quanergy Systems, Inc., Sunnyvale,
California, USA, alfred.riddle@quanergy.com

Luca Roselli, University of Perugia, Italy,
urlofi@tin.it; luca.roselli@unipg.it

Kamal Samanta, Sony Europe, U.K.,
kmlsamanta@googlemail.com

Almudena Suarez, University of Cantabria,
Spain, almudena.suarez@unican.es

Anding Zhu, University College Dublin,
Ireland, anding.zhu@ucd.ie

Columns and Departments

MicroBusiness

Fred Schindler,
m.schindler@ieee.org

Health Matters

James C. Lin, University of Illinois-Chicago,
USA, lin@uic.edu

Microwave Surfing

Rajeev Bansal, University of Connecticut,
USA, rajeev@engr.uconn.edu

Book Reviews

James Chu, Kennesaw State University,
Georgia, USA, jameschu@bellsouth.net

Education Corner

Rashaunda Henderson, University of Texas
Dallas, USA, mh072000@utdallas.edu

Women in Microwaves

Wenquan Che, Nanjing University of Science
and Technology, China, yeeren_che@163.com

Membership News

Bela Szendrenyi, Advantest, California, USA,
bela.szendrenyi@advantest.com

New Products

Ken Mays, The Boeing Company, Washington,
USA, microwave.newproducts@ieee.org

In Memoriam Contributions

Jerry Hausner, j.hausner@ieee.org

Ombuds Officer

Edward C. Niehenke, Niehenke Consulting,
e.niehenke@ieee.org

IEEE Periodicals Magazines Department

Mark Gallaher, Managing Editor

Geraldine Krolin-Taylor, Senior Managing Editor

Janet Dudar, Senior Art Director

Gail A. Schnitzer, Associate Art Director

Theresa L. Smith, Production Coordinator

Felicia Spagnoli, Advertising Production Manager

Peter M. Tuohy, Production Director

Kevin Lisankie, Editorial Services Director

Dawn Melley, Senior Director, Publishing Operations

Advertising Sales

Mark David, Director, Business Development—
Media & Advertising
+1 732 465 6473, fax +1 732 981 1855



for the Microwave & Wireless Engineer

MAGAZINE

Volume 22 • Number 2 • February 2021 • ISSN 1527-3342

features

16 Negative Group Delay Circuits and Applications

Feedforward Amplifiers, Phased-Array Antennas, Constant Phase Shifters, Non-Foster Elements, Interconnection Equalization, and Power Dividers
Jian-Kang Xiao, Qiu-Fen Wang, and Jian-Guo Ma

33 Waveguide Components Based on Multiple-Mode Resonators

Advances in Microwave Multiple-Mode Waveguide Components, Including Multiplexers, Three-State Diplexers, Crossovers, and Balanced/Unbalanced Elements
Sai-Wai Wong, Jing-Yu Lin, Yang Yang, Zai-Cheng Guo, Lei Zhu, and Qing-Xin Chu

46 Tunable Balanced Power Dividers

An Overview of Recently Developed Balanced Power Dividers and Couplers With Fixed and Tunable Functions
Feng Lin, Wenjie Feng, and Xiangguan Tan



IEEE Microwave Theory and Techniques Society

The IEEE Microwave Theory and Techniques Society (MTT-S) is an organization, within the framework of the IEEE, of members with principal professional interests in the field of microwave theory and techniques. All Members of the IEEE are eligible for membership in the Society. Information about joining the IEEE or the Society is available on the web, <http://www.ieee.org/membership>.

MTT-S AdCom

The Society is managed by an Administrative Committee (AdCom) consisting of 22 elected members of the Society plus additional ex-officio members as provided in the MTT-S Constitution and Bylaws, which is available on the web, <http://www.mtt.org>.

Officers

President: Gregory Lyons
President-Elect: Rashaunda Henderson
Secretary: Joseph Bardin
Treasurer: Maurizio Bozzi

Elected Members

Alaa Abunjaileh	Rashaunda Henderson
Scott Barker	Sherry Hess
Maurizio Bozzi	Sridhar Kanamaluru
Nuno Borges Carvalho	Dietmar Kissinger
Robert H. Caverly	Gregory Lyons
Goutam Chattopadhyay	Raafat Mansour
Wenquan Che	Daniel Pasquet
Terry Cisco	Ajay Poddar
Kamran Ghorbani	Jose Rayas-Sanchez
Xun Gong	Peter Siegel
Ramesh Gupta	Anding Zhu

Ex-Officio Members

Immediate Past Presidents: Alaa Abunjaileh* (2020)
Dominique Schreurs* (2018–2019)
Dylan Williams* (2017)

Honorary Life Members*
(max. three votes):

Józef Modelski
John T. Barr IV
Tatsuo Itoh
Richard Sparks
Peter Staecker

MTT-S Publications

IEEE Trans. Microwave Theory & Techniques Editor: Jianguo Ma*
IEEE Microwave & Wireless Components Letters Editor: Thomas Zwick*
IEEE Microwave Magazine Editor: Robert H. Caverly
IEEE Trans. Terahertz Science & Technology Editor: Imran Mehdi*
IEEE Journal of Electromagnetics, RF, and Microwaves in Medicine and Biology Editor: Yongxin Guo
IEEE Journal on Multiscale and Multiphysics Computational Techniques Editor: Costas Sarris
IEEE Journal of Microwaves Editor: Peter Siegel

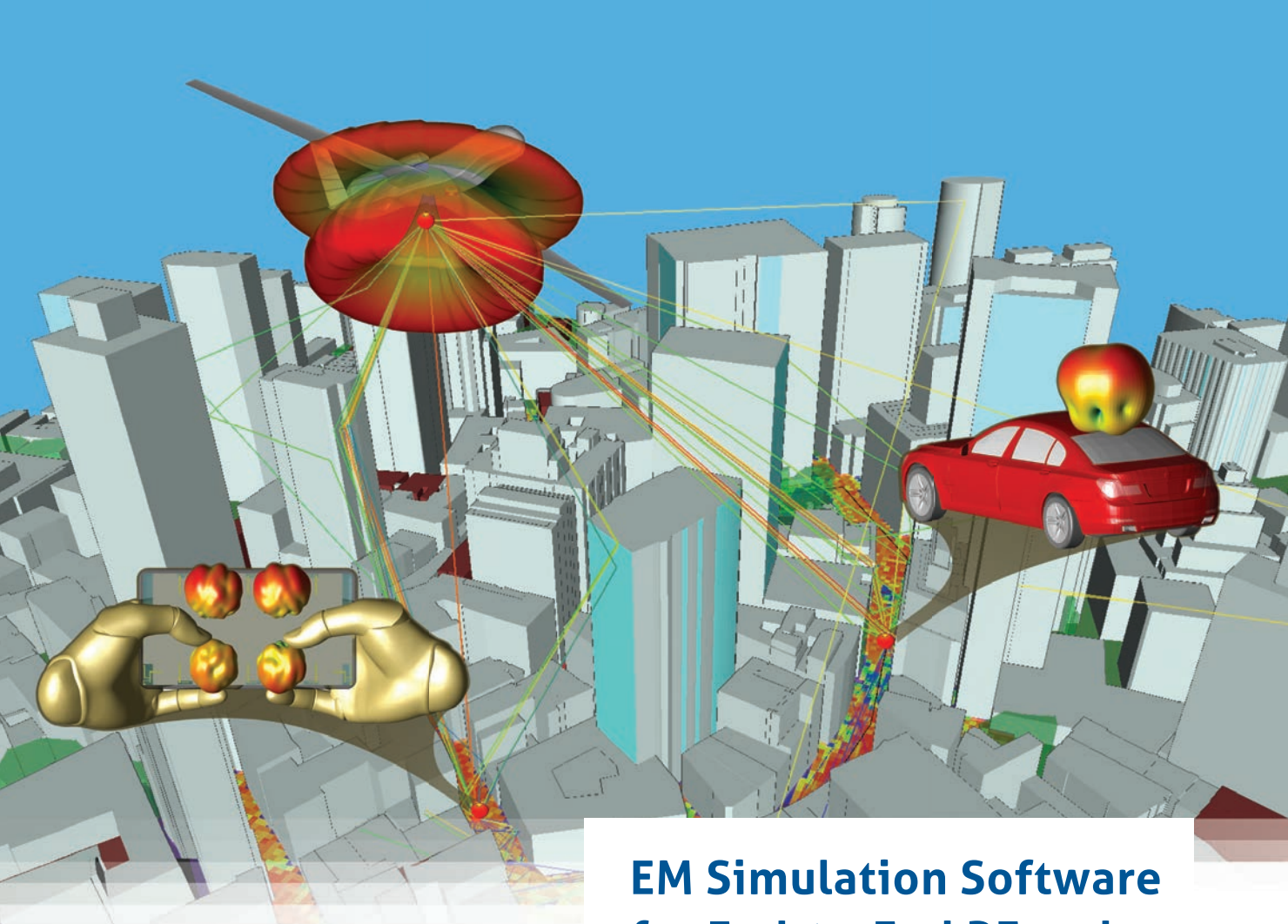
*Indicates voting AdCom ex-officio member

IEEE Microwave Magazine (ISSN 1527-3342) (IEMMFF) is published 12 times a year by the Institute of Electrical and Electronics Engineers, Inc. Headquarters: 3 Park Avenue, 17th Floor, New York, NY 10016-5997 USA. Responsibility for the contents rests upon the authors and not upon the IEEE, the Society, or its members. IEEE Service Center (for orders, subscriptions, address changes): 445 Hoes Lane, Piscataway, NJ 08854. Telephone: +1 732 981 0060, +1 800 678 4333. Individual copies: IEEE members US\$20.00 (first copy only), nonmembers US\$37.00 per copy. Subscription rates: Subscriptions for Society members are included with membership dues. Nonmember subscription rates available upon request. Copyright and reprint permissions: Abstracting is permitted with credit to the source. Libraries are permitted to photocopy beyond the limits of U.S. Copyright law for the private use of patrons those articles that carry a code at the bottom of the first page, provided the per-copy fee is paid through the Copyright Clearance Center, 222 Rosewood Drive, Danvers, MA 01923 USA. For other copying, reprint, or republication permission, write Copyrights and Permissions Department, IEEE Service Center, 445 Hoes Lane, Piscataway, NJ 08854 USA. Copyright © 2021 by the Institute of Electrical and Electronics Engineers, Inc. All rights reserved. Periodicals postage paid at New York, N.Y., and at additional mailing offices. Ride along enclosed. Postmaster: Send address changes to IEEE Microwave Magazine, IEEE Operations Center, 445 Hoes Lane, Piscataway, NJ 08854 USA. Canadian GST #125634188
PRINTED IN THE USA

Digital Object Identifier 10.1109/MMM.2020.3035861

columns & departments

- 6 From the Editor's Desk
 - Robert H. Caverly*A Look at the February Issue*
- 8 President's Column
 - Gregory Lyons*Administrative Committee Experience*
- 12 MicroBusiness
 - Fred Schindler*Travel, Revisited*
- 14 Microwave Surfing
 - Rajeev Bansal*A Moonshot?*
- 58 Application Notes
 - Zubair Ahmed*Revisiting the Binomial Multisection Transformer*
- 70 Book/Software Reviews
 - Alfy Riddle*CMOS Loves 5G*
- 72 Education News
 - Robert H. Caverly, Michael C. Hamilton, and Rashaunda Henderson*Continuing Our IEEE MTT-S Webinar Series*
- 76 Enigmas, etc.
 - Takashi Ohira*Turn-On Surge*
- 78 Conference Calendar



EM Simulation Software for End-to-End RF and Wireless Design



Remcom's products work together to streamline the design of complex devices and wireless communication systems.

- High frequency antenna modeling for intricate devices
- Wireless communication and 5G network planning
- Massive MIMO beamforming and fixed wireless access
- Drive test simulation of automotive radar sensors
- Remcom's Simulation Platform unites WaveFarer® and XFDTD® in a common interface

Subscribe to receive product updates | www.remcom.com/communications >>>



From the Editor's Desk

A Look at the February Issue

■ Robert H. Caverly

Welcome to the February issue of *IEEE Microwave Magazine*. Around the time you receive this issue in mid-January, both IEEE Radio and Wireless Week and the European Microwave Week series of conferences will be completed (or nearly so). We then look forward to the IEEE Microwave Theory and Techniques Society (MTT-S) flagship conference, the International Microwave Symposium (IMS) and International Microwave Week, 6–11 June 2021, in Atlanta, Georgia. In fact, a short preview of IMS can be found within this issue. Between now and June, there are a number of smaller conferences scheduled, and our “Conference Calendar” at the end of the magazine summarizes those events.

In addition to conference information, the February issue is devoted to articles covering various passive component technologies and their applications. These articles are from various researchers in the field and are separate from our MTT-S technical

Robert H. Caverly (rcaverly@villanova.edu) is with Villanova University, Villanova, Pennsylvania, USA.

Digital Object Identifier 10.1109/MMM.2020.3037385
Date of current version: 11 January 2021



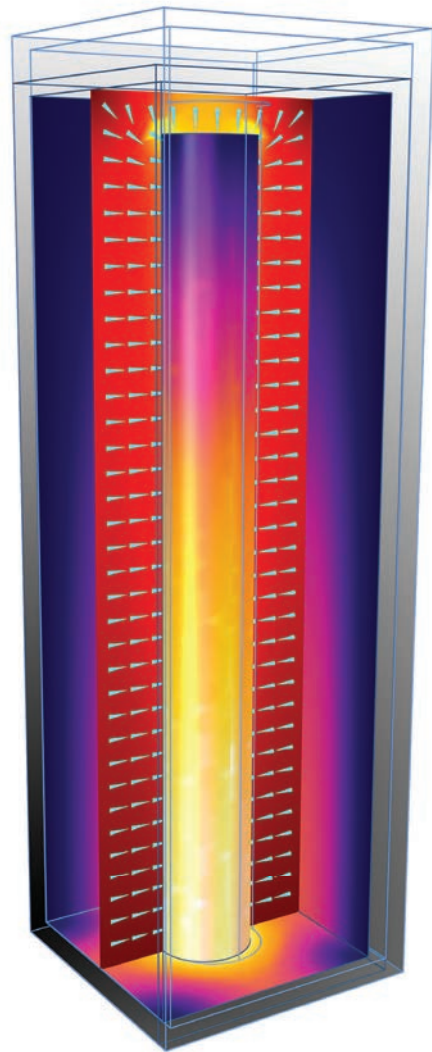
committee (TC) focus issues, of which we have a number planned over the next several months. If you have thought about writing a technology overview article, please consider *IEEE Microwave Magazine* as a publication to showcase your work. You do not have to be part of a TC focus issue to publish in the magazine.

The first of three technical features this month is “Negative Group Delay Circuits and Applications,” by Xiao et al.

The phase characteristics of filters and other multiport networks are often a secondary performance metric when designing these circuits, with more emphasis placed on magnitude properties, such as insertion or return loss or gain. However, the overall circuit performance in terms of delays and distortion increases with positive group delay behavior, and, to compensate

(continued on page 15)

In 1 design, both electrothermal effects and structural deformation are at play.



Visualization of the thermal expansion, electric field, and surface current patterns in a microwave cavity filter.

Microwave transmitters rely on filters to maintain a desired frequency output, but thermal drift can affect their operation. In order to optimize the design of these components, engineers need to predict their performance under real-world conditions. Multiphysics modeling can be used to evaluate the electrothermal and structural effects of microwave filters — simultaneously.

The COMSOL Multiphysics® software is used for simulating designs, devices, and processes in all fields of engineering, manufacturing, and scientific research. See how you can apply it to microwave designs.

comsol.blog/microwave-filters



President's Column

Administrative Committee Experience

■ Gregory Lyons

This month, it is my pleasure to introduce you to our president-elect for 2021, Rashaunda Henderson, as well as three IEEE Microwave Theory and Techniques Society (MTT-S) Administrative Committee (AdCom) members—Wenquan (Cherry) Che, Goutam Chattopadhyay, and Nuno Borges Carvalho—who were re-elected to a second three-year term (2021–2023) during our fall (now designated AM3) AdCom elections in September 2020. They have all provided a brief biography and a statement of their perspectives on the MTT-S. The perspectives of these experienced AdCom members are important because it is our AdCom that keeps the MTT-S healthy and moves it in new directions for the benefit of our overall Society membership.

The MTT-S AdCom voting membership consists of elected and ex-officio members. There are typically 21 elected members divided into groups



©SHUTTERSTOCK.COM/DANLEAP

of seven, each serving staggered three-year terms. Starting in 2019, two of the seven for each three-year term are elected by the MTT-S membership at large (previously, only one was). The remaining five for each term are elected by the MTT-S AdCom.

There are term limits for elected AdCom members of three three-year terms, for a total of nine years. Ex-officio members of the AdCom include the three most recent past presidents, honorary life members of the AdCom, and the editors-in-chief of our publications.

The complete organization of the AdCom can be found on our website at <https://www.mtt.org/administrative-committee-officers>.

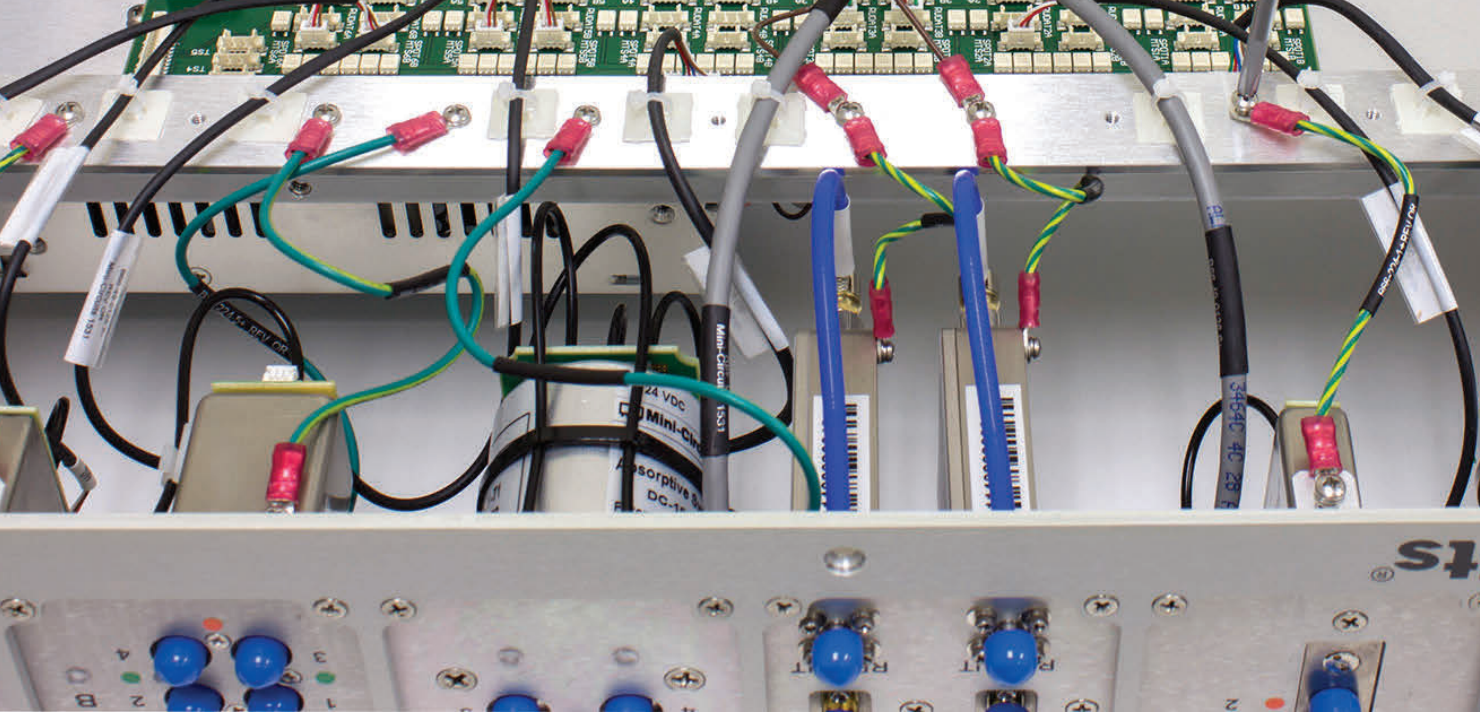
The MTT-S is a very active IEEE Society. If you would like to get involved as a volunteer in the MTT-S, fill out a contact form at <https://www.mtt.org/connectme>, and we will make sure you get connected.

Rashaunda M. Henderson

Rashaunda M. Henderson (Figure 1) received the B.S.E.E. degree with highest honors from Tuskegee University, Alabama, in 1992. She received the M.S. and Ph.D. degrees in electrical engineering from the University of Michigan, Ann Arbor, in 1994 and 1999, respectively. From 2000



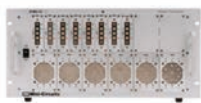
Gregory Lyons (g.lyons@ieee.org), is with Lincoln Laboratory, Massachusetts Institute of Technology, Lexington, Massachusetts, USA.



DC TO 50 GHz

Test Solutions

Components, Systems and Accessories



User-Assembled

Leverage our wide selection of in stock components for total flexibility to build your own system. We'll help you choose the right hardware. You take it from there.

Pre-Built Modular

Configure our flexible, pre-built modular chassis structures with your choice of routing and attenuation hardware for delivery as fast as two weeks. Plug and play GUI and API included.

Custom Systems

Put our full design and manufacturing capability to work for you to build complex custom systems with bespoke control software tailored to your unique test setup—scalable from design to production.

to 2007, she was an R&D device engineer at Freescale Semiconductor, Inc. (formerly Motorola Semiconductor Product Sector) in Tempe, Arizona, working in the microwave and mixed-signal technology labs for wireless embedded systems. In fall 2007, she joined the University of Texas at Dallas in Richardson, Texas, where she is an associate professor. She is cofounder of the High-Frequency Circuits and Systems Laboratory, which facilitates millimeter-wave design and the development of components, circuits, and integrated packages and antennas for communication systems. She has authored/co-authored more than 90 journal and conference papers/presentations in the field of microwave circuits and electronic packaging for high-frequency applications.

President-Elect Perspectives

I aspire to lead the MTT-S into this new decade as we face a world that has dramatically changed as a result of the pandemic. Due to the global shutdown, we all clearly understand our dependence on the advances and infrastructure that have been afforded us by microwave theory and technology.

Due to the global shutdown, we all clearly understand our dependence on the advances and infrastructure that have been afforded us by microwave theory and technology.

This pause in our normal way of doing things has also created opportunities to explore how the MTT-S can make contributions in health care, aerospace, safety, and security. I look forward to

working with the MTT-S AdCom to continue to maintain our relevance and seek ways to inspire and educate today's youth and young professionals. It is through our continued efforts to collaborate with other Societies and maintain a global presence that we will succeed and develop pathways allowing us to grow. In spite of what it looks like today, the best is yet to come!

Wenquan (Cherry) Che

Wenquan (Cherry) Che (Figure 2) received the B.Sc. and M.Sc. degrees from Nanjing University of Science and Technology in 1990 and 1995, respectively, and the Ph.D. degree from City University of Hong Kong (CityU), China, in 2003. She was a research assistant with CityU in 1999, a visiting scholar with the Polytechnique de Montréal of Canada in 2002, and a Humboldt Research Fellow at the Technische Universität München from 2007 to 2008. She is currently a

professor at the South China University of Technology. She has published more than 250 international journal articles. Her research interests include microwave circuits and antenna technology. She has received numerous awards, including the China Young Female Scientists award in 2008, Distinguished Young Scientist award from National Natural Science Foundation of China in 2012, and several IEEE Best Student Paper awards from the 2017 IEEE Global Symposium on Millimeter-Waves, 2016 IEEE International Conference on Microwave and Millimeter-Wave Technology, 2016 IEEE MTT-S International Microwave Workshop Series on Advanced Materials and Processes, and 2015 IEEE Asia-Pacific Microwave Conference. She is currently the editor-in-chief of *Microwave and Optical Technology Letters*.

AdCom Member Perspectives

I am highly motivated to continue my service in the MTT-S AdCom and to help our Society in its further advancement over the coming years. First, I hope to promote the vision and value of the MTT-S within/outside the microwave community and attract more active members. This requires dynamic Chapter-level activities sponsored through the MTT-S AdCom's Education and Membership and Geographic Activities (MGA) committees, both of which can provide incentives



Figure 1. Rashaunda M. Henderson.



Figure 2. Wenquan (Cherry) Che.



Figure 3. Goutam Chattopadhyay.

and benefits through high-quality programs and events.

Second, I hope to expand the technical boundary of the MTT-S and explore cross-discipline fields. This can be achieved through new conferences and journals sponsored jointly with other sister/partner Societies, reshaping our Society for its sustainable development.

Third, I hope to inspire women and young professionals in the MTT-S through their augmented visibility in the microwave community. For such purposes, professional and social events organized through the Education Committee and the Women in Microwaves Subcommittee under the MGA Committee can provide helpful opportunities and platforms.

Goutam Chattopadhyay

Goutam Chattopadhyay (Figure 3) is a senior research scientist at the NASA Jet Propulsion Laboratory, California Institute of Technology (Caltech), and a visiting professor at Caltech, Pasadena. He received the Ph.D. degree in electrical engineering from Caltech in 2000. He is a Fellow of IEEE and of the Institution of Electronics and Telecommunication Engineers (India) as well as an MTT-S Distinguished Microwave Lecturer (DML). His research interests include microwave, millimeter-wave, and terahertz systems and radars for space applications. He has more than



Figure 4. Nuno Borges Carvalho.

350 publications in international journals and conferences and holds more than 20 patents. He is also the recipient of more than 35 NASA Technical Achievement and New Technology Invention awards. He received the IEEE Region 6 Engineer of the Year award in 2018, the IEEE Transactions on Terahertz Science and Technology Best Journal Paper award in 2020 and 2013, and the Best Paper award for antenna design and applications at the 2017 European Conference on Antennas and Propagation.

AdCom Member Perspectives

As a DML, I traveled the globe interacting with students, young professionals, researchers, industry experts, and others and observed firsthand their enthusiasm about microwaves, millimeter-waves, and terahertz. At the same time, there is a lack of growth in MTT-S membership. It is crucial that we find new ways to attract students and young professionals to our Society. We need to strengthen our DML program so that many DMLs can travel the world,

especially Region 10 (Asia-Pacific) as well as Africa and the Middle East, where membership growth potential is huge. There is tremendous hunger

among the students in these areas to learn about microwaves, but they lack resources to attend conferences outside their Region.

As an MTT-S AdCom member, my focus will be on Women in Microwaves and Young Professionals events. It is imperative that we address gender inequality and diversity. Our success depends on catching the imagination of the next generation of engineers, of all

colors, creeds, and genders, and filling it with a future in microwaves.

Nuno Borges Carvalho

Nuno Borges Carvalho (Figure 4) is currently a full professor and a senior research scientist with the Institute of Telecommunications, University of Aveiro, Portugal, and a Fellow of IEEE. He has coauthored several books

(continued on page 74)

Our success depends on catching the imagination of the next generation of engineers, of all colors, creeds, and genders, and filling it with a future in microwaves.

Cable Assemblies

1,000,000 RF Cables @OnlineCables.com



Applied Interconnect
TM

Phone: (408)749-9900
Fax: (408)734-9770
Sales@OnlineCables.com



MicroBusiness

Travel, Revisited

■ Fred Schindler

When I was a child, every few years my family would fly from the United States to Europe to visit relatives. In that era, flying was not commonplace; it was an occasion. Men would wear suits and ties; women would wear a nice dress and stockings. Leg room was spacious, and seats reclined more than a few centimeters. Food and drink were plentiful, and service was attentive. This was in coach class. We flew on Boeing 707s and Douglas DC-8s, which carried about 150 passengers. It was expensive. We traveled to Europe only every few years because of the cost. My parents needed to save up money to afford to pay for all of us.

By the time I was in college, air travel had started to change. Low-cost carriers had come into



©SHUTTERSTOCK.COM/CLAUDIA BALASOIU

being. When I finished my undergraduate studies, I traveled to the United Kingdom with my girlfriend (now wife) on Laker Airlines. Laker flew wide-body McDonnell–Douglas DC-10s that carried about 300 passengers.

We wore comfortable clothes, and the atmosphere was decidedly informal. Our airfare was US\$150 one way, which was much more affordable than full-fare carriers.

As I embarked on my career as an engineer and as my wife and I started a family, air travel became routine. Our family would fly to vacation destinations and to visit relatives, sometimes more than one trip a year. My wife and I often flew for business trips. Air travel was no longer a special occasion. In recent years, air travel has become a tedium.

As 2020 began, I anticipated numerous trips around the United States and beyond—more than a dozen. Then, in March, it all came to an end. I returned from my fourth trip of the year on February 28, and I haven't been to an airport since.

It's been the same for many of us. According to airport checkpoint data from the U.S. Transportation Security Agency, in September 2020, the agency handled fewer than one third the passengers it did in September 2019.

Fred Schindler (m.schindler@ieee.org)
consults on management issues in Boston,
Massachusetts, USA.

Digital Object Identifier 10.1109/MMM.2020.3035972
Date of current version: 11 January 2021

The pandemic has caused us to change how we live and work. Just as we have learned that many of us can work effectively from home, we've also found success interacting virtually with people in distant locales. Almost all conferences have been virtual since March 2020. Business meetings have largely been transacted via teleconferencing. We've connected with distant relatives and friends via video chat. Is travel dead?

As I'm writing this, my daughter, who lives on the west coast of the United States, is planning to visit us for the holidays in December. We won't have been together for a full year. Travel will pose a risk of exposure to the coronavirus for my daughter, but my wife and I are looking forward to her visit despite the risks. So are my other children. I suspect many other people will travel over the holidays, despite the pandemic.

My experiences with travel, and my family's, are similar to what many have experienced, both recently and over the past several decades. U.S. Department of Transportation statistics corroborate the long-term trend. Air travel continuously increased between 1960 and 2000. From 2000 to 2015, air travel continued to grow, although there were a few years of temporary decline after the 11 September 2001 terrorist attacks and during the Great Recession in 2008–2009.

These general air travel statistics don't provide any insights into how the trends for business and leisure travel differ. I suspect that the growth in business travel has slowed, or may even have started to decline, over the 10 years prior to the COVID-19 pandemic. There has been ever-growing adoption of telepresence throughout the 21st century. I recall, even in 1995, using a PictureTel system. That system was hampered by the limited bandwidth of the telephone networks of that time and was a poor surrogate for physical interaction.

Over the past 10 years, telepresence systems have become much more capable and have been able to take

advantage of ever more bandwidth to provide a more satisfactory meeting experience. The cost has come down significantly, and today we find that we can have an adequate meeting experience with most any smartphone or laptop computer. An example is the pervasive Zoom meetings we have had throughout the pandemic.

Prior to the pandemic, businesses were relying ever more on virtual meetings as an alternative air travel. Businesses want to avoid both the cost of travel and the inevitable employee downtime while traveling. Regardless, business air travel hasn't disappeared. Telepresence, no matter how good, isn't a suitable replacement for all meetings.

Leisure and personal travel are different. Here, a virtual experience is a poor substitute. A 40-min Zoom call with relatives cannot replace a multi-day visit. A virtual tour of a cultural site is far from the experience of physically visiting. I'm sure that, prior to the pandemic, leisure travel growth continued to be strong, regardless of the trends in business travel.

What does the future hold, from our vantage point several months into the pandemic? Leisure travel came to an almost complete halt at the onset of the pandemic. But some, like my daughter, are making personal trips, and more will certainly do so. She is traveling to see family, which is different from purely leisure travel. Anecdotally, I also know that some people are again starting to travel purely for leisure.

Business travel, in the pandemic, has been different from leisure travel. While it dropped dramatically at the onset of the pandemic, it continued throughout and has gradually been growing. I have an acquaintance in Boston who works in sales. Part of his territory is in Chicago, and he occasionally needs to travel and visit potential and existing customers. That type of business interaction is all but impossible to replicate virtually, so this is essential travel.

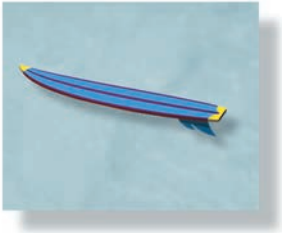
Routine, nonessential business travel, of the type that most engineers and engineering managers do, can, in many cases, be replaced by telepresence. It was under pressure before the pandemic and all but came to a halt at the pandemic's onset. Meanwhile, for many of us, work from home has continued virtually. We have become accustomed to virtual meeting tools and found that most routine interactions can be satisfied with them.

I'm sure nonessential business travel will recover, too, but almost certainly not to its prepandemic levels. Nonetheless, we are social beings, even if sometimes awkwardly so. We still have a need to meet face to face, so we will travel again. I hope to see you soon at an upcoming MTT-S sponsored conference.



We want to hear from you!

Do you like what you're reading?
Your feedback is important.
Let us know—
send the editor-in-chief an e-mail!



Microwave Surfing

A Moonshot?

■ Rajeev Bansal

Quiz: Take a look at the image in Figure 1 and guess what it represents.

- a) a Venn diagram representing political polarization in a neighborhood
- b) hexagonal close packing in a germanium crystal
- c) a cellular radio concept
- d) none of the above.

If you guessed c), you can give yourself a pat on the back. Figure 1 appeared in a 1947 Bell Labs internal technical memorandum [1] by D.H. Ring. While 1947 is now remembered as the year when the transistor was invented (also at Bell Labs), the eight-page document filed by Ring laid the foundation for what has become the dominant communication technology in the 21st century. In the context of car phones, Ring made the following modest proposal [1]:

In this memorandum it is postulated that an adequate mobile radio system should provide service to any equipped vehicle at any point in the whole coun-

Rajeev Bansal (rajeev.bansal@uconn.edu) is with the University of Connecticut, Storrs, Connecticut, USA.

Digital Object Identifier 10.1109/MMM.2020.3038129
Date of current version: 11 January 2021

Editor's Note: An earlier version of this column originally appeared in the February 2021 issue of *IEEE Antennas and Propagation Magazine*.

try. Some of the features resulting from this conception of the problem are discussed along with reference to a rather obvious plan for providing such service. The plan which is outlined briefly is not proposed as the best solution resulting from ex-

haustive study, but rather is presented as a point of departure for discussion and comparison of alternative suggestions which may be made.

While Ring was the first person to document the concept of cellular mobile communication, he acknowledged that the idea originated with another Bell Labs scientist, W.R. Young, who had "pointed out . . . the best general arrangement for the minimum interference and with a minimum number of frequencies is a hexagonal layout in which each

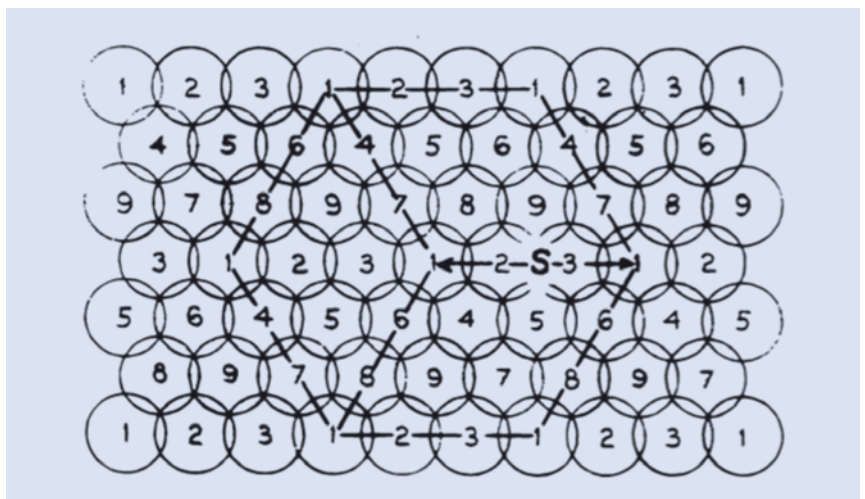


Figure 1. What does this represent?

station is surrounded by six equidistant stations [1].”

So what is Bell Labs up to now? Owned currently by the Finnish company Nokia, it recently received a US\$14.1 million contract from NASA to design and develop a 4G network on the moon [2]. According to Bell Labs, “Astronauts will use its wireless network for data transmission, controlling of lunar rovers, real-time navigation over lunar geography (think Google Maps for the moon), and streaming of high-definition video” [2]. It is all a part of the long-term NASA plan [3], “which entails 37 launches of private and NASA rockets, as well as a mix of robotic and human landers . . . with a ‘Lunar Surface Asset Deployment’ in 2028, likely the beginning of a

surface outpost for long-duration crew stays.”

At least in principle, the proposed 4G network should “work better on the moon than it does here—it won’t have any trees, buildings or TV signals to interfere with the 4G signal” [2]. On the other hand, it will have to be “specially designed to withstand the particularities of the lunar surface: extreme temperature, radiation and space’s vacuum. It will also stay functional during lunar landings and launches, even though rockets significantly vibrate the moon’s surface” [2]. Like the 5G networks being developed currently on Earth, the lunar mobile network will make use of the so-called small cells [2], [4]. I can’t wait to see images of an astronaut traipsing around on the moon asking, “Can you hear me now?”

References

- [1] A. Madrigal. “The 1947 paper that first described a cell-phone network.” *The Atlantic*. Accessed: Nov. 3, 2020. [Online]. Available: <https://www.theatlantic.com/technology/archive/2011/09/the-1947-paper-that-first-described-a-cell-phone-network/245222/>
- [2] D. Goldman. “NASA and Nokia are putting a 4G network on the moon.” *CNN*. Accessed: Nov. 3, 2020. [Online]. Available: <https://www.cnn.com/2020/10/18/tech/4g-network-moon-trnd/index.html>
- [3] E. Berger. “NASA’s full Artemis plan revealed: 37 launches and a lunar outpost.” *Ars Technica*. Accessed: Nov. 3, 2020. [Online]. Available: <https://arstechnica.com/science/2019/05/nasas-full-artemis-plan-revealed-37-launches-and-a-lunar-outpost/>
- [4] A. Nordrum et al. “Everything you need to know about 5G.” *IEEE Spectrum*. Accessed: Sept. 5, 2020. [Online]. Available: <https://spectrum.ieee.org/video/telecom/wireless/everything-you-need-to-know-about-5g>



From the Editor’s Desk *(continued from page 6)*

for these nonidealities, negative group delay circuits are often employed. This article covers a number of circuit topologies for group delay compensation, along with numerous references, allowing you to delve deeper into the operation of these circuits.

In the second article, “Waveguide Components Based on Multiple-Mode Resonators,” Wong et al. look at the use of multimode resonators in waveguides as a method to improve the frequency selectivity of the resonator while reducing the overall footprint. The article provides a tutorial on multimode waveguide resonators and shows numerous examples of these structures in applications such as diplexers, filters, and baluns.

The third feature, “Tunable Balanced Power Dividers” by Lin et al., provides an overview of balanced power dividers. Balanced power dividers (and their combining counterparts) are particularly useful because the balanced nature of their circuit operation provides some immunity to common

mode issues as well as noise. A number of circuits are shown with explanations of their operation; an extensive reference list is also provided for those wishing to learn more.

We also have an “Application Notes” column in this issue by Zubair Ahmed, “Revisiting the Binomial Multisection Transformer.” This impedance matching structure is commonly studied in various microwave engineering textbooks, but the author takes a different approach in explaining its operation. If any of your students have difficulty understanding common textbook approaches, this alternative explanation may be useful.

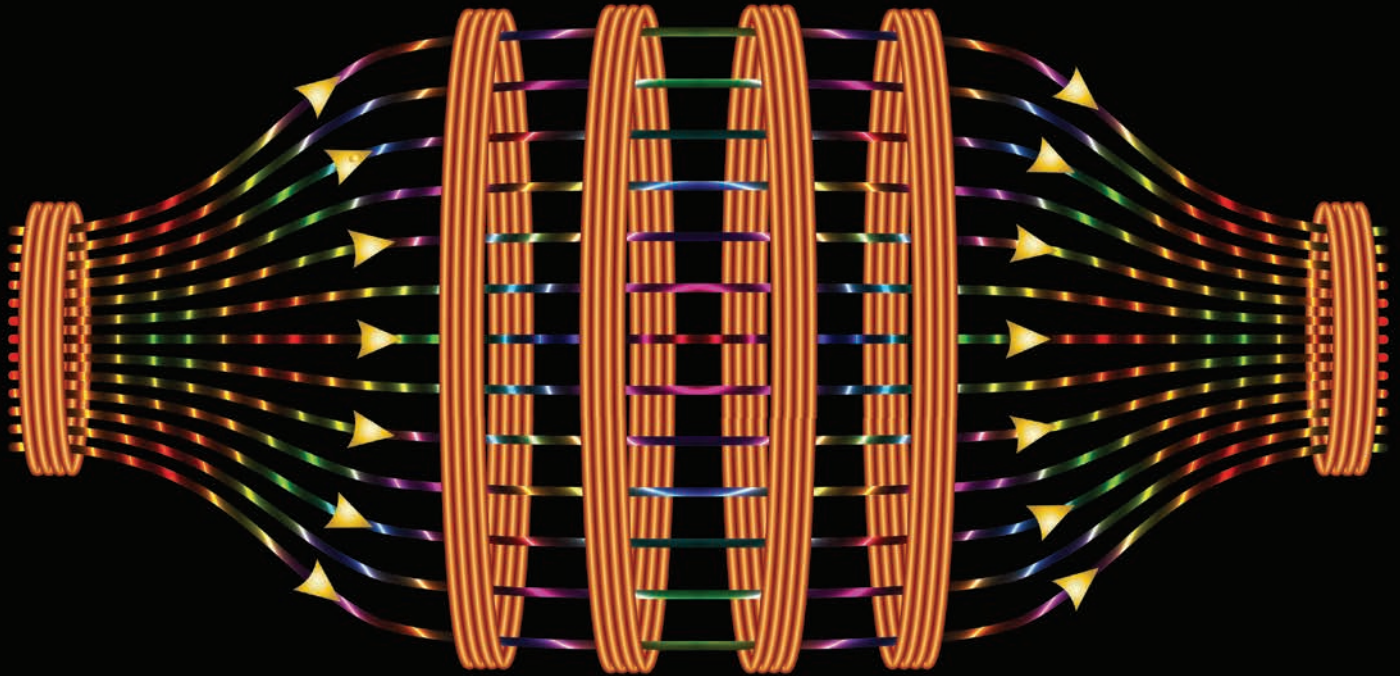
Also in this issue is the MTT-S president’s column, where Dr. Gregory Lyons introduces you to the new MTT-S president-elect for 2021 as well as returning Administrative Committee (AdCom) members for new three-year terms. As you have read about in the previous Society news “Spotlight” columns on the various AdCom committees, the MTT-S

AdCom is a group of volunteers engaged in promoting the direction and growth of the Society.

One area that the AdCom is involved with is the organization, promotion, and presentation of our MTT-S webinar series, and this month we have a short column on the planned webinars through the middle of the year. We also have a review of the recently published book *Millimeter-Wave Circuits for 5G and Radar* that you may wish to read or add to your library. Our “MicroBusiness” column speaks to all members about the pandemic restrictions on travel and how they affect the way we work as well as our lives. In addition, we have a “Microwave Surfing” column focusing on the origins of the concept of cellular mobile communication. Finally, Dr. Takashi Ohira continues his “Enigmas, etc.” series with another waveform engineering problem for you to solve. The solution to last month’s enigma is also included. I hope you enjoy the issue.



Negative Group Delay Circuits and Applications



©SHUTTERSTOCK.COM/FOUAD A. SAAD

*Jian-Kang Xiao, Qiu-Fen Wang,
and Jian-Guo Ma*

With the rapid development of new-generation communication technology such as multiple-input/multiple-output technology, ultrawideband communication, and 5G technology, communication systems have higher requirements for the quality of signal transmissions.

Achieving this quality requires attention not only to signal amplitude characteristics but also to phase characteristics because of the long delays and signal distortion that come with positive group delay (PGD). However, negative group delay (NGD) circuits are an effective way to compensate for PGD and decrease the variability of passband group delay.

Jian-Kang Xiao (jkxiao@xidian.edu.cn) and Qiu-Fen Wang (cherish_old_time@163.com) are with the School of Electro-Mechanical Engineering, Xidian University, Xi'an, China. Jian-Guo Ma (mjg@gdut.edu.cn) is with the School of Computers, Guangdong University of Technology, Guangzhou, China.

Digital Object Identifier 10.1109/MMM.2020.3035862

Date of current version: 11 January 2021

In the past few years, NGD circuits [1]–[23], both passive and active, have been designed using resistance-inductance-capacitance (RLC) circuit resonators [1], utilizing the signal attenuation characteristics of a bandstop filter (BSF) [2]–[6] and absorptive [4] and matched techniques [7]–[10] to enhance the attenuation of S_{11} for reducing the reflection to the source, which is helpful to overcome the undesired standing waves and instability problems of microwave system terminals. Other methods, including signal-interference techniques [13], effective negative dielectric permittivity techniques [15], use of a composite right-/left-handed transmission line [19], and microwave transversal filter approaches [23], have also been used to implement NGD circuits. Tunable NGD circuits [16] and suspended multilayer NGD circuits [17] have also been developed. A time-domain experiment of an NGD circuit [24] has also been done. A major disadvantage of NGD circuits is their large signal attenuation (S_{21}), which requires more power compensation.

The design of NGD circuits focuses on NGD time and bandwidth, signal attenuation, and matching, which all differ from BSFs. However, NGD circuit designs can be based on BSFs because of their similar signal attenuation characteristics. Of course, other methods are also effective for NGD circuit design.

Because of their very useful PGD compensation and passband group delay flatness, NGD circuits have been applied to various microwave circuits in communication systems for uses such as improving the efficiency of feedforward amplifiers [25], minimizing beam-squint delay flatness in phased-array antennas [26], eliminating phase variation with frequency in broadband-constant phase shifters [27], realizing non-Foster reactive elements [28], [29], producing NGD characteristics in power dividers (PDs) [30]–[32] and couplers [33], [34] to minimize the effect of the PGD of traditional circuits, and incorporating time-delay cancellation in sensors [35].

The NGD Phenomenon

Group delay was proposed by Nyquist and Brand [36] to describe phase linearity. It refers to the delay of the whole signal when a group of signals pass through a transmission system and can be defined as

$$\tau_g(\omega) = -\frac{d\phi(\omega)}{d\omega} \quad (1)$$

with $\phi(\omega) = \angle S_{21}(j\omega)$, where $\phi(\omega)$ is the phase, S_{21} is the transmission coefficient of a two-port network, and ω is the angular frequency. It yields

$$\tau_g(\omega) = -\frac{d\angle S_{21}}{d\omega} = -\frac{d}{d\omega} \left[\arctan \frac{\text{Im}(S_{21})}{\text{Re}(S_{21})} \right]. \quad (2)$$

It can be seen that the group delay drives the slope of the phase-frequency characteristic curve: a negative slope leads to a PGD, while a positive slope leads

to an NGD, as shown in Figure 1(a); the corresponding lumped-element circuit is displayed in Figure 1(b). NGD occurs in the frequency range where the signal is absorbed or attenuated to the maximum; therefore, a traditional NGD circuit is based on the bandstop structure of series/parallel RL resonators. Figure 1(b) is a typical Π -shaped lumped-element NGD circuit, where both the input and output terminal reference impedances are Z_0 .

It should be noted that group delay is the delay time of the signal envelope, not the phase delay of a single frequency, because there is no group delay for a single frequency. Thus, a group delay is also called an *envelope delay*. The transmission waveform distortion can be minimized when the group delay is constant.

NGD is commonly accompanied by a superluminal phenomenon. Superluminal speed, here, is not the speed of energy or information transmission but the group speed of the signal, so this kind of speed, which is greater than the speed of light in free space, does not contradict Einstein's theory of relativity, which states that no speed can exceed the speed of light.

Assume that a modulated Gaussian pulse (an input pulse) enters an arbitrary resonant circuit, such as a two-port network. If the circuit is lossless and the bandwidth of the input pulse is relatively narrow, the output waveform will lag behind the input waveform,

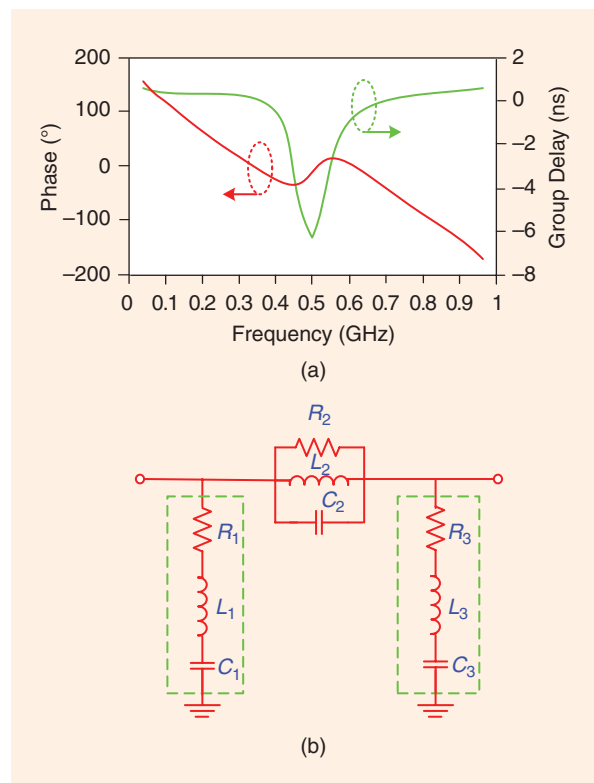


Figure 1. NGD and a typical lumped-element circuit. (a) The schematic curves of NGD and its phase [37]. (b) A typical Π -shaped lumped-element NGD circuit [37].

which causes the output port to have a PGD, that is $\tau_{\text{out}} - \tau_{\text{in}} > 0$; meanwhile, the waveform remains basically unchanged, as illustrated in Figure 2.

Let the propagation length of the input pulse in free space (lossless) be l ; the propagation time for the pulse reaching the peak would be $\tau_{\text{in-max}} = l/c$. But, when the resonant circuit has loss and the propagation length of the pulse is still l , then the propagation time for the output envelope reaching its peak value would be $\tau_{\text{out-max}} = l/v_g$, where c is the velocity of light in free space and v_g is the phase velocity of the output envelope. If $v_g > c$ (superluminal), we have $\tau_{\text{in-max}} > \tau_{\text{out-max}}$, as shown in Figure 2, which would lead to the NGD [38]

$$\tau = \tau_{\text{out-max}} - \tau_{\text{in-max}} < 0. \quad (3)$$

Of course, in theoretical analysis, for an NGD time of $\tau < 0$, v_g can also be negative (negative group velocity), and in this case, the contribution of the lumped part dominates that of the free propagation path [39].

The NGD effect can be regarded as the electromagnetic (EM) wave passing through the dispersion

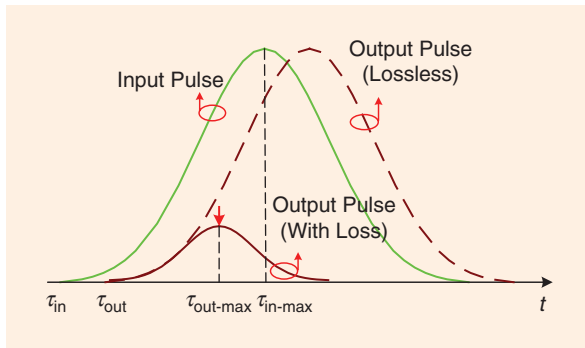


Figure 2. The NGD phenomenon [38].

medium or circuit and its output signal amplitude envelope reaching the medium or circuit in time-advance without delay, as depicted in Figure 2. It also indicates that lossless networks always have a PGD, while loss introduces the NGD. In other words, for passive reciprocal networks, loss is a necessary condition for the generation of NGD.

General Conditions of NGD Transmission

NGD originates from a BSF, and a resonator-feeding line coupling is one of the more effective methods for BSF design, one that is also commonly used for NGD circuit design. The general condition of NGD can be obtained by using a resonator-feeding, line-coupling structure from the energy storage [40].

A typical coupling open-loop resonator is shown in Figure 3(a), where the coupling between the open-loop resonator and the input port is by the semicircular coupled structure. An equivalent circuit of the single-port coupling structure is displayed in Figure 3(b), where the parallel RLC circuit represents the open-loop resonator with a self-resistance of R , a self-inductance of L , and a self-capacitance of C , and the parallel $L_c C_c$ circuit, which denotes the mixed electric/magnetic coupling, represents the coupling between the open-loop resonator and the input port; here, L_c and C_c denote the magnetic and electric couplings, respectively. To simplify the calculation, an admittance inversion converter is used to replace the parallel $L_c C_c$ circuit, as presented in Figure 3(c).

According to microwave network theory, the reflection phase of the equivalent circuit can be obtained from the reflection coefficient and formulated as [40]

$$\phi_r = \tan^{-1} \frac{\omega C Y_0 - Y_0 / \omega L}{Y_0 / R - j^2} - \tan^{-1} \frac{\omega C Y_0 - Y_0 \omega L}{Y_0 / R + j^2}, \quad (4)$$

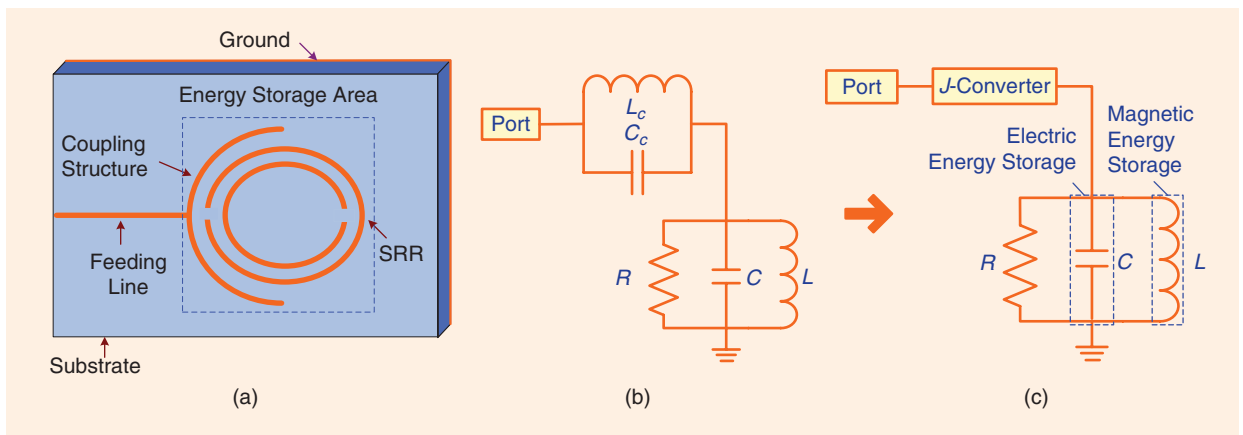


Figure 3. A resonator-feeding, line-coupling structure and its equivalent circuit model [40]. (a) A coupling structure, (b) the equivalent circuit, and (c) the admittance inversion converter replacing the $L_c C_c$ circuit. SRR: split-ring resonator.

where Y_0 is the admittance of the source. The group delay at the resonant frequency $\omega_0 = 1/\sqrt{LC}$ can be expressed as

$$\tau_d(\omega_0) = -\frac{d\phi_r}{d\omega} \Big|_{\omega=\omega_0} = \frac{4J^2 \frac{1}{Y_0}}{\frac{\omega_0 J^4}{Y_0^2} \sqrt{\frac{L}{C}} - \frac{\omega_0}{R^2} \sqrt{\frac{L}{C}}} \quad (5)$$

It is noted that the denominator of (5) can be divided into two parts: 1) $\omega_0 J^4 \sqrt{L/C}/Y_0^2$, which is related to the energy coupling between the resonator and the input port, and 2) $\omega_0 \sqrt{L/C}/R^2$, which is linked to the energy consumption of the resonator itself. Thus, it can be concluded that the group delay is determined by the energy storage capacity of the coupling structure, as shown in Figure 3.

The group delay of the coupling structure can be shown as [40]

$$\tau_d(\omega_0) = \frac{4Q_e}{\omega_0 \left(1 - \left(\frac{Q_e}{Q_0}\right)^2\right)} \quad (6)$$

with inner quality factor $Q_0 = R\sqrt{C/L}$ and external quality factor $Q_e = (Y_0 \sqrt{C/L})/J^2$ [40]. It is clear from (6) that the sign of the group delay is determined by the ratio of Q_e to Q_0 . When $Q_e < Q_0$, it is a PGD, but when $Q_e > Q_0$, an NGD can be obtained. Thus, NGD can be obtained in two ways. One is by increasing the resonator loss—which amounts to decreasing Q_0 —but, because we know that the inner quality factor is always fixed when the resonator structure is certain, a resistor must be introduced to obtain the reduced Q_0 . The other approach is to increase Q_e by reducing the coupling between the resonator and the source, which can be easily realized by enlarging the coupling distance between the resonator and the semicircular coupled structure.

It is important to note the relationship between group delay and the amplitude of S_{21} (insertion loss). Greater attenuation of S_{21} will introduce greater NGD time.

Design Methods of Microwave NGD Circuits

Design of BSF Multiband NGD Passive Circuits

NGD can be realized by utilizing the signal attenuation characteristics of a BSF, such as the resonator-feed, line-coupling; stub/resonator-loaded; and defected microstrip structure BSFs, which are depicted in Figure 4(a)–(c), respectively.

A triband defected microstrip structure NGD circuit [6] with three composite L-shaped deflections in a 50-Ω microstrip line is shown in Figure 5(a). The center frequencies of the first, second, and third bands can be controlled by the corresponding etched slot with lengths of l_1 , l_2 , and l_3 , respectively, while the desired NGD time of each band can be obtained independently and easily adjusted by the corresponding resistor connected across the slot. The triband NGD circuit

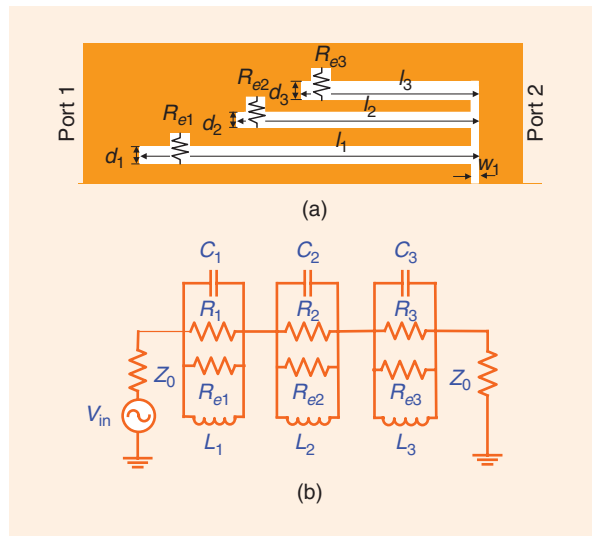


Figure 5. The triband NGD circuit and its equivalent circuit [6]. (a) A circuit physical structure and (b) the equivalent circuit.

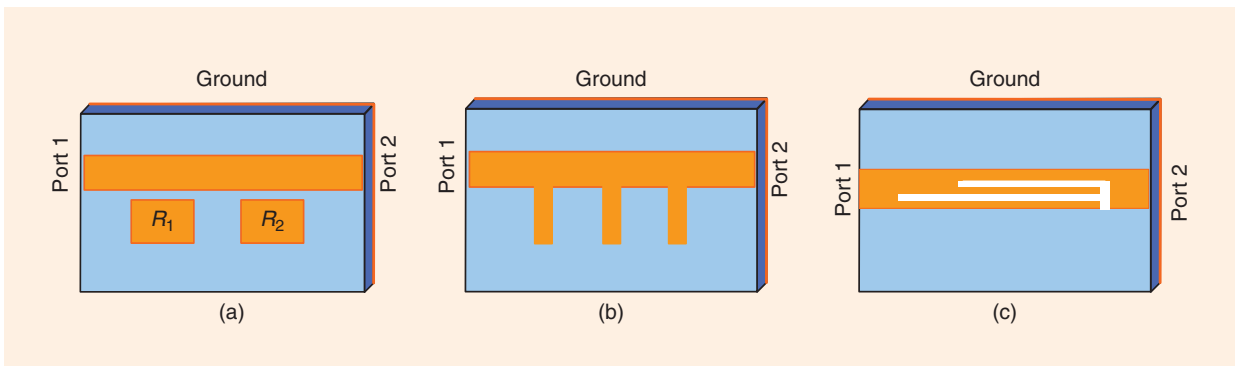


Figure 4. Microstrip BSF structures. (a) A resonator-feed, line-coupling BSF. (b) A stub/resonator-loaded BSF. (c) A defected microstrip structure BSF.

can be equivalent to a parallel RL circuit, as plotted in Figure 5(b), where R_i , L_i , and C_i are the self-resistance, inductance, and capacitance of the RL resonator unit, respectively, and $i = 1, 2$, and 3 . R_{ei} is the loaded resistance in each slot. The design concept can also be extended to a quad- or higher-band NGD circuit.

The parameters of the equivalent circuit can be extracted based on circuit theory and simulation optimization. The forward transmission scattering parameters S_{21i} ($i = 1, 2$, and 3) can be expressed as [2], [16]

$$S_{21i} = 1 - e^{j\theta_i} / \sqrt{(1 + 2/Y_0 R_{ii})^2 + 4/Y_0^2 (\omega C_i - 1/\omega L_i)}, \quad (7)$$

with $R_{ii} = R_i R_{ei} / (R_i + R_{ei})$, where Y_0 is the characteristic admittance of the input/output ports. The phase of S_{21i} , the group delay time, and the insertion loss can be obtained from (7) as

$$\theta_i = -\arctan 2/Y_0 (\omega C_i - 1/\omega L_i) / (1 + 2/Y_0 R_{ii}), \quad (8a)$$

$$\tau = -d \angle S_{21i} / d\omega = -2R_{ii}^2 C_i / (2Z_0 + R_{ii}), \quad (8b)$$

$$|S_{21i}| = 2Z_0 / (2Z_0 + R_{ii}), \quad (8c)$$

where Z_0 is the port impedance with a value of 50Ω , and $Y_0 = 1/Z_0$.

TABLE 1. The equivalent circuit parameters.

C_i (pF)	L_i (nH)	R_i (k Ω)	R_{ei} (k Ω)
3.7101	0.8706	1.6095	2.7
C_2 (pF)	L_2 (nH)	R_2 (k Ω)	R_{e2} (k Ω)
1.7475	0.7771	4.3865	2.7
C_3 (pF)	L_3 (nH)	R_3 (k Ω)	R_{e3} (k Ω)
1.2257	0.6147	2.6041	2.7

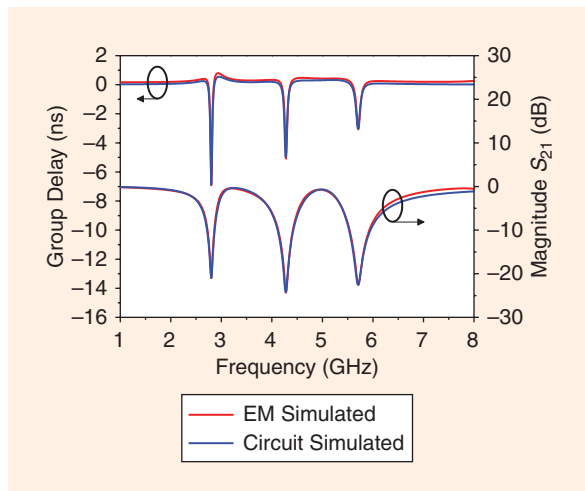


Figure 6. A comparison of circuit and EM simulations.

For the triband NGD circuit specifications of $f_{01} = 2.8$ GHz, $\tau_{01} = -6.5$ ns, $f_{02} = 4.3$ GHz, $\tau_{02} = -5.4$ ns, $f_{03} = 5.8$ GHz, and $\tau_{03} = -3$ ns, the equivalent circuit parameters can be calculated and extracted using the desired circuit specifications, (7) and (8a)–(8c), and the resonant frequency of $f_{0i} = 1/(2\pi\sqrt{L_i C_i})$, as listed in Table 1. The circuit model simulation result using the Advanced Design System (ADS) software is plotted in Figure 6, which agrees well with the EM simulation result.

The simulated EM field characteristics of the triband NGD circuit for three different frequencies are shown in Figure 7, which indicates that each band of the NGD circuit can be controlled separately. The hardware fabrication and the measurements are shown in Figure 8. The triband NGD circuit has a measured center frequency of 2.8/4.3/5.8 GHz, with an NGD time of $-6.5/-5.4/-3$ ns and an NGD bandwidth of 120/180/250 MHz, respectively. The measurement approaches the simulation. The circuit has a compact size of $0.387 \lambda_g \times 0.032 \lambda_g$ (30 mm \times 2.46 mm).

Another dual-band NGD circuit with a center frequency of 2.54/4.8 GHz and an NGD time of $-3.34/-2.72$ ns

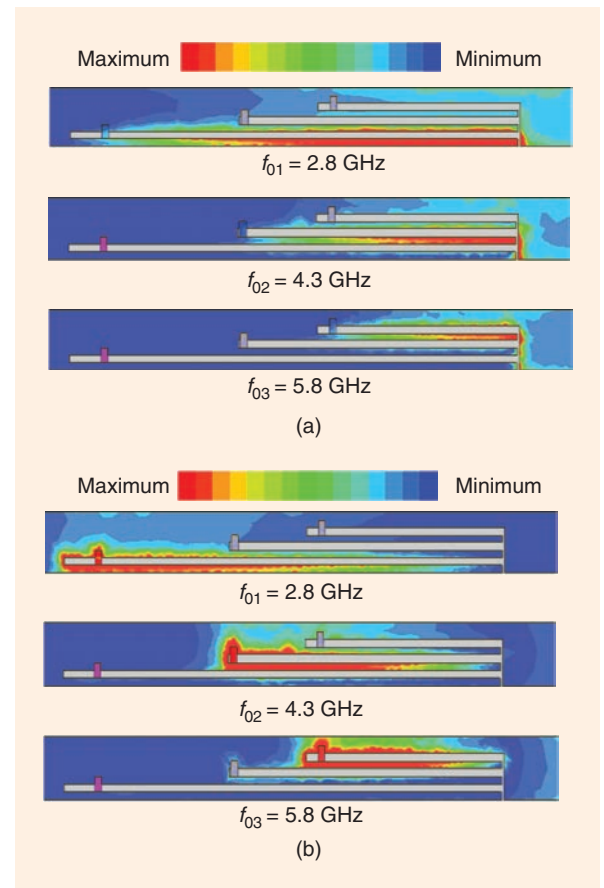


Figure 7. The simulated EM field distributions. (a) An electric field distribution and (b) a magnetic field distribution.

is illustrated in Figure 9(a), which is designed using the following process: first, etch a rectangular-shaped deflection on the 50- Ω microstrip transmission line; second, embed two stubs in the deflection to generate the desired dual band; finally, add a resistor across the embedded stub and the microstrip line to obtain the desired NGD time. The circuit can be viewed as a combination of an L-shaped, stub-embedded resonator, as presented in Figure 9(b), and a U-shaped,

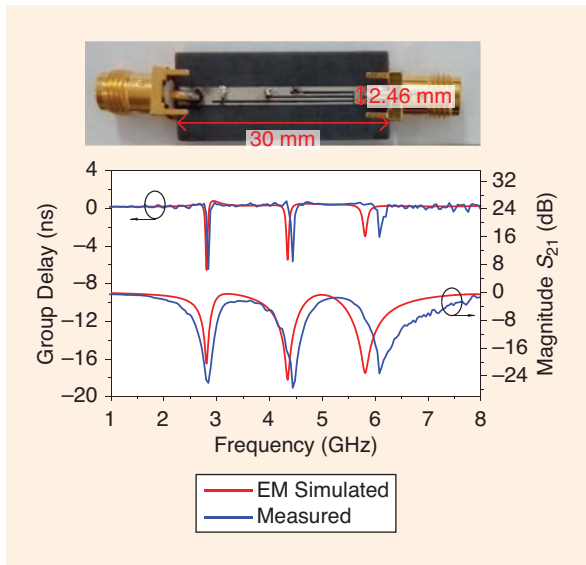


Figure 8. The fabrication and measured results of the triband NGD circuit [6].

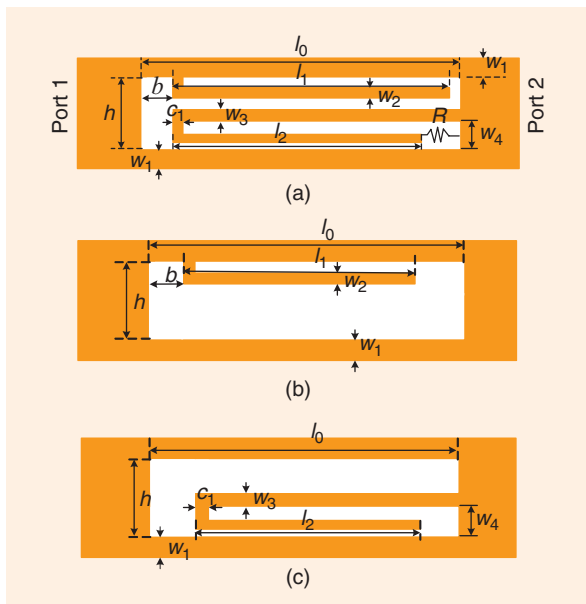


Figure 9. The dual-band NGD circuit structure and its composition. (a) The circuit structure. (b) Part 1 for working at f_{02} . (c) Part 2 for working at f_{01} . $l_0 = 12$, $l_1 = 11.2$, $l_2 = 10.7$, $h = 2$, $b = 0.6$, $w_1 = c_1 = 0.2$, $w_2 = 0.3$, $w_3 = 0.4$, and $w_4 = 0.7$. Unit: mm; $R = 10$ k Ω .

stub-embedded resonator, as shown in Figure 9(c), that control the second and first bands, respectively.

The simulated dual-band NGD circuit group delay and S_{21} variations with parameters l_1 and l_2 are displayed in Figure 10(a) and (b), respectively. Figure 10(a) shows that when l_1 is increased from 9.2 to 11.2 mm and the other dimensions are fixed, the center frequency of the second band lowers gradually, while the group delay, S_{21} magnitude, and the circuit's center frequency of the first band remain almost unchanged. Figure 10(b) indicates that the center frequency of the first band decreases when l_2 increases, so the circuit's center frequencies can be individually controlled. Group delay and S_{21} behave similarly.

The simulated dual-band NGD circuit group delay and S_{21} variations versus resistor R are shown in Figure 11, which indicates that circuit signal attenuation and group delay can be controlled by an external resistor.

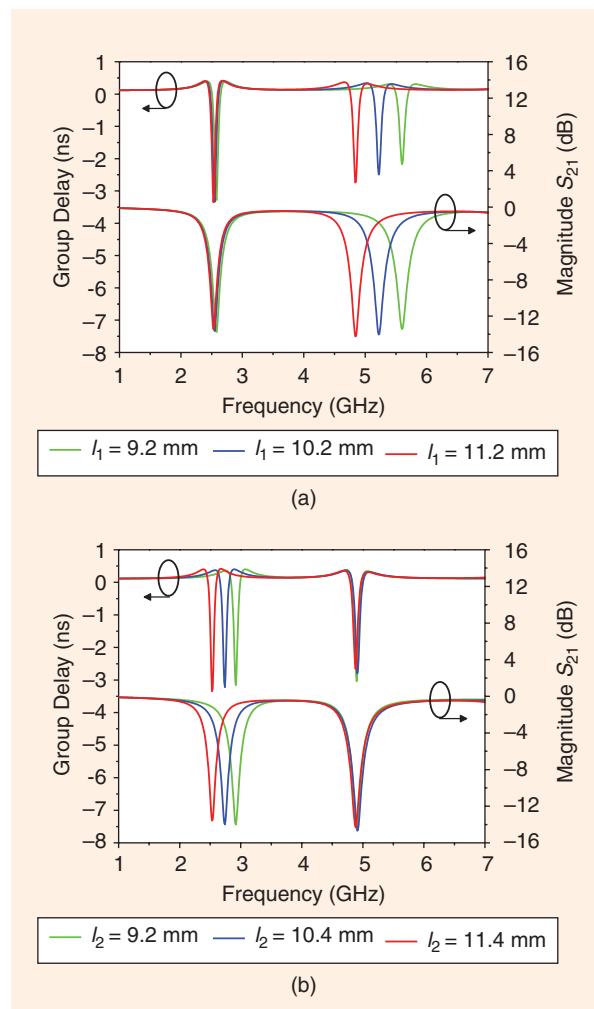


Figure 10. The simulated results of the group delay and the signal attenuation versus stub physical lengths l_1 and l_2 . (a) The variation curves versus l_1 . (b) The variation curves versus l_2 .

The dual-band NGD circuit was fabricated on an RT/Duroid 5880 substrate with a dielectric constant of 2.2 and a thickness of 31 mils; a photo and the measured results are presented in Figure 12(a) and (b), respectively. The measurements show that the NGD circuit centers at 2.6/4.9 GHz, with a signal attenuation of $-16.1/-17.3$ dB and an NGD time of $-3.9/-3.1$ ns, which approach the simulation. The dual-band NGD circuit has a circuit size of $0.276 \lambda_g \times 0.031 \lambda_g$.

Although the dual and triband NGD circuits have controllable working frequencies and NGD times, the

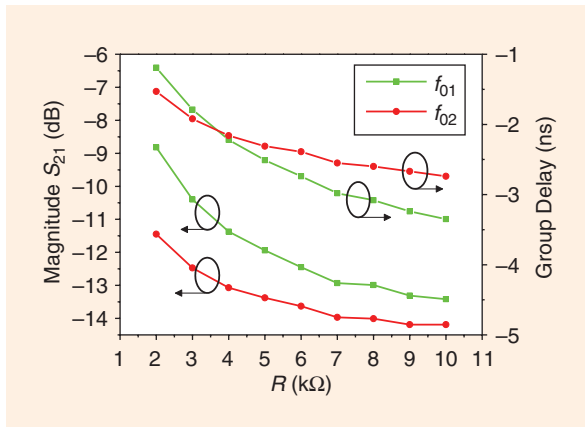


Figure 11. The group delay and signal attenuation variation curves versus R .

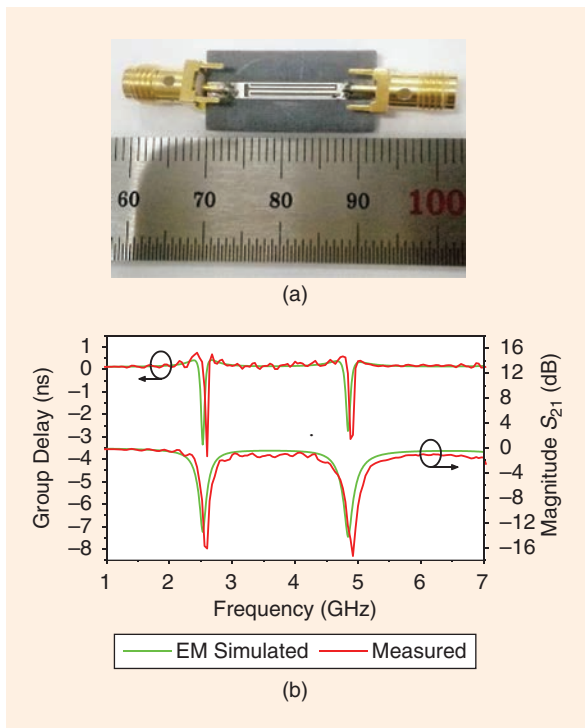


Figure 12. The fabrication and the measurements of the dual-band NGD circuit. (a) The fabricated hardware and (b) the measured results.

reflection wave to the source is inevitable because they are unmatched.

Design of Matched NGD Passive Circuits

According to microwave circuit theory, return loss (RL/S_{11}) can be expressed as [41]

$$RL = -20 \log |\Gamma| \text{ dB}, \quad (9)$$

where Γ is the voltage reflection coefficient of the terminal-loaded transmission line. When $|\Gamma|=1$ (total reflection), $RL=0$ dB, which would bring the whole reflection wave to the source and introduce undesired standing waves and instability problems in the microwave system terminal. When $\Gamma=0$, the return loss can be achieved as $RL=\infty$ dB, the circuit would be matched, and the reflection wave problems would be overcome. Of course, an infinite return loss is only an ideal case.

A Matched NGD Circuit Using Impedance Transformers

Impedance transformers in the input/output ports [12] have been used for matched NGD circuit designs. Although this kind of technology has a simpler circuit topology, as depicted in Figure 13, the use of impedance transformers would provide a PGD time, which would bring uncertainty for the desired NGD; moreover, the circuit size would also be greatly

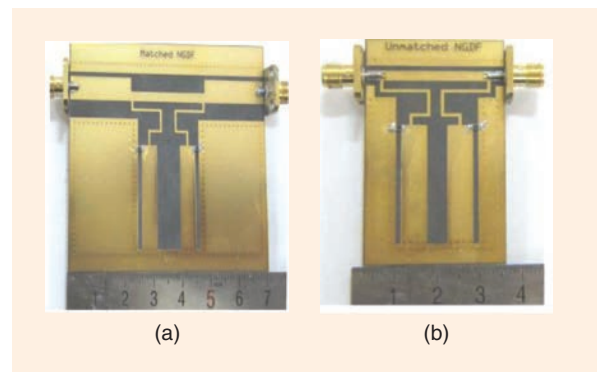


Figure 13. The NGD circuits (a) with and (b) without impedance transformers [12].

TABLE 2. A performance comparison of NGD circuits with and without impedance transformers.

Circuit/ Performance	NGD Time (ns)	S_{11} at CF (dB)	SA (dB)	NGD BW (MHz)
Matched NGD circuit	-6.5	-24	-21.2	90
Unmatched NGD circuit	-7.3	-5	-22.65	100

CF: center frequency; SA: signal attenuation (S_{21}); BW: bandwidth.

increased, as per the comparison in Figure 13(a) and (b). A measured performance comparison of NGD circuits with and without impedance transformers is listed in Table 2, where “matched” and “unmatched” represent the circuit with and without impedance transformers, respectively.

A Matched NGD Circuit Using Resistor-Connected Coupled Lines

Coupled lines [7]–[10] are effective for matched NGD circuit designs. The design scheme of the NGD circuit with resistor-connected coupled lines is an open-circuited, resonator-loaded structure that generates an NGD connected with a pair of shunt resistor-loaded coupled lines, which introduce matching [9]. The ideal circuit model is constructed by a pair of shunt resistor-connected coupled lines with even-/odd-mode characteristic impedances of Z_{1e} and Z_{1o} , an electrical length of θ_1 , and an open-circuited resonator structure with characteristic impedances of Z_2/Z_3 and corresponding

Although the dual and triband NGD circuits have controllable working frequencies and NGD times, the reflection wave to the source is inevitable because they are unmatched.

electrical lengths of θ_2/θ_3 , respectively. [see Figure 14(a)]. The realized circuit structure is shown in Figure 14(b), where R is the resistance of the shunt resistor and $\theta_i = (l_i \omega \sqrt{\epsilon_{re}})/c$, with $i = 1, 2$, and 3. Here, l_i is the physical length of the i th microstrip line, ω is the circuit angular frequency, ϵ_{re} is the effective permittivity, and c is the velocity of light in free space.

The NGD circuit is designed at 3.5 GHz with an NGD time of -3.7 ns, an NGD bandwidth of 110 MHz ($\tau = 0$), and a reflection coefficient attenuation of 32 dB.

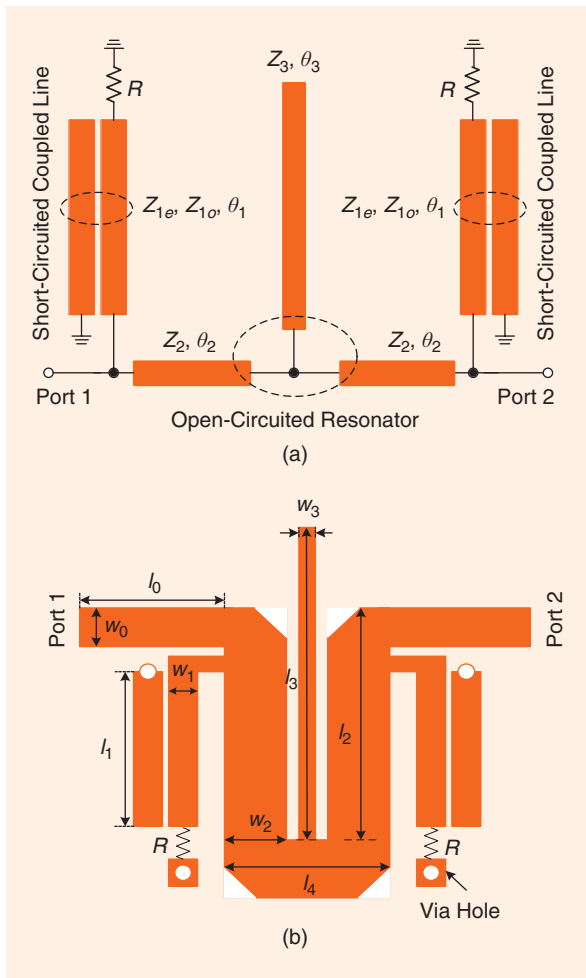


Figure 14. The matched NGD circuit with resistor-connected coupled lines [9]. (a) The circuit model and (b) the circuit structure.

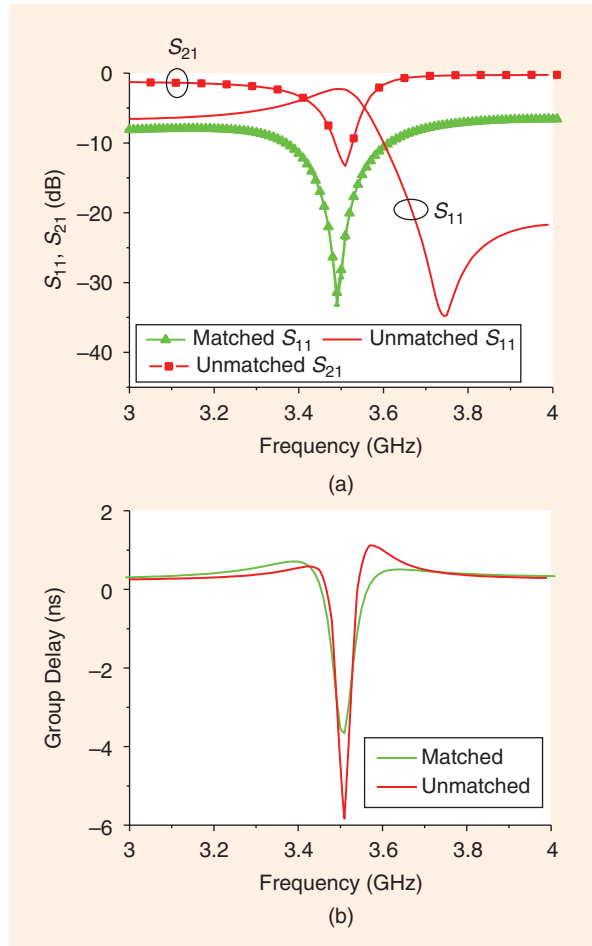


Figure 15. The simulated S_{11} and group delay with and without matching [9]. (a) A comparison of S_{11} with and without matching. (b) A comparison of group delay with and without matching.

The resistor-connected coupled lines are used to obtain matching, which makes S_{11} greatly attenuated at the desired frequency. Figure 15(a) and (b) shows the simulated S -parameter and group delay with and without resistor-connected coupled lines, respectively, which indicates that S_{11} has attenuated more than 30 dB at the center frequency when matched, while the group delay has a change of no more than 2.2 ns. Note that the production of NGD is not dependent on matching because NGD can still be produced even without matching, as illustrated in Figure 15(b). The resistor-connected coupled lines are very helpful for S_{11} attenuation but have a very slight influence on S_{21} , as demonstrated in Figure 16(a) and (b). The greatly attenuated reflection coefficient means that the reflection wave to the source can be greatly reduced, which is helpful in eliminating the undesired standing waves and instability problems of a microwave system terminal.

The fabrication and the measured results of the NGD circuit are shown in Figure 17(a) and (b). The NGD circuit has a measured S_{11} attenuation of more than 33 dB, an NGD bandwidth of no fewer than 120 MHz, and an NGD time of -4.6 ns. The NGD circuit has a compact size of $0.33 \lambda_g \times 0.29 \lambda_g$.

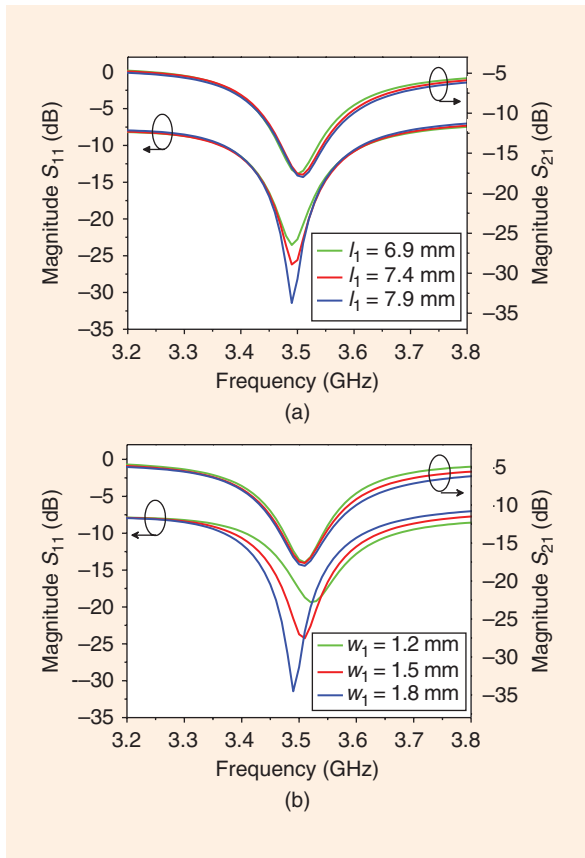


Figure 16. The S -parameter variations versus l_1 and w_1 [9]. (a) S_{11}/S_{21} variations versus l_1 . (b) S_{11}/S_{21} variations versus w_1 .

A Self-Matched NGD Circuit Using a Signal-Interference Technique

A self-matched NGD circuit using a signal-interference technique [13] is composed of two unequal Wilkinson PDs and a coupled-line phase shifter, as shown in Figure 18. One unequal PD is used to generate two path signals, the phase of which is shifted by the coupled line, while the other PD is used as a combiner to carry

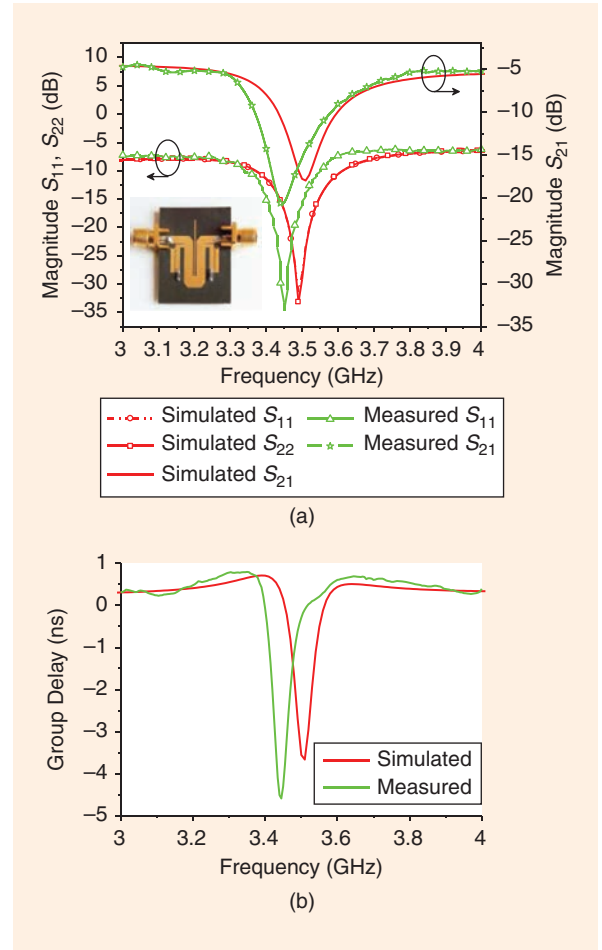


Figure 17. The experimental results [9]. (a) The measured and simulated S -parameters. (b) The measured and simulated group delay.

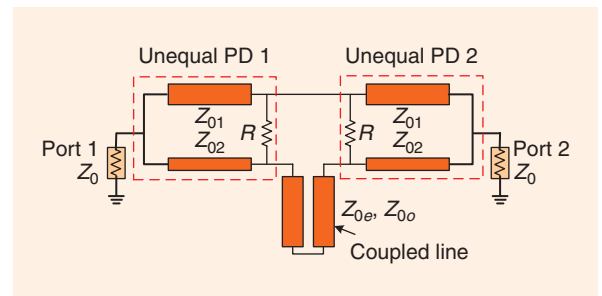


Figure 18. A circuit model of the NGD circuit with a signal-interference technique [13].

out destructive interference for obtaining NGD characteristics. The coupled line also helps in input/output matching. Photos of the fabricated hardware are shown in Figure 19(a) and (b), and the measured results are plotted in Figure 20(a) and (b), which demonstrate that the NGD circuit with a signal-interference technique has an NGD time of -2.09 ns, an insertion loss of fewer than 18.1 dB, and a return loss of greater than 33 dB at the center frequency of 1.02 GHz.

NGD Circuits Without Resistors

An NGD circuit based on a coupling matrix with a finite unloaded quality factor of resonators [22] has been designed and implemented, as shown in Figure 21. Unlike conventional NGD circuit topologies that use a lumped resistor R along with bandstop resonators, the

NGD circuit with finite unloaded quality-factor resonators has both source-to-load and interresonator coupling structures, as illustrated in Figure 21(a). No extra networks for matching input/output ports with reference termination impedances are required, while the predefined NGD and matched ports that bring greatly attenuated S_{11} are obtained. The equivalent transmission line model of the NGD circuit without resistors is shown in Figure 21(b), where Z_i ($i = 1, 2,$ and 3) is the characteristic impedance corresponding to the transmission line, with a width of w_i . θ_i and θ_j ($j = 4, 5$) are the electric lengths corresponding to the transmission line, with physical lengths of l_i and l_j , respectively [22]. The measured results of the NGD circuit are listed in Table 3.

An NGD circuit with an O=O geometrical shape is also designed and realized [42], as shown in Figure 22. The NGD circuit topology is composed of a PD, coupled line, and power combiner, as shown in Figure 22(a), and the fabricated hardware is displayed in Figure 22(b). The O=O-shaped NGD circuit has an NGD time of -2.8 ns, with a signal attenuation of only -2.2 dB and a reflection coefficient of better than -15 dB.

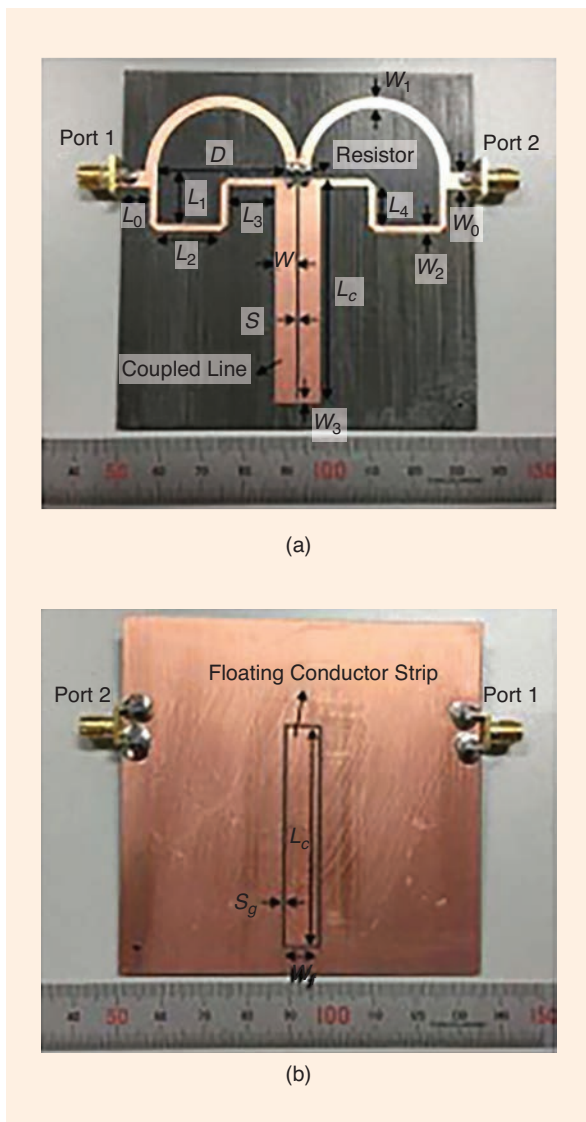


Figure 19. Photos of the fabricated NGD circuit [13]. (a) The top view and (b) the bottom view.

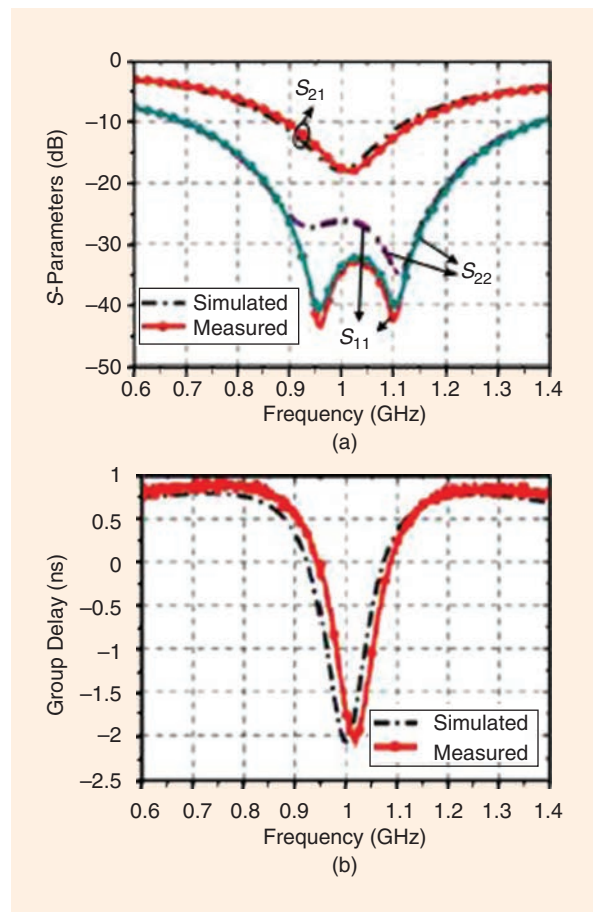


Figure 20. Comparisons of the measured results and simulations [13]. (a) The S-parameter comparison and (b) the group delay comparison.

NGD time can be adjusted via a loading resistor, which, when matched, can attenuate the standing wave, while the NGD time is proportional to the signal attenuation.

The electric performance and circuit sizes of some reported NGD circuits are listed in Table 3; all are measured results. It can be seen that NGD circuits with

single, dual, and tribands have all been realized, but matching is the limiting factor for multiband NGD circuits. The NGD circuit in [6] has the smallest circuit size because it is designed with a 50-Ω defected microstrip structure. The table also shows that the included NGD circuits have NGD times that range from -1.03 to -8.75 ns, with a minimum signal attenuation of 2.2 dB and a maximum return loss of 33 dB. It can be clearly seen that the NGD circuits focus on NGD time and bandwidth, signal attenuation, and return loss. NGD time can be adjusted via a loading resistor, which, when matched, can attenuate the standing wave, while the NGD time is proportional to the signal attenuation.

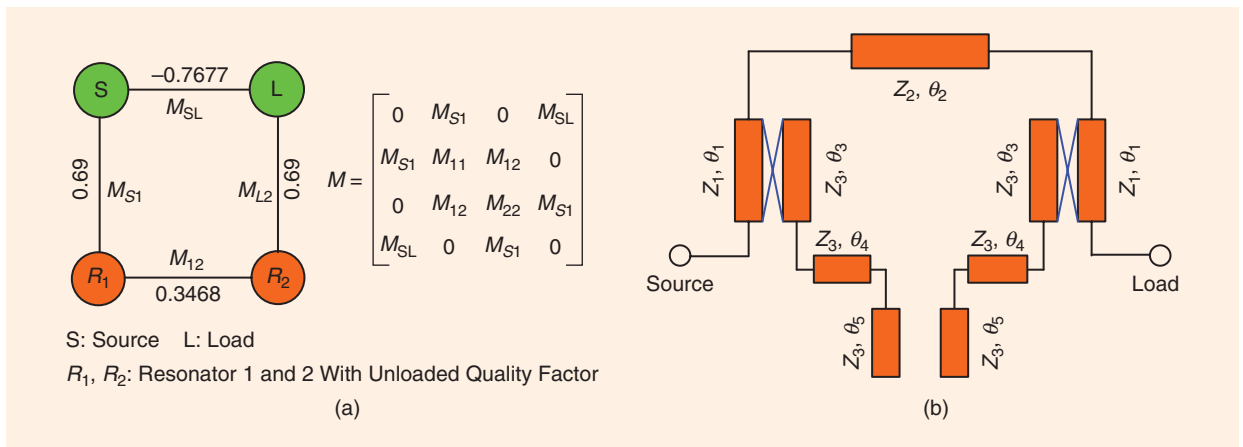


Figure 21. The NGD circuit based on coupling matrix. (a) A coupling topology and (b) the transmission line circuit model.

TABLE 3. A comparison of published NGD circuits.

Reference	CF (GHz)	NGD (ns)	NGD-BW (MHz)	SA (dB)	S_{11} (dB)	Matched or Not	Size $\lambda_g \times \lambda_g/\text{mm}^2$
[2] Dual band	3.50/5.15	-4.54/-4.20	330/270	-47.3/-38.8	-	Not	-
[3]	2.14	-6.33	70	-20.7	< -29.7	Matched	$0.53 \lambda_g \times 0.33 \lambda_g$ (54 × 34 mm ²)
[4]	1.99	-6.5	105	-22.6	-20	Matched	$0.76 \lambda_g \times 0.16 \lambda_g$
[5]	1.79	-7.7	35	-8.6	-20	Not	$0.3 \lambda_g \times 0.18 \lambda_g$
[6] Triband	2.8/4.3/5.8	-6.5/-5.4/-3	120/180/250	-21/-24/-23	-	Not	$0.387 \lambda_g \times 0.032 \lambda_g$ (22 × 2.46 mm ²)
[8]	1.57	-8.75	59.9	-20.5	< -32	Matched	$0.39 \lambda_g \times 0.19 \lambda_g$ (50 × 25 mm ²)
[9]	3.45	-4.6	120	-20.4	< -33	Matched	$0.33 \lambda_g \times 0.29 \lambda_g$ (21 × 18.5 mm ²)
[12]	1.96	-6.5	90	-21.2	< -24	Matched	-
[13]	1.016	-2.09	144	-18.1	-33	Matched	$0.41 \lambda_g \times 0.41 \lambda_g$ (85 × 85 mm ²)
[20] Dual band	2.14/3.5	-3/-3.1	150/170	-34.2/-34.9	< -17	Not	140 × 70 mm ²
[22]	2.14	-1.03	60	-3.82	-30.48	Matched	39.6 × 31 mm ²
[42]	1.2	-2.8	30	-2.2	-15	Not	64 × 32 mm ²

More signal attenuation would require more power compensation of the power amplifier.

NGD Circuit Applications

Application in a Constant Phase Shifter

NGD circuits can be used in a constant phase shifter [27], as shown in Figure 23. In this case, a traditional transmission line, which commonly has a PGD, and an NGD circuit cascade together to construct the constant phase shifter, as depicted in Figure 23(a); here, the PGD and NGD circuits must be well matched. The phase slope for the PGD is negative, while that of the NGD is positive, so the cancelled group delay (for example, the zero group delay) can be realized when the PGD and NGD circuits are cascaded, as the schematic curves in Figure 23(b) and (c) illustrate and can be expressed as $\Phi_T(f) = \Phi_1(f) + \Phi_2(f)$. Φ_1 , Φ_2 , and Φ_T are the phases for the PGD, NGD, and total circuits, respectively; the corresponding group delays are τ_1 , τ_2 , and τ_T , respectively. The schematic circuit diagram has been realized by an active circuit [27].

Application in Feedforward Amplifiers and Antenna Arrays

An NGD circuit can be used to replace the commonly used delay element in a feedforward amplifier to enhance efficiency and reduce size [25], as presented in Figure 24. NGD circuits can also be connected in the feeding line of a series feed antenna array to minimize beam-squint delay flatness [26], as shown in Figure 25, where the antenna array is constructed with amplifiers, NGD circuits,

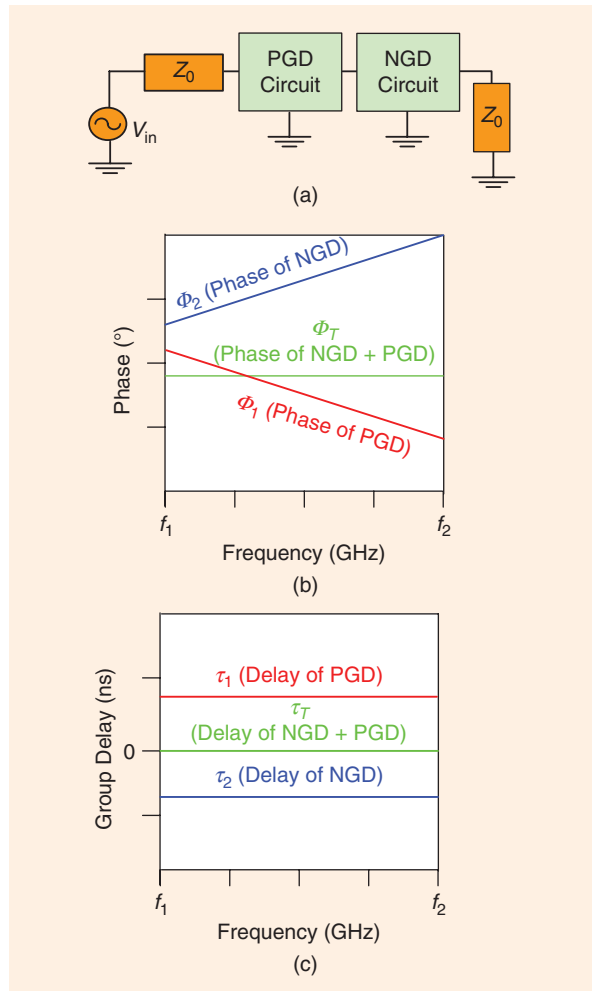


Figure 23. A schematic diagram of the constant phase shifter [27]. (a) The schematic circuit diagram. (b) The schematic phase curves. (c) The corresponding group delay.

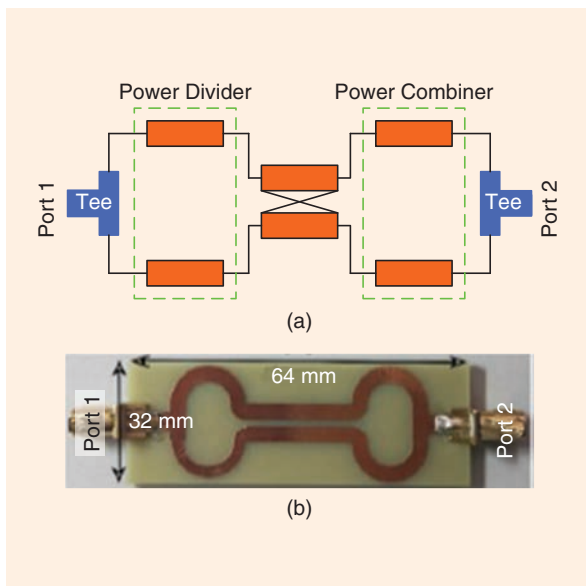


Figure 22. An O=O-shaped NGD circuit. (a) The circuit diagram and (b) the fabricated hardware [42].

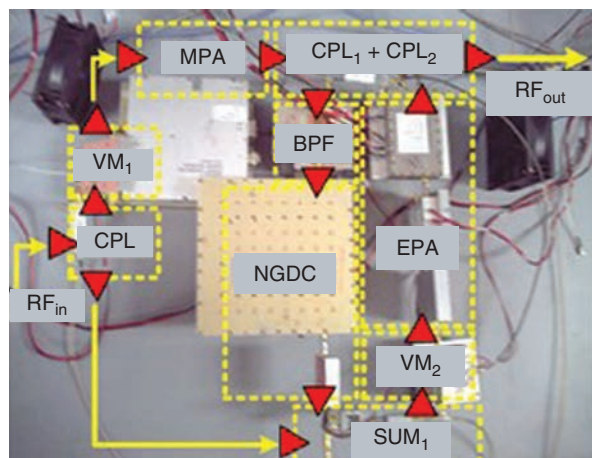


Figure 24. A feedforward topology [25]. EPA: error power amplifier; MPA: main power amplifier; VM: vector modulator; CPL: coupler; NGDC: negative group delay circuit.

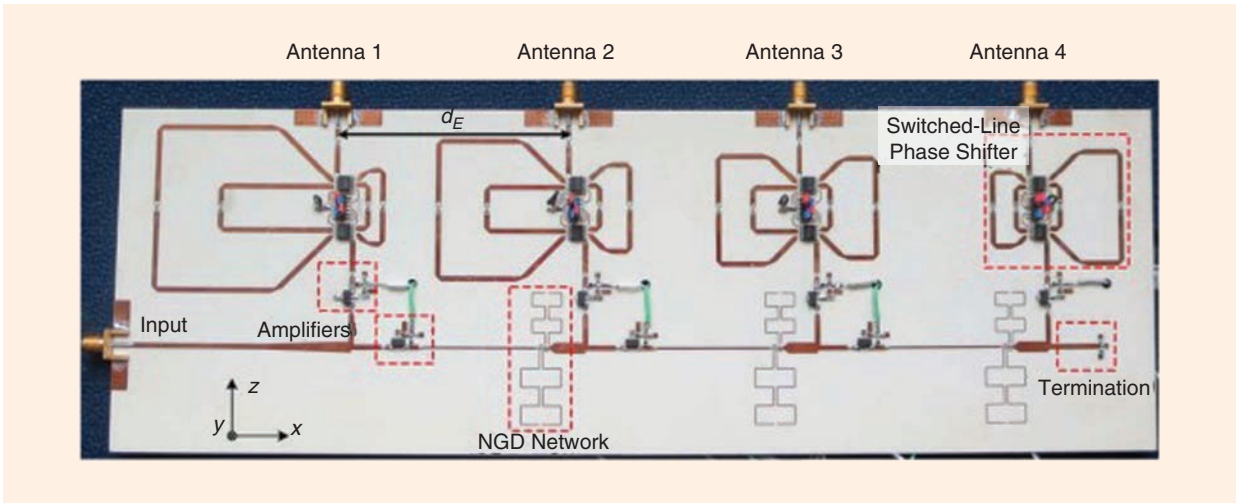


Figure 25. A series feed antenna array [26].

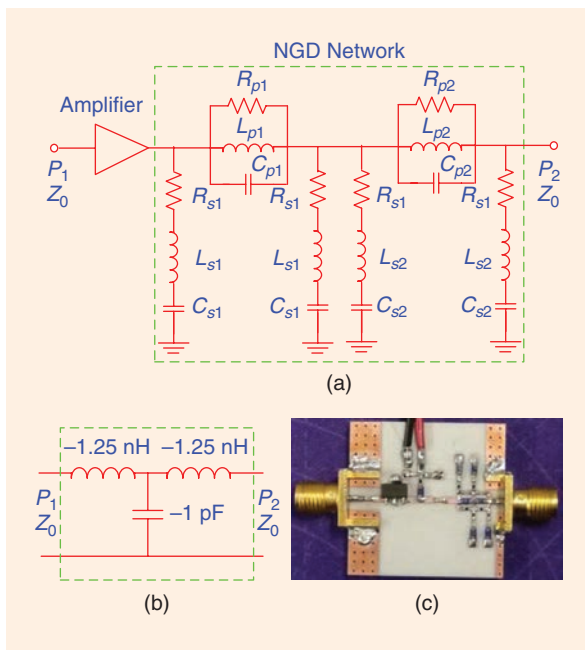


Figure 26. A unilateral non-Foster T-network [28]. (a) A schematic of the unilateral non-Foster network. (b) A unilateral non-Foster T-network. (c) The fabricated hardware.

switched line phase shifters, and termination. The signal attenuation caused by the NGD circuit can be compensated for by the amplifier behind, and the PGD caused by the amplifier itself can also be effectively eliminated.

Application in Non-Foster Reactive Elements

NGD circuits can be used to realize non-Foster reactive elements (to be specific, negative capacitors and inductors), which have many applications,

ranging from electronics and integrated-circuit design to microwaves and electromagnetics [28], such as realizing fast low-dispersion transmission lines, increasing the bandwidth of an electrostatic discharge protection unit at the input/output of a broadband amplifier, implementing a varactorless voltage-controlled oscillator (VCO), or increasing a VCO's tuning range. A unilateral non-Foster T-network that works at 1.3–2.0 GHz can be realized using an NGD network, as shown in Figure 26, where the schematic of the unilateral non-Foster network is displayed in Figure 26(a), the equivalent unilateral non-Foster T-network is shown in Figure 26(b), and the fabricated hardware is illustrated in Figure 26(c). It can be seen from Figure 26(a) that the amplifier is used to compensate for the loss of the NGD circuit, while the NGD network is a series circuit of a typical Π -shaped, lumped-element NGD circuit, as shown in Figure 1(b).

Application in Interconnection Equalization

In very-large-scale integration (VLSI) circuits with millions of transistors in a single chip, the propagation delay of the interchip interconnect cannot be neglected; it is an important issue in modern VLSI/system-on-chip designs. A new approach for propagation delay reduction is interconnect-effect equalization using an active NGD circuit [43], as shown in Figure 27(a). The circuit model is depicted in Figure 27(b), where, for achieving interconnection equalization, the terminal of the interconnection line is driven by the logic gate, while an NGD circuit is used to compensate for the PGD of the interconnection line. The interconnection equalization with active NGD circuit allows for a propagation delay reduction of no less than 50% [43].

High-speed integrated metamaterial-inspired NGD CMOS circuits in millimeter-wave frequencies have also been presented for delay equalization [44].

Application in PD Integration Circuits

PDs are important components for power dividing and combining and have wide applications in radar and

wireless communication systems such as high power amplifiers, mixers, and antenna-feeding networks. Conventional PDs have PGD [34], which has a negative influence on the performance of microwave circuits and systems. If an NGD circuit is integrated with a PD, NGD characteristics would be produced, which compensate for a PGD and eliminate the need for a delay compensation element or attenuator.

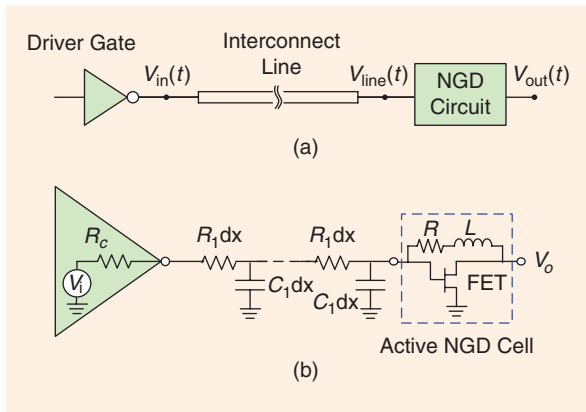


Figure 27. The interconnection equalization with an active NGD circuit [43]. (a) A schematic of the interconnect line with an NGD circuit. (b) The interconnection equalization circuit model. FET: field-effect transistor.

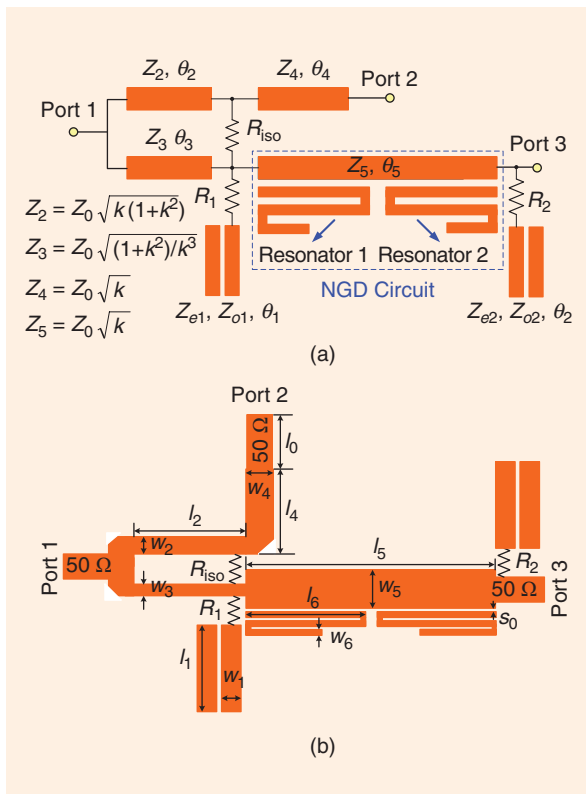


Figure 28. An unequal Wilkinson PD with NGD characteristics [10]. (a) The transmission line circuit model and (b) the physical structure of the circuit.

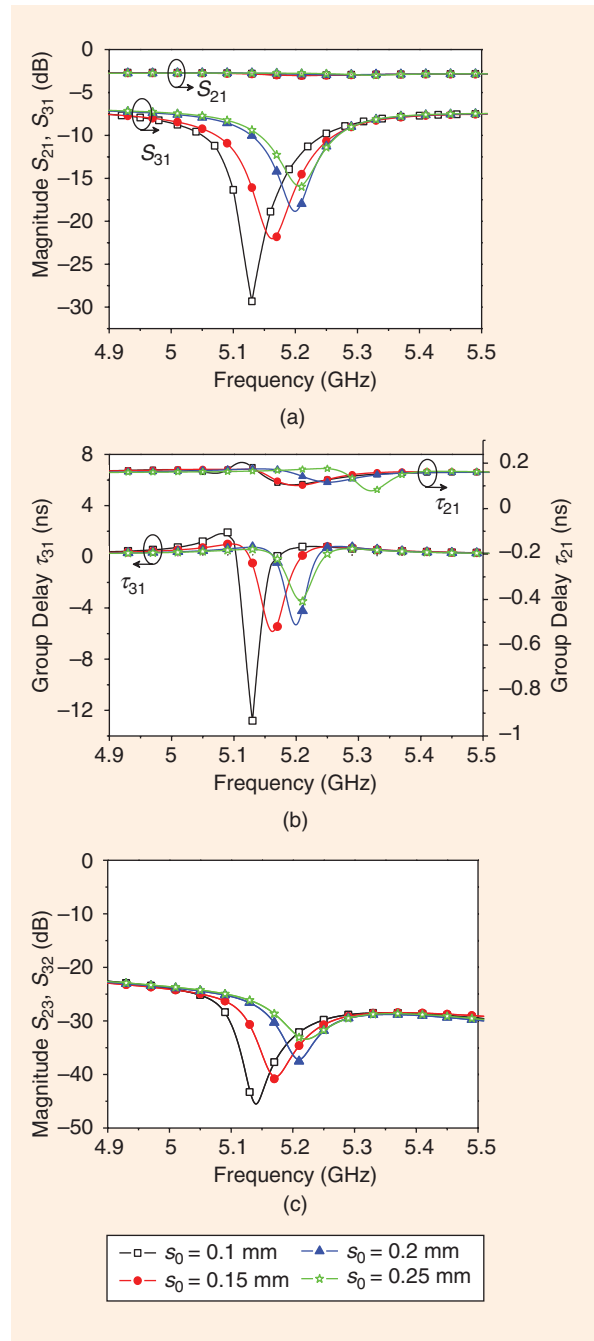


Figure 29. The simulated frequency responses of an unequal PD with NGD characteristics versus s_0 [10]. (a) S_{21}/S_{31} versus s_0 . (b) Isolation S_{23}/S_{32} versus s_0 . (c) Group delay versus s_0 .

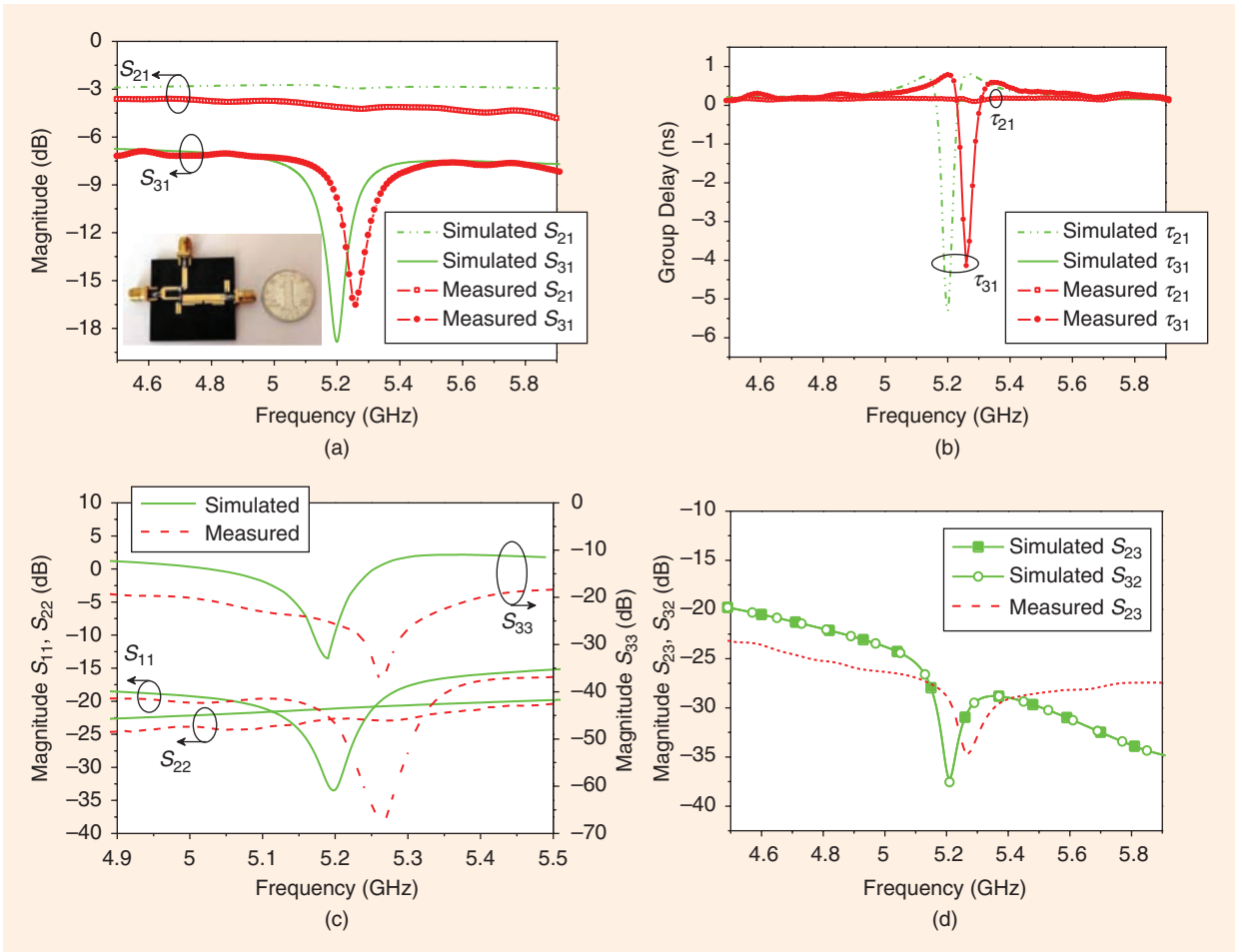


Figure 30. The fabrication and measured results of an unequal PD with NGD characteristics [10]. (a) S_{21}/S_{31} . (b) The group delay. (c) $S_{11}/S_{22}/S_{33}$. (d) An isolation comparison.

TABLE 4. The performance of the PDs with NGD characteristics.

Performance/Reference	[30]	[10]
Without an NGD circuit	PGD	PGD
NGD-BW (MHz)/ f_0 (GHz)	100/2.14	73/5.26
$S_{11}/S_{22}/S_{33}$ (dB)	-30.38/-26.76/ -28.99	-37.6/-22.7/ -37.67
S_{21}/S_{31} (dB)	-9.29/-9.3	-4.23/-16.85
Isolation (S_{23}) (dB)	-42.18	-35.06
τ_{21}/τ_{31} (ns)	-1.16/-1.17	0.14/-4.21

The unequal PD with NGD characteristics can be realized by an unequal PD integrating with an NGD circuit [10], as illustrated in Figure 28, where the transmission line circuit model with a power division ratio of k is presented in Figure 28(a) and the circuit physical structure is shown in Figure 28(b). The simulated S -parameters and group delay variations versus coupling gap s_0 are displayed in Figure 29(a)–(c), respectively. It can be seen

that S_{21} is nearly fixed, while τ_{21} has only a nonsignificant change, but S_{31} , S_{32}/S_{23} , and τ_{31} decrease with an increasing s_0 , which, for the NGD circuit, is integrated in transmission paths 1–3, not in 1–2. The variation of τ_{31} is coupled to the variation of S_{31} . From Figure 29(c), it is clear that PD isolation decreases with an increase in s_0 because that PD isolation is related to the power division ratio k and the reflection coefficient from ports 2 and 3. As $k = S_{31}/S_{21}$, the power division ratio can be changed with a change in s_0 , and the practical power division ratio would decrease with the increase in s_0 for a nearly fixed S_{21} .

The fabrication and the measurements of the unequal PD with NGD characteristics are shown in Figure 30, where the fabricated hardware and the measured S_{21}/S_{31} are depicted in Figure 30(a), the measured group delay is presented in Figure 30(b), the measured $S_{11}/S_{22}/S_{33}$ are plotted in Figure 30(c), and the measured isolation is illustrated in Figure 30(d). The simulated results are also shown for comparison. The measured results are listed in Table 4. The integration

circuit has a size of $0.86 \lambda_g \times 0.52 \lambda_g$, where λ_g is the guided wavelength at 5.2 GHz.

Another short-circuited, coupled-lines-connected PD with NGD characteristics [30] is shown in Figure 31, where the PD has an equal power division ratio and the NGD circuit is integrated in both transmission paths 1–2 and 1–3. The circuit structure and the fabricated hardware are displayed in Figure 31(a) and (b), respectively. The resistor-loaded, short-circuited coupled lines are used not only to bring NGD characteristics but also to introduce port matching for S_{11} attenuation. The resistances of the loaded resistors are R and $2R$, as shown in Figure 31(a). Both transmission paths 1–2 and 1–3 of the integration circuit have NGD characteristics because the NGD circuits are connected in both paths. The measured performance is presented in Table 4.

Conclusions and Future Developments

NGD is very useful in compensating for PGD to bring group delay flatness, which can improve communication quality. In this article, the development of NGD circuits was reviewed, and their applications in

feedforward amplifiers, phased-array antennas, constant phase shifters, non-Foster elements, interconnection equalization, and PDs were introduced.

NGD circuits can be realized based on BSFs such as stub/resonator-loaded; resonator-feed, line-coupled; and defected microstrip structure BSFs. Multiband NGD circuits can also be realized by these constructions. The desired NGD time can be controlled by the loading resistor. To attenuate the reflection wave to minimize the undesired standing waves and instability problems of a microwave system terminal, matched NGD circuits have been developed using impedance transformers, short-circuited coupled lines, and signal-interference techniques. Unlike BSFs, NGD circuits focus on NGD time and bandwidth and matching. Group delay time is associated with S_{21} .

Overall, NGD circuits are very useful for phase linearity and can be easily integrated with other components. NGD characteristics can be obtained when the corresponding transmission path is integrated with an NGD circuit. In the future, the delay variations of phase-sensitive circuits will become more important, while multilayer NGD circuits and more NGD integration circuits will be developed for circuit miniaturization and integration.

Acknowledgments

This work was supported in part by the National Natural Science Foundation of China under Grant 61871458. Jian-Kang Xiao is the corresponding author.

References

- [1] M. Kandic and G. E. Bridges, "Asymptotic limits of negative group delay in active resonator-based distributed circuits," *IEEE Trans. Circuits Syst.*, vol. 58, no. 8, pp. 1727–1735, 2011. doi: 10.1109/TCSI.2011.2107251.
- [2] G. Chaudhary, Y. Jeong, and J. Lim, "Miniaturized dual-band negative group delay circuit using dual-plane defected structures," *IEEE Microw. Wireless Compon. Lett.*, vol. 24, no. 8, pp. 521–523, 2014. doi: 10.1109/LMWC.2014.2322445.
- [3] G. Chaudhary and Y. Jeong, "Transmission-type negative group delay networks using coupled line doublet structure," *IET Microw. Antennas Propag.*, vol. 9, no. 8, pp. 748–754, 2015.
- [4] L. Qiu, L. Wu, W. Yin, and J. Mao, "Absorptive bandstop filter with prescribed negative group delay and bandwidth," *IEEE Microw. Compon. Lett.*, vol. 27, no. 7, pp. 639–641, 2017. doi: 10.1109/LMWC.2017.2711572.
- [5] G. Liu and J. Xu, "Compact transmission-type negative group delay circuit with low attenuation," *Electron. Lett.*, vol. 53, no. 7, pp. 476–478, 2017. doi: 10.1049/el.2017.0328.
- [6] J.-K. Xiao and Q.-F. Wang, "Individually controllable tri-band negative group delay circuit using defected microstrip structure," in *Proc. Cross Quad-Regional Radio Sci. Wireless Technol. Conf. (CSQRWC)*, Taiyuan, China, July 18–21, 2019, pp. 1–3. doi: 10.1109/CSQRWC.2019.8799248.
- [7] G. Chaudhary and Y. Jeong, "Low signal-attenuation negative group-delay network topologies using coupled lines," *IEEE Trans. Microw. Theory Techn.*, vol. 62, no. 10, pp. 2316–2324, 2014. doi: 10.1109/TMTT.2014.2345352.
- [8] T. Shao, Z. Wang, S. Fang, H. Liu, and S. Fu, "A compact Transmission-line self-matched negative group delay microwave circuit,"

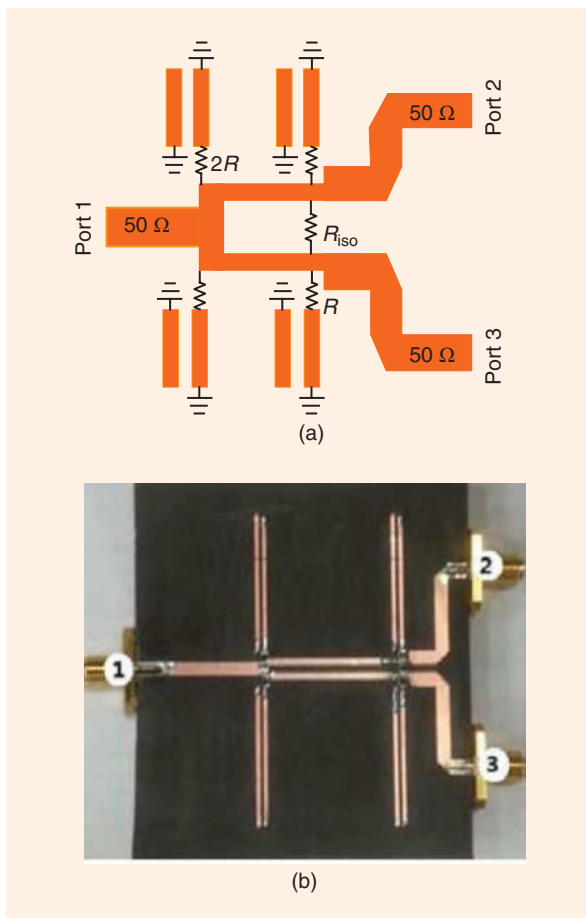
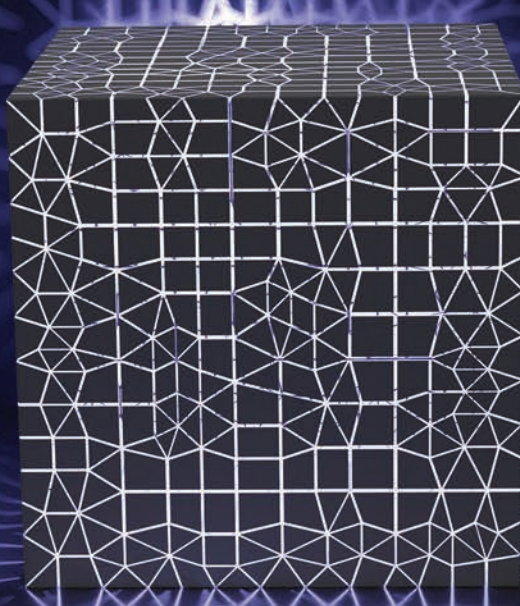


Figure 31. The PD with two-path NGD characteristics [30]. (a) The circuit topology and (b) the fabricated hardware.

- IEEE Access*, vol. 5, pp. 22,836–22,843, Oct. 2017. doi: 10.1109/ACCESS.2017.2761890.
- [9] J.-K. Xiao, Q.-F. Wang, and J.-G. Ma, “Matched NGD circuit with resistor-connected coupled lines,” *Electron. Lett.*, vol. 55, no. 16, pp. 903–905, 2019. doi: 10.1049/el.2019.1277.
- [10] J.-K. Xiao, Q.-F. Wang, and J.-G. Ma, “A matched negative group delay circuit and its integration with an unequal power divider,” *IEEE Access*, vol. 7, pp. 113,578–113,588, Aug. 2019. doi: 10.1109/ACCESS.2019.2935208.
- [11] B. Ravelo, M. Le Roy, and A. Perennec, “Application of negative group delay active circuits to the design of broadband and constant phase shifters,” *Microw. Opt. Technol. Lett.*, vol. 50, no. 12, pp. 3078–3080, 2008. doi: 10.1002/mop.23883.
- [12] G. Chaudhary, Y. Jeong, and J. Lim, “Microstrip line negative group delay filters for microwave circuits,” *IEEE Trans. Microw. Theory Techn.*, vol. 62, no. 2, pp. 234–243, 2014. doi: 10.1109/TMTT.2013.2295555.
- [13] Z. Wang, Y. Cao, T. Shao, S. Fang, and Y. Liu, “A negative group delay microwave circuit based on signal interference techniques,” *IEEE Microw. Compon. Lett.*, vol. 28, no. 4, pp. 290–292, 2018. doi: 10.1109/LMWC.2018.2811254.
- [14] Y. Wu, H. Wang, Z. Zhuang, Y. Liu, Q. Xue, and A. Kishk, “A novel arbitrary terminated unequal coupler with bandwidth-enhanced positive and negative group delay characteristics,” *IEEE Trans. Microw. Theory Techn.*, vol. 66, no. 5, pp. 2170–2184, 2018. doi: 10.1109/TMTT.2018.2809516.
- [15] H. Taher and R. Farrell, “Highly miniaturized wideband negative group delay circuit using effective negative dielectric permittivity stopband microstrip lines,” in *Proc. 46th Eur. Microw. Conf.*, London, Oct. 4–6, 2016, pp. 112–115, doi: 10.1109/EuMC.2016.7824290.
- [16] J. Jeong, S. Park, G. Chaudhary and Y. Jeong, “Design of tunable negative group delay circuit for communication systems,” in *Proc. IEEE Int. Symp. Radio-Frequency Integr. Technol. (RFIT)*, Singapore, Dec. 2012, pp. 59–61. doi: 10.1109/RFIT.2012.6401613.
- [17] J.-K. Xiao and X.-Y. Yang, “A negative group delay circuit using substrate integrated suspended line,” in *Proc. Cross Quad-Regional Radio Sci. Wireless Technol. Conf. (CSQRWC)*, Taiyuan, China, July 18–21, 2019, pp. 1–2. doi: 10.1109/CSQRWC.2019.8799288.
- [18] K. Ahn, R. Ishikawa, and K. Honjo, “Group delay equalized UWB InGaP/GaAs HBT MMIC amplifier using negative group delay circuits,” *IEEE Trans. Microw. Theory Techn.*, vol. 57, no. 9, pp. 2139–2147, Sept. 2009. doi: 10.1109/TMTT.2009.2027082.
- [19] B. Ravelo, A. Pérennec, M. Le Roy, and Y. G. Boucher, “Active microwave circuit with negative group delay,” *IEEE Microw. Compon. Lett.*, vol. 17, no. 12, pp. 861–863, 2007. doi: 10.1109/LMWC.2007.910489.
- [20] H. Choi, Y. Jeong, J. Lim, S.-Y. Eom, and Y.-B. Jung, “A novel design for a dual-band negative group delay circuit,” *IEEE Microw. Compon. Lett.*, vol. 21, no. 1, pp. 19–21, 2011. doi: 10.1109/LMWC.2010.2089675.
- [21] H. Choi, Y. Kim, Y. Jeong, and C. D. Kim, “Synthesis of reflection type negative group delay circuit using transmission line resonator,” in *Proc. 39th Eur. Microw. Conf.*, Rome, Italy, 29 Sept.–1 Oct., 2009, pp. 902–905. doi: 10.23919/EUMC.2009.5296195.
- [22] G. Chaudhary and Y. Jeon, “Negative group delay phenomenon analysis using finite unloaded quality factor resonators,” *Progr. Electromagn. Res.*, vol. 156, pp. 55–62, Jan. 2016. doi: 10.2528/PIER16041111.
- [23] C.-T. M. Wu and T. Itoh, “Maximally flat negative group-delay circuit: A microwave transversal filter approach,” *IEEE Trans. Microw. Theory Techn.*, vol. 62, no. 6, pp. 1330–1342, 2014. doi: 10.1109/TMTT.2014.2320220.
- [24] F. Wan, N. Li, B. Ravelo, J. Ge, and B. Li, “Time domain experimentation of NGD active RC-network cell,” *IEEE Trans. Circuits Syst., II, Exp. Briefs*, vol. 66, no. 4, pp. 562–566, 2019. doi: 10.1109/TCSII.2018.2870836.
- [25] H. Choi, Y. Jeong, C. D. Kim, and J. S. Kenney, “Efficiency enhancement of feedforward amplifiers by employing a negative group-delay circuit,” *IEEE Trans. Microw. Theory Techn.*, vol. 58, no. 5, pp. 1116–1125, May 2010. doi: 10.1109/TMTT.2010.2045576.
- [26] S. S. Oh and L. Shafai, “Compensated circuit with characteristics of lossless double negative materials and its application to array antennas,” *IET Microw. Antennas Propag.*, vol. 1, no. 1, pp. 29–38, 2007. doi: 10.1049/iet-map:20050229.
- [27] B. Ravelo, M. Le Roy, and A. Perennec, “Application of negative group delay active circuits to the design of broadband and constant phase shifters,” *Microw. Opt. Technol. Lett.*, vol. 50, no. 12, pp. 3078–3080, Dec. 2008. doi: 10.1002/mop.23883.
- [28] H. Mirzaei and G. V. Eleftheriades, “Realizing non-Foster reactive elements using negative group delay networks,” *IEEE Trans. Microw. Theory Techn.*, vol. 61, no. 12, pp. 4322–4332, Dec. 2013. doi: 10.1109/TMTT.2013.2281967.
- [29] T. Zhang, R. Xu, and C.-T. M. Wu, “Unconditionally stable non-foster element using active transversal-filter-based negative group delay circuit,” *IEEE Microw. Compon. Lett.*, vol. 27, no. 10, pp. 921–923, 2017. doi: 10.1109/LMWC.2017.2745487.
- [30] G. Chaudhary and Y. Jeong, “A design of power divider with negative group delay characteristics,” *IEEE Microw. Compon. Lett.*, vol. 25, no. 6, pp. 394–396, June 2015. doi: 10.1109/LMWC.2015.2421280.
- [31] G. Chaudhary and Y. Jeong, “Negative group delay phenomenon analysis in power divider: Coupling matrix approach,” *IEEE Trans. Compon. Packag. Manuf. Technol.*, vol. 7, no. 9, pp. 1543–1551, Sept. 2017. doi: 10.1109/TCPMT.2017.2696972.
- [32] G. Chaudhary, P. Kim, J. Jeong, and Y. Jeong, “A design of unequal power divider with positive and negative group delays,” in *Proc. 45th Eur. Microw. Conf.*, Paris, France, Sept. 7–10, 2015, pp. 127–130. doi: 10.1109/EuMC.2015.7345716.
- [33] B. Ravelo, “Theory of coupled line coupler-based negative group delay microwave circuit,” *IEEE Trans. Microw. Theory Techn.*, vol. 64, no. 11, pp. 3604–3611, 2016. doi: 10.1109/TMTT.2016.2604316.
- [34] M. J. Chik and K. K. M. Cheng, “Group delay investigation of rat-race coupler design with tunable power dividing ratio,” *IEEE Microw. Wireless Compon. Lett.*, vol. 24, no. 5, pp. 324–326, May 2014. doi: 10.1109/LMWC.2014.2309085.
- [35] F. Wan et al., “Design of multi-scale negative group delay circuit for sensors signal time-delay cancellation,” *IEEE Sensors J.*, vol. 19, no. 19, pp. 8951–8962, 2019. doi: 10.1109/JSEN.2019.2921834.
- [36] H. Nyquist and S. Brand, “Measurement of phase distortion,” *Bell Syst. Tech. J.*, vol. 9, no. 3, pp. 522–549, 1930. doi: 10.1002/j.1538-7305.1930.tb03215.x.
- [37] H. Noto, K. Yamauchi, M. Nakayama, and Y. Isota, “Negative group delay circuit for feed-forward amplifier,” in *Proc. IEEE/MTT-S Int. Microw. Symp.*, June 2007, pp. 1103–1106. doi: 10.1109/MWSYM.2007.380286.
- [38] Q. Zhang, D. L. Sounas, S. Gupta, and C. Caloz, “Wave-interference explanation of group-delay dispersion in resonators [Education Column],” *IEEE Antennas Propag. Mag.*, vol. 55, no. 2, pp. 212–227, Apr. 2013. doi: 10.1109/MAP.2013.6529352.
- [39] M. Kitano, T. Nakanishi, and K. Sugiyama, “Negative group delay and superluminal propagation: An electronic circuit approach,” *IEEE J. Sel. Topics Quantum Electron.*, vol. 9, no. 1, pp. 43–51, Feb. 2003. doi: 10.1109/JSTQE.2002.807979.
- [40] H. Jin, Y. Zhou, Y. M. Huang, and S. Ding, “General condition to achieve negative group delay transmission in coupled resonator structure,” in *Proc. Progr. Electromagn. Res. Symp.*, Singapore, Nov. 19–22, 2017, pp. 2956–2960. doi: 10.1109/PIERS-FALL.2017.8293639.
- [41] D. M. Pozar, *Microwave Engineering*, 3rd ed., Hoboken, NJ: Wiley, 2005.
- [42] F. Wan, N. Li, B. Ravelo, and J. Ge, “O=O shape low-loss negative group delay microstrip circuit,” *IEEE Trans. Circuits Syst., II, Exp. Briefs*, vol. 67, no. 10, pp. 1795–1799, Oct. 2020. doi: 10.1109/TCSII.2019.2955109.
- [43] B. Ravelo, A. Pérennec, and M. L. Roy, “Experimental validation of the RC-interconnect effect equalization with negative group delay active circuit in planar hybrid technology,” in *Proc. 13th IEEE Workshop Signal Propag. Interconnects (SPI’09)*, Strasbourg, France, 2009, pp. 1–4. doi: 10.1109/SPI.2009.5089836.
- [44] S. K. Podilchak, B. M. Frank, A. P. Feundorfer, and Y. M. M. Antar, “High speed metamaterial-inspired negative group delay circuits in CMOS for delay equalization,” in *Proc. 2nd Microsyst. Nanoelectron. Res. Conf.*, Ottawa, Canada, Oct. 14, 2009, pp. 9–12. doi: 10.1109/MNRC15848.2009.5338974.





Waveguide Components Based on Multiple-Mode Resonators

*Sai-Wai Wong, Jing-Yu Lin, Yang Yang,
Zai-Cheng Guo, Lei Zhu, and Qing-Xin Chu*

Sai-Wai Wong (wsw@szu.edu.cn) is with the College of Electronics and Information Engineering, Shenzhen University, China. Jing-Yu Lin (l.j.2014@ieee.org) and Yang Yang (yang.yang-1@uts.edu.au) are with the School of Electrical and Data Engineering, University of Technology, Sydney, Australia. Zai-Cheng Guo (yb67454@umac.mo) and Lei Zhu (leizhu@um.edu.mo) are with the Department of Electrical and Computer Engineering, University of Macau, Macau, China. Qing-Xin Chu (qxchu@scut.edu.cn) is with the School of Electronics and Information Engineering, South China University of Technology, Guangzhou, China.

Digital Object Identifier 10.1109/MMM.2020.3035863

Date of current version: 11 January 2021

Waveguide components have been widely explored for several decades, due to their inherent merits of low insertion losses, high quality (Q) factors, and a significant power-handling capacity. Historically, cavity-based narrowband filters and multiplexers have been explored and designed for base stations and satellite applications. Compared with using single-mode resonators (SMRs), the implementation of multiple-mode resonators (MMRs) in waveguide structures is a promising solution to dramatically reduce the circuit volume and improve the frequency selectivity. Taking advantage of MMR techniques, various innovative waveguide structures have been proposed for a wide range of application scenarios. This article presents an overview of advances in microwave multiple-mode waveguide components, including narrow-, wide-, and multiband filters; multiplexers; three-state diplexers; crossovers; and balanced/unbalanced elements. Representative examples and their results are comprehensively discussed and summarized.

Advantages of MMRs

Composite signals can be represented as a combination of multiple sinusoidal signals with varying frequencies, phases, and amplitudes. In general, these critical features can be manipulated by microwave components for different application scenarios. As the indispensable part of most microwave components, microwave resonators play a significant role in functional circuit designs. Single-resonance (single-mode) circuits in one order and in higher orders have dominated in microwave circuits and systems in industry. For high-power applications, such as base stations, satellite communication, and aerospace communication, conventional SMR waveguide components have the advantage of achieving high performance and meeting required precision performance specifications. However, their bulky circuit volume and high fabrication cost hinder their implementation in many

space-constrained scenarios. There is a need to tackle these challenges by means of a novel approach. MMRs, with more than one resonant mode in a single resonator, have been investigated by several research groups during the past decade. Besides their merits of circuit miniaturization, low loss, and low cost compared to SMRs, MMRs have the inherent advantage of diverse topologies with better out-of-band signal attenuation, due to the generation of additional transmission zeroes (TZs). In addition, MMRs provide more design freedom and flexibility in function integration, which might not be possible using single-mode resonators.

MMRs can be used in many microwave component designs. As shown in Figure 1, a microwave filter can be achieved using MMRs with improved bandwidth and out-of-band signal suppression. Further expanding this concept, out-of-phase and in-phase performance can be achieved in a three-port network for implementations of baluns and power dividers, respectively, while maintaining the merits of in-band and out-of-band operation. These three fundamental components focus on the manipulation of a single signal with one operational frequency, f . In the case of several signals resonating at different frequencies, multiplexing is a one-to- N system that separates desired signals from corresponding channels, where the outputs are isolated from each other. On the other hand, an N -to- N system can be considered a combination of multichannel filters because the same/different signals from N inputs transmit to their respective outputs.

MMRs based on planar structures were discussed for the first time in [1] and include microstrip lines, coplanar waveguides, and hybrid assemblies. The authors of [2] present state-of-the-art substrate-integrated waveguide filters; [3]–[5] offer a detailed analysis and explanation of waveguide-based filters. The current article reviews the latest microwave waveguide components based on MMRs, which can be categorized as dual-mode resonators [6], triple-mode resonators (TMRs), quadruple-mode resonators, and MMRs (more than four modes).

Characteristics of Multiple Resonance Modes

A model of a rectangular cavity is presented in Figure 2(a); the length, width, and height are denoted as a , b , and c , respectively. The cavity is covered by metal, which can be regarded as the electric wall. Inside the cavity is a vacuum. Therefore, the resonant frequencies of the proposed rectangular waveguide modes can be expressed as

$$\omega_{m,n,l}^2 = \frac{v^2}{\epsilon_r \mu_r} \left[\left(\frac{m\pi}{a} \right)^2 + \left(\frac{n\pi}{b} \right)^2 + \left(\frac{l\pi}{c} \right)^2 \right] \quad (1)$$

where $\omega_{m,n,l}$ stands for the resonant angular frequencies of the specific modes (m , n , and $l = 0$ or 1), while v represents the speed of light in the air. Here, ϵ_r and μ_r are the permittivity and the permeability of the air of the cavity, respectively. Therefore, the resonant

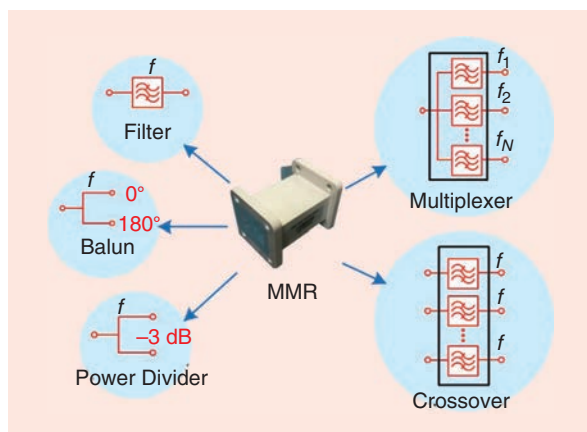


Figure 1. Categories of microwave passive components.

frequencies of three fundamental modes, namely, TE_{011} , TE_{101} , and TM_{110} , can be obtained from (1):

$$\omega_{0,1,1}^2 = \frac{v^2}{\epsilon_r \mu_r} \left[\left(\frac{\pi}{b} \right)^2 + \left(\frac{\pi}{c} \right)^2 \right], \quad (2a)$$

$$\omega_{1,0,1}^2 = \frac{v^2}{\epsilon_r \mu_r} \left[\left(\frac{\pi}{a} \right)^2 + \left(\frac{\pi}{c} \right)^2 \right], \quad (2b)$$

$$\omega_{1,1,0}^2 = \frac{v^2}{\epsilon_r \mu_r} \left[\left(\frac{\pi}{a} \right)^2 + \left(\frac{\pi}{b} \right)^2 \right]. \quad (2c)$$

Using (2a)–(2c), the resonant frequencies of three fundamental modes can be independently determined and designed. The electric field distributions of these rectangular cavity modes are shown in Figure 2(b)–(m). Compared with the first harmonic modes [Figure 2(e)–(j)], second harmonic modes [Figure 2(k)–(m)], and higher harmonic modes, three fundamental modes [Figure 2(b)–(d)] resonate at the lowest frequencies, which

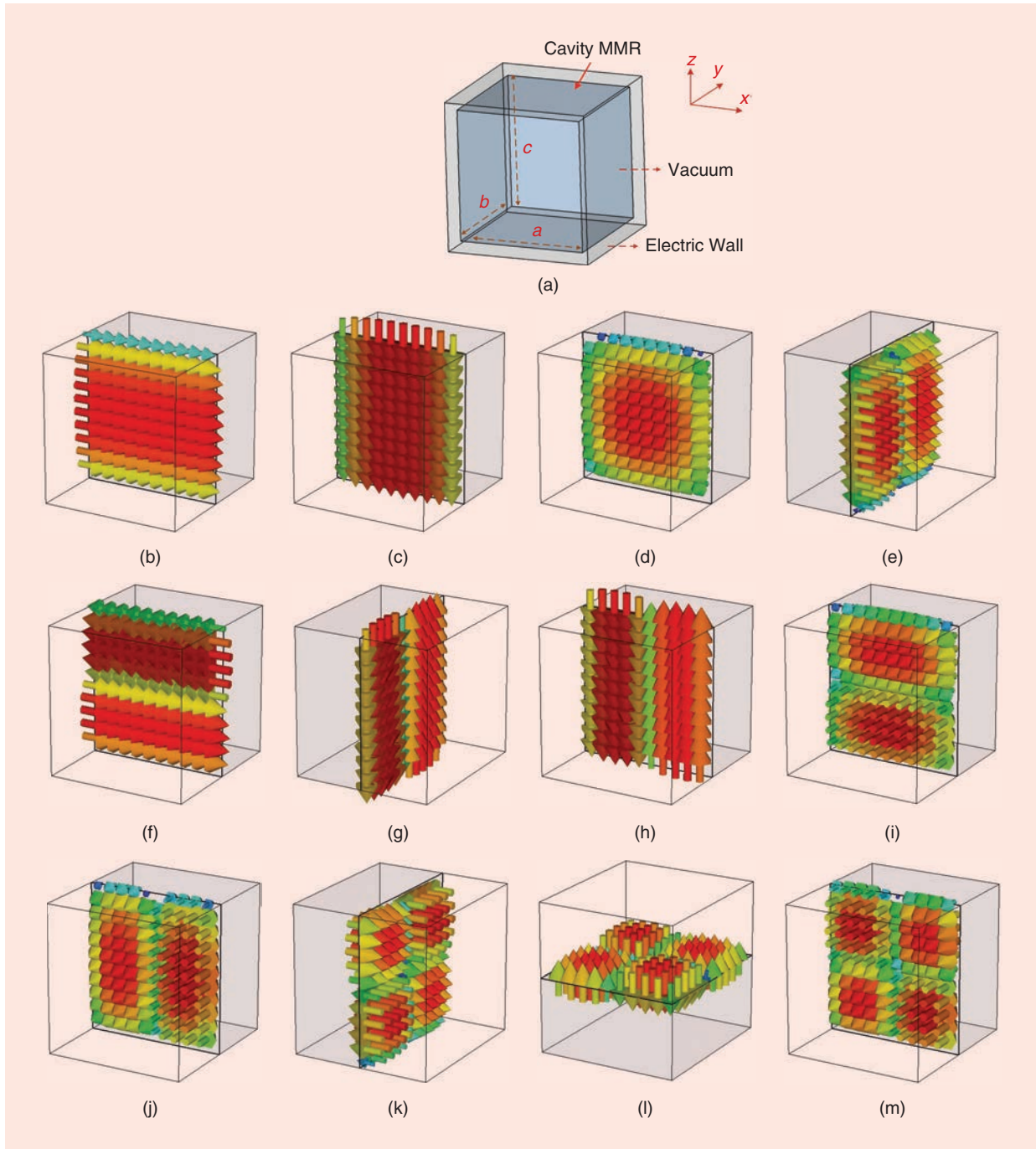


Figure 2. (a) A model of a rectangular cavity. An electric field distribution with (b) TE_{011} , (c) TM_{110} , (d) TE_{101} , (e) TE_{021} , (f) TE_{012} , (g) TM_{120} , (h) TM_{210} , (i) TE_{102} , (j) TE_{201} , (k) TE_{022} , (l) TM_{202} , and (m) TE_{202} .

guarantees a compact circuit volume in terms of the selected resonant modes.

Design Examples: MMR-Based Waveguide Components

Narrowband Filters

Filters are primarily used in microwave components, and they can be generally categorized as narrowband, wideband, and multiple band. Due to the high unloaded Q factors (Q_u) of cavity resonators, cavity-based narrowband filters have long been investigated. In this section, we introduce narrowband filters based on different MMRs distinguished by the number of intrinsic operating modes.

Dual-Mode Resonators

Typically, there are two types of modes used in dual-mode resonators: 1) TM_{120}/TM_{210} harmonic modes [7]–[10] and 2) TE_{011}/TE_{101} fundamental modes [11]–[13]. First, we discuss the TM_{120}/TM_{210} modes. Figure 3(a) presents a sixth-order filter topology based on three TM_{120}/TM_{210} doublets connected by nonresonating nodes (NRNs), while the proposed filter is pictured in Figure 3(b). As explained in [7], each of this type of doublet can generate two TZs, at most. Figure 3(c) illustrates that the filter passband is centered at 10 GHz, with a fractional bandwidth of 1.5% and a measured insertion loss of 0.6 dB. A

maximum of six TZs is generated and located beside the passband to increase the high selectivity of the filter.

In [8], instead of using a doublet topology, this pair of TM_{120}/TM_{210} modes is arranged by a direct-coupling arrangement to form an eighth-order filter with eight TZs symmetrically located at the lower and upper stopbands. In [9], a dielectric resonator (DR) is installed within the cavity to further decrease the structure volume; thus, an eighth-order symmetric filter composed of four DRs is designed at 1.95 GHz, with a bandwidth of 67 MHz and a measured insertion loss of 0.5 dB.

Here, we discuss the use of TE_{011}/TE_{101} modes. In [11], tuning screws are inserted inside the cavity resonator to simultaneously excite the proposed dual modes. In [13], without any additional elements installed in the cavity, a pair of cross-rotated slots is placed at the surface center of the cavity resonator to excite the TE_{011}/TE_{101} doublet with the generation of one TZ. This TZ can be placed at the lower or upper stopband, depending on the rotated angle of the slots.

TMRs

Another type of structural topology, namely, a $TE_{011}/TE_{101}/TM_{110}$ triplet, is depicted in the inset of Figure 4(a). It can be seen that three fundamental modes are located in parallel and coupled with the source and the load, respectively. Narrowband filter designs based on TMRs can be found in [12]–[20]. According to this

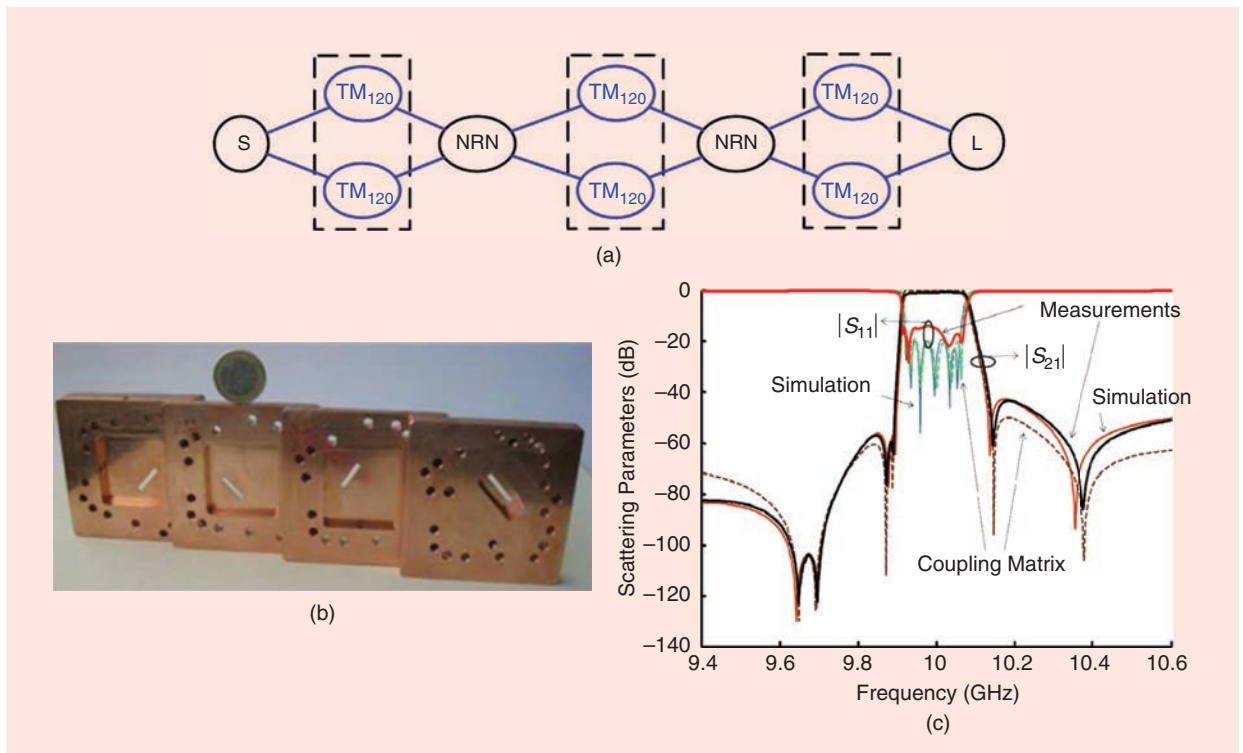


Figure 3. A transverse magnetic (TM) dual-mode sixth-order filter with (a) a doublet topology connected by NRNs and (b) three cavity resonators. (c) A comparison of the simulated and measured results [7].

topology, a geometrical configuration of the designed triple-mode filter is proposed in Figure 4(a) and explained in [13] and [14]. Three fundamental modes in this cavity resonator can be simultaneously excited by virtue of a pair of rotated and offset slots. Figure 4(c) details the implementation of a third-order frequency response with one TZ on the left and another one on the right of the passband. This filter resonates at 2.99 GHz, with a fractional bandwidth of 1% and a measured insertion loss of 0.5 dB. The out-of-band attenuation at both sides of the desired passband gets a sharp skirt and achieves an attenuation level that is better than 30 dB.

Another approach to achieving narrowband performance is the installation of a DR in the metal cavity [15]. The proposed filter resonates at a center frequency of 2.53 GHz, with a fractional bandwidth of 2.7% and a measured insertion loss of 0.4 dB. Furthermore, in [19], this triplet topology is extended and enriched by adding four more resonators to achieve a seventh-order narrowband filter. Based on a slab–slab–cube–slab–slab structure, the silver-plated ceramic cavity filter achieves 1 dB of band edge insertion loss, with a fractional bandwidth of 4% and more than 50 dB of attenuation.

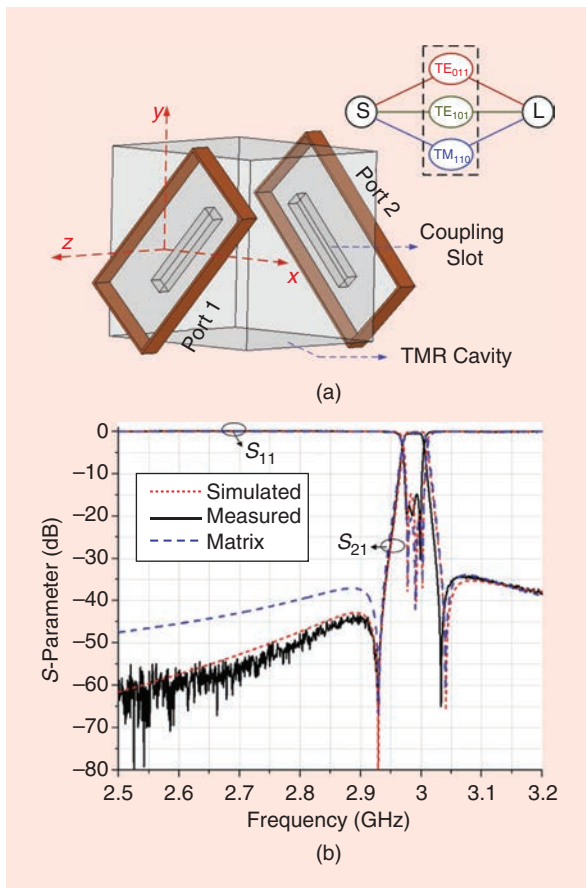


Figure 4. (a) A triple-mode filter with a geometrical configuration using one TMR. (b) A comparison of the simulated and measured results [14].

Quadruple-Mode Resonators

Several researchers are focused on quadruple-mode resonators [21]–[24]. In [21], as documented in the inset of Figure 5(a), a quadruplet is presented that combines two doublets: a TE_{011}/TE_{101} doublet and a TM_{120}/TE_{210} doublet. Therefore, two TZs are generated and controlled independently. The geometrical configuration is depicted in Figure 5(a); a pair of cross-rotated slots is placed at the left and right sides of the cavity resonator. By properly arranging the resonant frequencies of four modes within a frequency range, a fourth-order response forms, with one TZ at the lower stopband and one TZ at the upper stopband, as shown in Figure 5(b). In [22], the proposed quadruple-mode resonator is made up of four inner conductive posts within a single cavity, which improves the unloaded Q values. Furthermore, four TZs are generated due to multiple cross-couplings and because of source-to-load direct coupling. From this summary of different types of MMRs, it can be seen that using more modes in a single cavity has the obvious advantage of better miniaturization. However, the design sensitivity is also increased since more parameters are required to control the relevant internal and external couplings.

Wideband Filters

Decreasing the external Q factor Q_e of a cavity resonator is the key to designing a wideband cavity filter with a fractional bandwidth that is more than 20%, which is still a

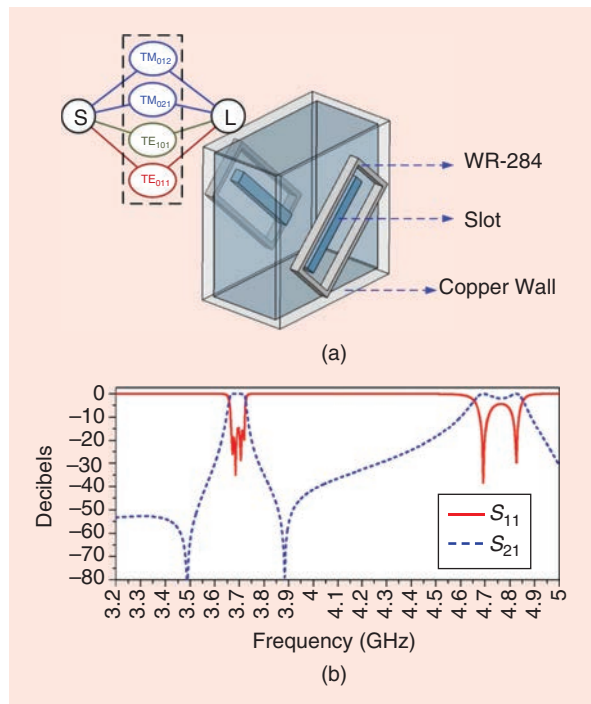


Figure 5. (a) A quadruple-mode filter with a geometrical configuration that uses one quadruple-mode resonator. (b) The simulated results [21]. WR-284: rectangular waveguide to feed.

challenging research topic. A novel wideband bandpass filter (BPF) using simple perturbation in a single metal cavity is presented in Figure 6(a) and explained in [25]. A perturbation metal cylinder is fixed at the bottom of the intracavity, with an off-centered position. The extracted Q_{es} s of the three resonant modes in the cavity are 5.13, 11.6, and 26.88, respectively, which satisfies the requirements of wideband filter designs. Figure 6(b) depicts the simulated and measured results, showing that this kind of filter resonates at a center frequency of 3.2 GHz, with a fractional bandwidth of 30% and a measured insertion loss of 0.5 dB. The group delay within the passband varies within 0.6 ns, demonstrating good linearity. Furthermore, one and two more perturbation metal rods [26] are installed at the bottom of the intracavity. Therefore, besides the three fundamental modes, one and two additional modes are excited and resonated at the central frequencies so that the bandwidth of the filter can be further enlarged.

We next focus on the relationships between fundamental modes and their harmonic modes. In [27], the center conductors of the two coaxial feed lines are perpendicular to the bottom sidewall of the cavity. They are extended into the cavity as coupling probes for exciting three triple-mode resonant modes, namely,

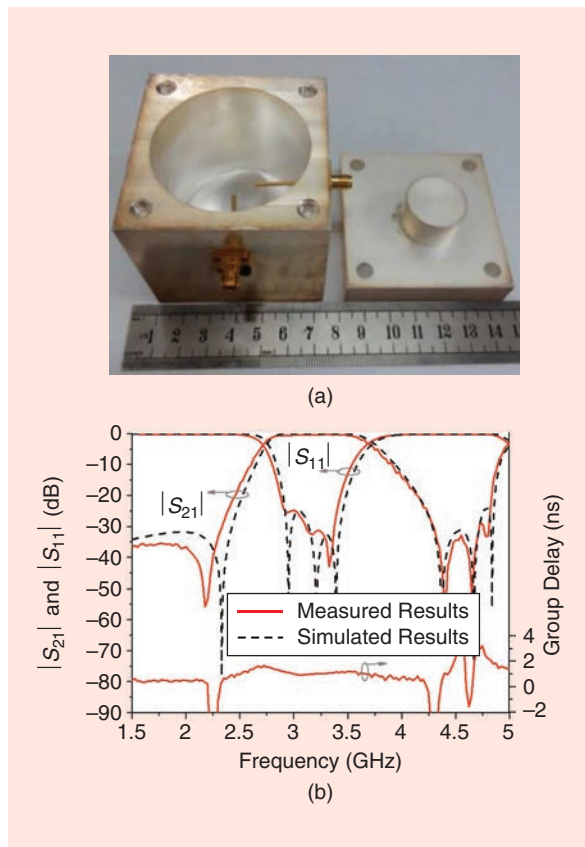


Figure 6. (a) A wideband filter that uses one metal perturbation. (b) A comparison of the simulated and measured results [25].

TM_{110} , TM_{210} , and TM_{310} . Compared with wideband filters using three fundamental modes, the proposed filter achieves a wider bandwidth, showing a fractional bandwidth of 58% at the center frequency of 5.5 GHz, with a roughly 0.5-dB measured insertion loss. In [28], a cavity is embedded within a rectangular metallic plane. The first four modes in this type of cavity (TE_{100} , TE_{101} , TE_{102} , and TE_{103}) are used to form a low-profile quadruple-mode filter. The measured passband has a center frequency of 5 GHz and a fractional bandwidth of 30%. Meanwhile, the measured insertion loss in the passband and the attenuation in the stopband are better than 0.6 and 20 dB, respectively.

Multiple-Band Filters

State-of-the-art multiple-band waveguide filters based on MMRs can be classified into two categories: dual band [29]–[32] and triple band [14], [33]–[35].

Dual-Band Filters

Generally, two bands of the designed dual-band filter are separately and independently dominated by two resonant modes of the cavity resonators. Both modes are excited at the first order and separated at the last order, which can dramatically decrease the circuit volume. In [32], the structure of the eighth-order dual-band filter consists of six TE_{112} modes and two TE_{113} modes. The elliptical cavities are designed to meet the requirement of Q_u and the spurious-free window. The filter was manufactured from an invar alloy with silver plating and is depicted in Figure 7(a). The ratio of the horizontal axis length and the vertical axis length of the elliptical cavity is approximately 1.15. An average Q_u value of 18,000 and a spurious-free window of 10–12.5 GHz is achieved. The measured return loss is better than 24 dB, and the insertion loss is 0.38 dB, as demonstrated in Figure 7(b). In [29], two fundamental modes, TE_{011} and TE_{101} , are used to independently control each band of a dual-band filter. In [31], to achieve widely separated passbands, one fundamental mode and its first-order harmonic mode are employed; the frequency ratio in this design can reach 1.5.

Triple-Band Filters

Three fundamental modes (TE_{011} , TE_{101} , and TM_{110}) are adopted to independently control each of the three bands of a triple-band filter. In [35], an elliptical-cavity triple-band filter with a third-order response is designed with an in-line configuration, which appears in Figure 8(a). Three subbands are set at the lower band (3.6–3.9 GHz), middle band (3.9–4.1 GHz), and higher band (4.1–4.4 GHz), respectively. The measured return loss is better than 20 dB, and the rejection between adjacent channels is more than 50 dB. The measured insertion loss is 0.22–0.25 dB. In [34], a fourth-order C-band triple-band filter is manufactured

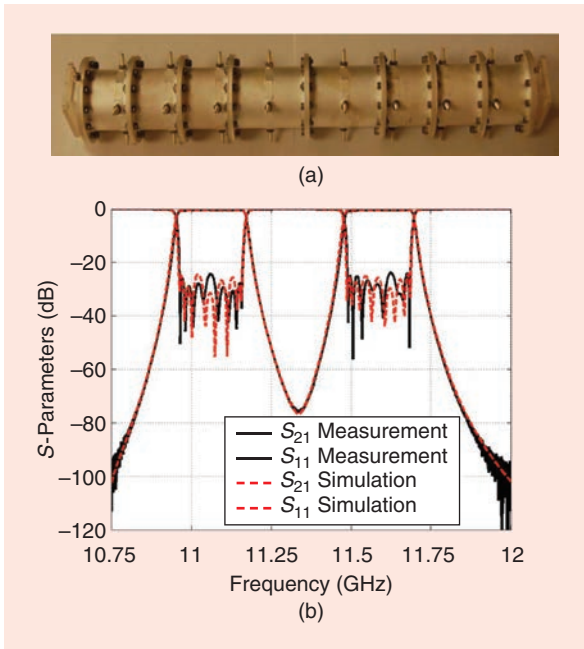


Figure 7. (a) A fabricated dual-band, eighth-order filter. (b) A comparison of the simulated and measured results [32].

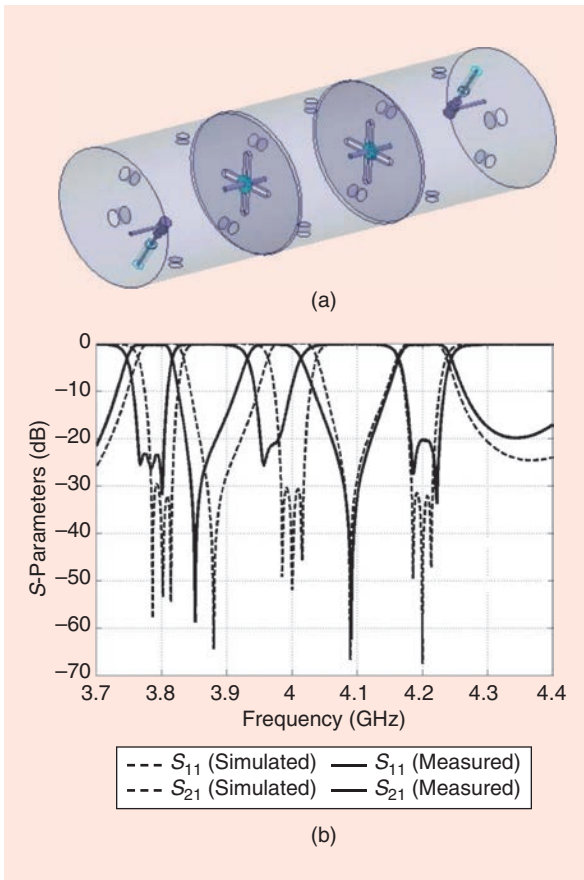


Figure 8. (a) The geometrical configuration of the triple-band, third-order filter. (b) A comparison of the simulated and measured results [35].

at the center frequencies of 3.6, 3.8, and 4 GHz, respectively, where the absolute bandwidths are all 20 MHz. The measured insertion losses, ranging from 0.38 to 0.46 dB, reflect a loaded Q in the range of 7,800–8,500.

Baluns and Balanced Circuits

A series of cavity-based baluns and balanced circuits is designed by means of the out-of-phase performance of the resonant modes in [36]–[40]. The authors of [36]–[39] present balun and balanced filter designs that are achieved by properly mounting a DR in the metal cavity. In [39], a balanced filter is designed using a dual-mode, cross-shaped DR, which is dominated by a pair of $TE_{11\delta}$ orthogonal modes. The proposed balanced filter resonates at 1.78 GHz, with a fractional bandwidth of 1.3% and an insertion loss of 0.8 dB. Similarly, the proposed balun resonates at 1.78 GHz, with a fractional bandwidth of 1.3%. The amplitude imbalance and the phase imbalance are within 0.25 dB and $180 \pm 1.2^\circ$ across the passband, respectively.

In [40], a total of four types of baluns and balanced diplexers are presented and explained in detail; the architectures

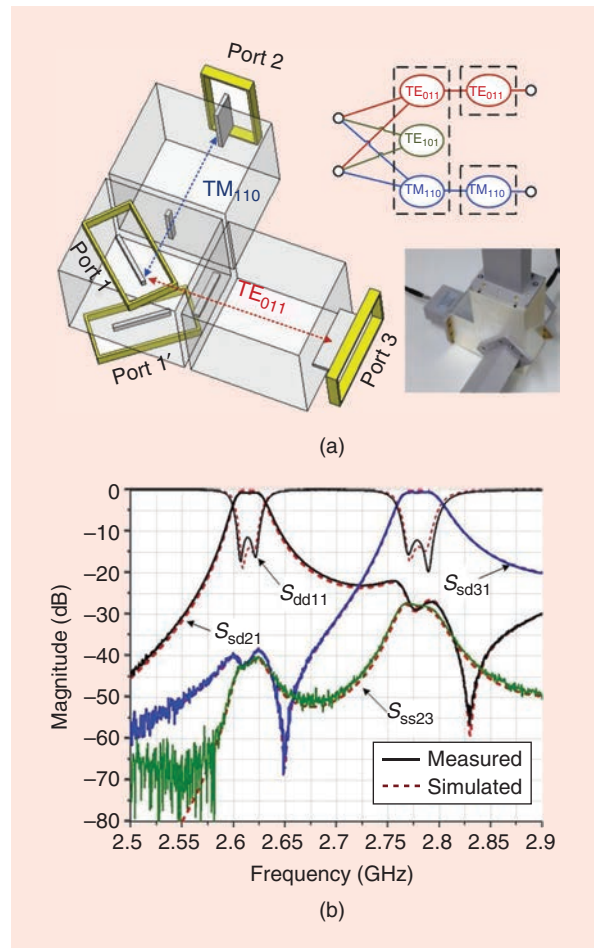


Figure 9. A balun diplexer based on TMRs with (a) a geometrical configuration that has a fifth-order topology and (b) mixed-mode S-parameter responses [40].

utilize the out-of-phase performance of each of three fundamental modes. It is noted that, to simultaneously achieve balun function in both channels of the diplexer, these two modes excited by the balanced input ports should be reversed at the same time. As depicted in Figure 9(b), a pair of coupling slots forms a cross, with offsetting along the y -axis to simultaneously excite the out-of-phase TE_{011} and TM_{110} modes. The TM_{110} mode propagates into port 2, while the TE_{011} mode propagates into port 3. Figure 9(b) shows the mixed-mode S-parameters of the balun diplexer. It can be seen for the differential mode response that the TE_{011} mode resonates at 2.61 GHz with a 3-dB bandwidth of 30 MHz, while the TM_{110} mode resonates at 2.78 GHz with a 3-dB bandwidth of 43 MHz. The isolation between ports 2 and 3 is 25 dB from 2.5 to 2.9 GHz.

Magic Ts

A magic T is a type of four-port power divider that also has in-phase and out-of-phase signals; isolation between outputs can be implemented with an isolation port instead of a lossy resistor. Broadband waveguide magic Ts are studied in [41] and [42]. The authors of [43] present a filtering magic T that uses MMRs. Based on this structure, balanced functions are integrated at the input ports, as shown in the geometrical structure of the balanced-to-unbalanced filtering magic T in Figure 10(a). Figure 10(b) demonstrates that two differential-mode channels have the same resonant frequencies, resonating at 2.74 GHz with a 40-MHz fractional bandwidth and a measured insertion loss of 3.17 dB. Duplexing function integration is also explored in [43]. The designed structure has two

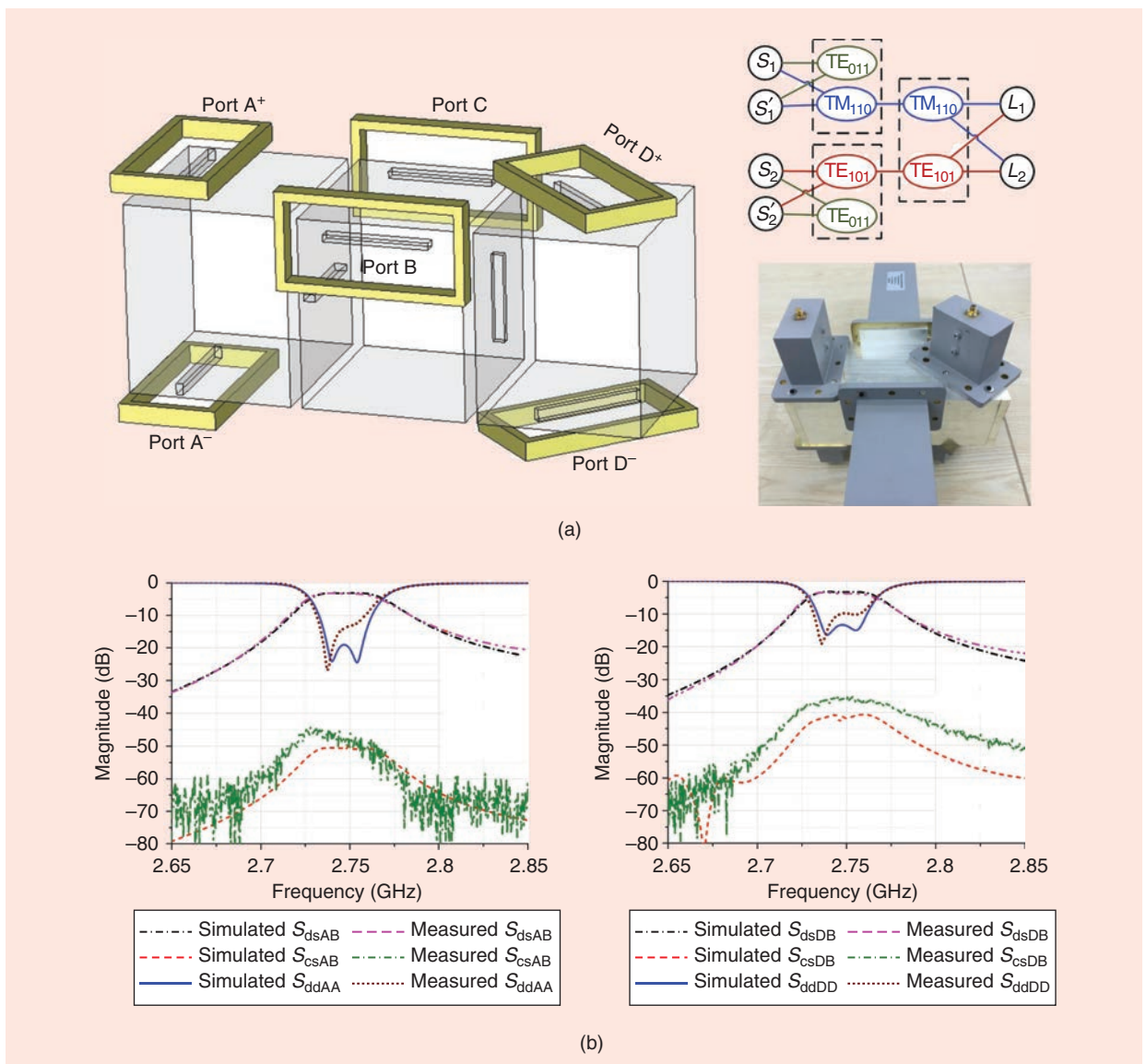


Figure 10. A balanced-to-unbalanced magic T based on TMRs with (a) a geometrical configuration that has a fifth-order response and (b) mixed-mode S-parameter responses [43].

channels resonating at 2.58 and 2.76 GHz, with a fractional bandwidth of 20 and 32 MHz, respectively.

Multiplexers

MMR-inspired multiplexers can be categorized into four types: 1) diplexer, 2) triplexer, 3) multiplexer, and 4) three-state diplexer.

Diplexers

According to conventional diplexer design, the first step is to implement two BPFs, one at the lower band and the other at the upper band. The matching network between the input and the two filters is explained in [44]–[50]. Therefore, BPFs play a key role in determining the performance of a diplexer that uses traditional design methods. Herein, we present a variety of diplexers [28], [44]–[47] based on MMR BPFs.

Figure 11(a) presents the internal view of a manufactured diplexer, which is explained in [44]. The diplexer has been confirmed to operate in two prescribed bands with the central frequencies of 2.55 and 2.66 GHz, and each passband has an absolute bandwidth of roughly 80 MHz. Three TZs are located at the lower and upper stopbands to achieve a sharp roll-off rate. The measured minimum insertion losses are 0.63 and 1.1 dB in the two passbands, respectively. The output isolation ($|S_{32}|$) is also measured, which is better than 18 dB from 2.4 to

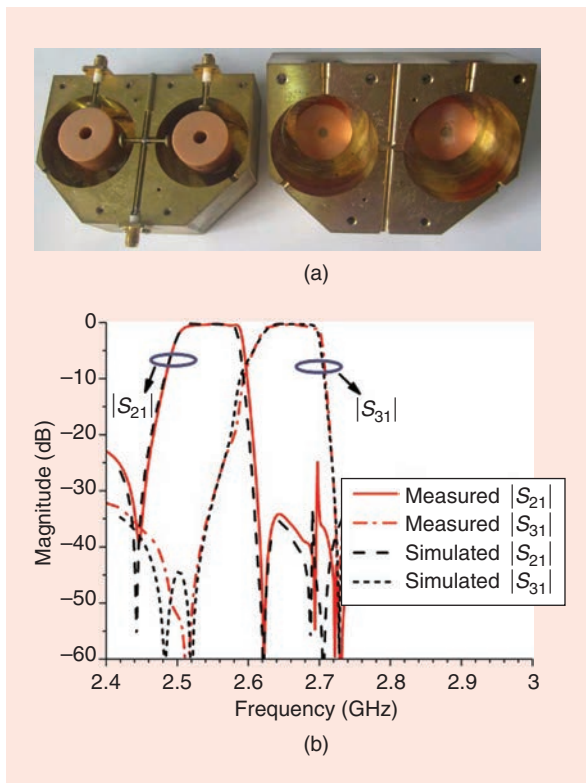


Figure 11. (a) A narrowband DR-based diplexer. (b) A comparison of the simulated and measured results [44].

2.7 GHz. In [38], to achieve a high-order response, two ceramic cuboids are cascaded to achieve six-pole pass-band responses in each band of the proposed diplexer. The proposed MMR diplexer has a measured insertion loss of 1.2 dB at 1,785 MHz for the receiver side and 1.1 dB at 1,805 MHz for the transmitter side.

The research mentioned previously [44]–[47] focuses on narrowband diplexers. In [28], we present a type of wideband, low-profile cavity-based diplexer. The two distinctive filtering channels are connected in shunt using a T-shaped feeding circuit. The lower-frequency channel of the developed diplexer has a center frequency at 3.4 GHz, with a fractional bandwidth of 29.4%, while the higher frequency channel has a center frequency at 4.7 GHz, with a fractional bandwidth of 21.3%. In addition, the measured insertion losses in the lower- and higher-frequency passbands or channels are lower than 0.9 dB.

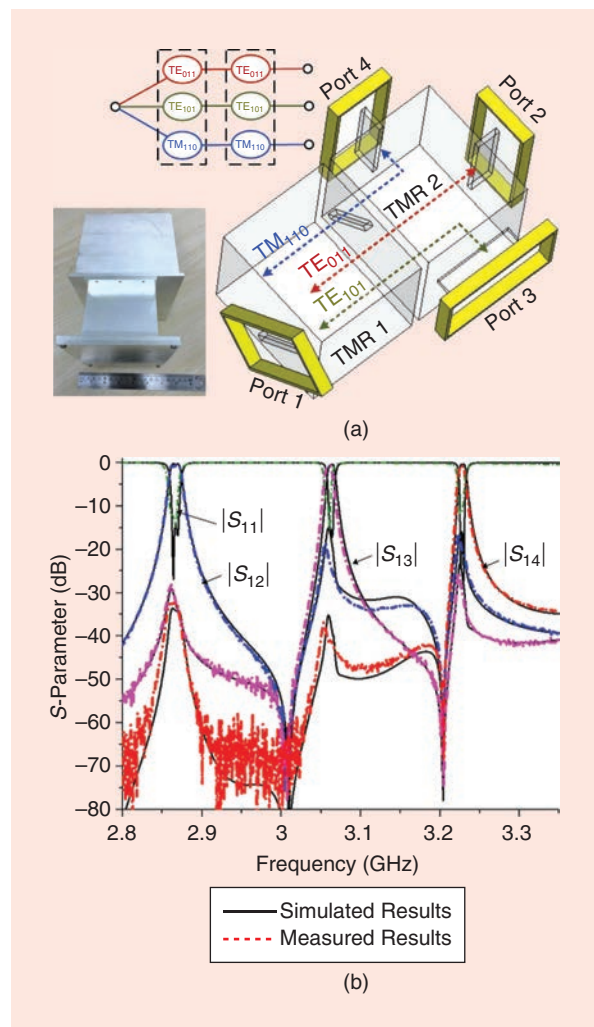


Figure 12. (a) A triplexer based on TMRs with a geometrical configuration that has a second-order response. (b) A comparison of the simulated and measured results [51].

Triplexers

In this section, a triplexer is investigated and designed using the triple-mode approach. The presented topology is depicted in the inset of Figure 12(a). Three fundamental modes in a TMR are simultaneously excited at port 1. Due to modal orthogonality, they can be propagated into their respective loads, which act as the outputs of the proposed triplexer. In addition, each channel dominated by these modes of the triplexer will be isolated from the others. Based on this, a geometrical configuration with a second-order filtering response is presented in Figure 12(a) and fully explained in [51]. Figure 12(b) illustrates the simulated and measured results of the proposed triplexer. Three passbands operate at the central frequencies of 2.87, 3.06, and 3.23 GHz, with 3-dB bandwidths of 15, 11, and 9.5 MHz, respectively. The measured insertion losses in these three passbands are equal to 0.6, 1, and 1 dB, respectively, while the isolation among these three bands is better than 20 dB. Furthermore, as presented in [51], the port-to-port isolation of a triplexer can be further improved by adding more resonators. A geometrical configuration of a triplexer with one TMR and three SMRs is proposed

to implement the second-order response triplexer, and three fundamental modes are separated in the first order. The presented triplexer design approach has the advantage of adopting fewer resonators and omitting the occupation of channel division junctions.

Multiplexers

Research by the authors of [52]–[54] shows that a multiplexer can be composed of MMRs and a manifold-matching junction, as detailed in Figure 13(a). Due to the high selectivity and sharp out-of-band rejection of the filter elements, the components can be placed close to one another to prevent wasting frequency resources. A broadband waveguide-contiguous output multiplexer is presented in [53]; the two utilized dual-mode resonators are coupled in line to form a fourth-order filter with two TZs. The proposed filters also possess at least 30% more spurious-free range in both the Ku and the C bands, which ensures enough frequency space for the multiplexer design. A manufactured three-channel multiplexer appears in Figure 13(b); the measured results show excellent agreement with the theoretical

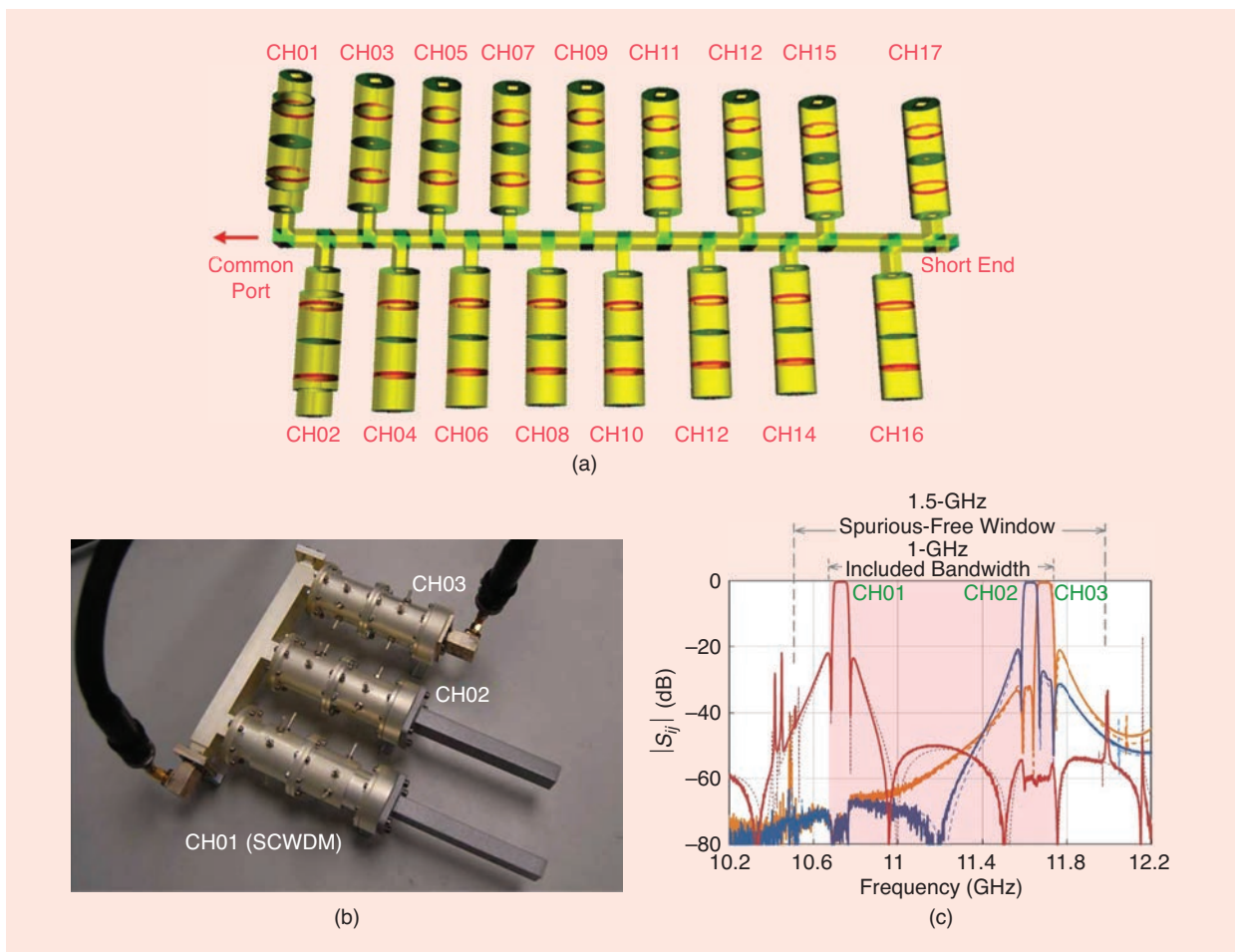


Figure 13. (a) The topology of a 17-channel multiplexer. (b) A fabricated three-channel multiplexer based on dual-mode resonators. (c) A comparison of the simulated and measured results [53]. CH: channel; SCWDM: stepped circular waveguide, dual mode.

electromagnetic designs, as plotted in Figure 13(c). In [54], a dual-mode super Q resonator is utilized to implement the filter and multiplexer designs. A 20-GHz, two-channel ($Q > 25,000$) vertical multiplexer with a 32-MHz channel bandwidth is fabricated and tested.

Three-State Diplexers

A new concept and approach for the integration of a three-state cavity diplexer is presented in [55]. The functions of a three-state diplexer can be summarized by the following:

- *State 1*: The excitation of port 1 corresponds to the generation of channels f_1 and f_2 .
- *State 2*: The excitation of port 2 corresponds to the generation of channels f_1 and f_3 .
- *State 3*: The excitation of port 3 corresponds to the generation of channels f_2 and f_3 .

Figure 14(a) displays the geometrical configuration of a three-state diplexer with a third-order response that consists of four identical TMRs. For all three states, the excited modes propagate through the TMR 2 cavity into the corresponding output ports. Three fundamental modes can be simultaneously propagated through three of four TMRs to form a miniaturized third-order, three-state diplexer structure. Figure 14(b) shows the separated simulated three-state S -parameters of the three diplexers in the three-state diplexer. All three passbands are designed with absolute bandwidths of 20 MHz, and isolation among the three channels can be implemented below 27 dB.

To achieve higher isolation among the channels of the three-state diplexer presented in [55], a geometrical configuration with a third-order response and consisting of six TMR cavities is proposed. Unlike the TMR 2 in Figure 14(b), which is a shared TMR for three fundamental modes, in the proposed structure, each of the three modes has its own path to be propagated. Compared with the former case that uses four TMRs, the latter has better isolation among all the channels but increases the number of resonators and the circuit volume.

Crossover

It is crucial to prevent interaction among multiple channel integrations in an N -to- N system. Modal orthogonality among multiple modes can address this issue. In [56], two types of three-way crossovers are presented for different applications. Depicted in Figure 15(a), a geometrical configuration of a wideband crossover with a fifth-order response is presented. It is noteworthy that two slots between ports and cavities and one slot between cavity and cavity are considered as three resonant windows. Hence, along with two-cavity resonators, the fifth-order filtering response can be achieved with five resonators. The S -parameter curves of the three-way wideband crossover are demonstrated in Figure 15(b). Three fundamental modes resonate at the same frequencies, and the bandwidth is enhanced to 24%

from 2.66 to 3.38 GHz. A perfect isolation performance with more than 50 dB is reached.

A narrowband three-way crossover is also presented in [56]. Using a similar structure but different physical dimensions, this kind of crossover possesses a fractional bandwidth of 1.4% at a 2.91-GHz central frequency, and isolation within the three-way crossover can reach 60 dB. Furthermore, this wideband crossover unit can be extended into a 2×2 three-way crossover array. The authors of [57]–[59] present two-way crossover components. In [57] and [58], a dual-channel DR crossover is implemented using two pairs of HEH_{11} and HEE_{11} harmonic modes. The proposed crossover resonates at 3.525 GHz, with an absolute bandwidth of 19 MHz (0.54%) and an insertion loss of 0.32 dB. Furthermore, the integration with a Doherty power amplifier for 5G massive multiple-input, multiple-output system applications is also designed.

Conclusions

This article presented an overview of a series of waveguide components based on MMRs. Due to the frequency resonances and inherent characteristics of multiple

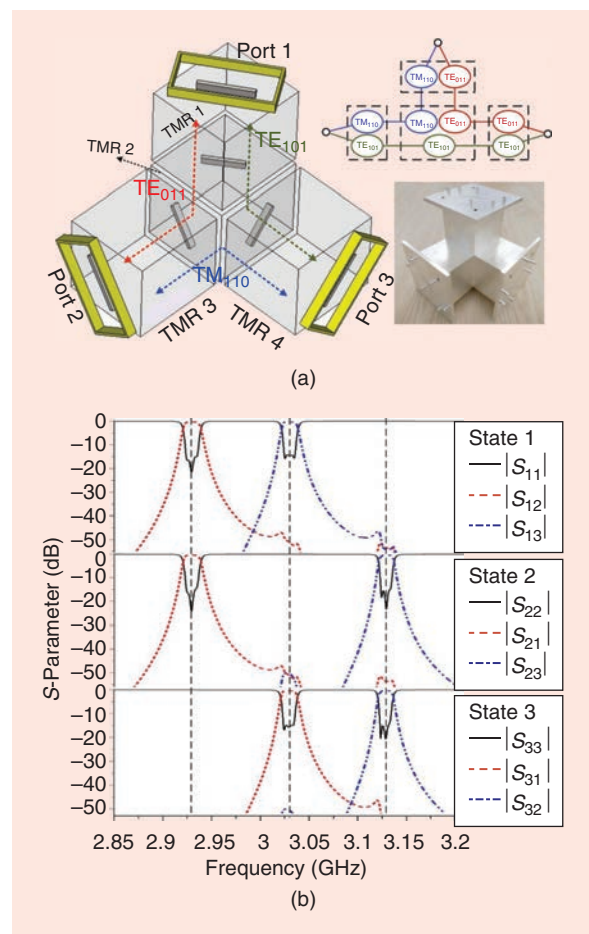


Figure 14. A three-state diplexer based on TMRs with (a) a geometrical configuration that has a third-order response and (b) the separated S -parameter responses [55].

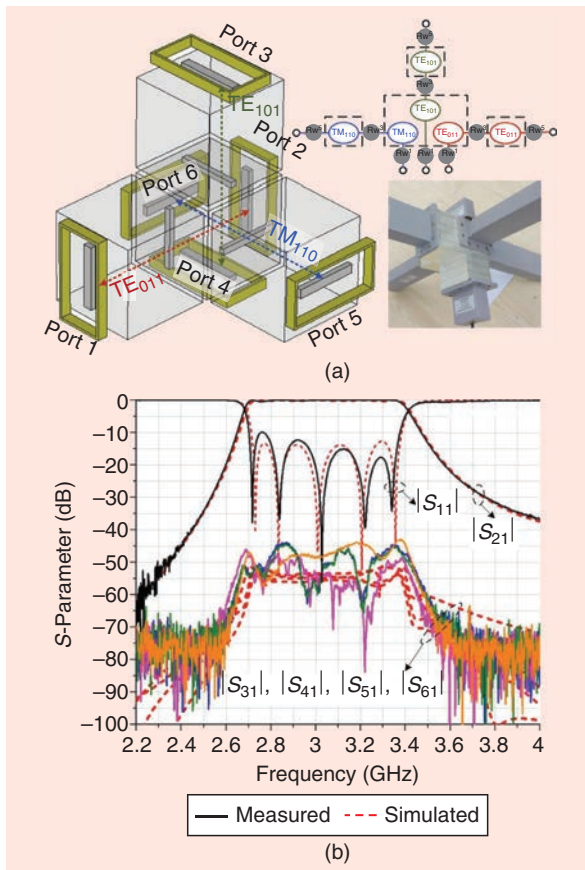


Figure 15. (a) A three-way crossover based on TMRs with a geometrical configuration that has a fifth-order response. (b) A comparison of the simulated and measured results [56].

modes in a single cavity, several novel circuits are presented, with the advantage of a miniaturized circuit volume and low in-band insertion losses. Good matching between the simulated and measured results verifies the accuracy of the proposed design methodology.

Acknowledgments

This work was supported, in part, by the Shenzhen Science and Technology Program, under grant JCYJ20180305124543176; the Natural Science Foundation of Guangdong Province, under grant 2018A030313481; the Shenzhen University Research Startup Project of New Staff, under grant 20188082; and the National Natural Science Foundation of China, under grant 81771955.

References

- [1] S. Sun and L. Zhu, "Multiple-resonator-based bandpass filters," *IEEE Microw. Mag.*, vol. 10, no. 2, pp. 88–98, Apr. 2009. doi: 10.1109/MMM.2008.931673.
- [2] X. Chen and K. Wu, "Substrate integrated waveguide filters: design techniques and structure innovations," *IEEE Microw. Mag.*, vol. 15, no. 6, pp. 121–133, Sept./Oct. 2014. doi: 10.1109/MMM.2014.2332886.
- [3] R. R. Mansour, "Filter technologies for wireless base stations," *IEEE Microw. Mag.*, vol. 5, no. 1, pp. 68–74, Mar. 2004. doi: 10.1109/MMW.2004.1284945.

- [4] M. Yu, "Power-handling capability for RF filters," *IEEE Microw. Mag.*, vol. 8, no. 5, pp. 88–97, Oct. 2007. doi: 10.1109/MMM.2007.904712.
- [5] R. J. Cameron, C. M. Kudsia, and R. R. Mansour, *Microwave Filters for Communication Systems-Fundamentals, Design and Applications*. Hoboken, NJ: Wiley, 2018.
- [6] S. Bastioli, "Nonresonating mode waveguide filters," *IEEE Microw. Mag.*, vol. 12, no. 6, pp. 77–86, Oct. 2011. doi: 10.1109/MMM.2011.942009.
- [7] C. Tomassoni, S. Bastioli, and R. Sorrentino, "Generalized TM dual-mode cavity filters," *IEEE Trans. Microw. Theory Techn.*, vol. 59, no. 12, pp. 3338–3346, Dec. 2011. doi: 10.1109/TMTT.2011.2172622.
- [8] S. Bastioli, C. Tomassoni, and R. Sorrentino, "A new class of waveguide dual-mode filters using TM and nonresonating modes," *IEEE Trans. Microw. Theory Techn.*, vol. 58, no. 12, pp. 3909–3917, Dec. 2010. doi: 10.1109/TMTT.2010.2086068.
- [9] H. Hu and K. Wu, "A TM_{11} dual-mode dielectric resonator filter with planar coupling configuration," *IEEE Trans. Microw. Theory Techn.*, vol. 61, no. 1, pp. 131–138, Jan. 2013. doi: 10.1109/TMTT.2012.2226741.
- [10] K. Wu, "An optimal circular-waveguide dual-mode filter without tuning screws," *IEEE Trans. Microw. Theory Techn.*, vol. 47, no. 3, pp. 271–276, Mar. 1999. doi: 10.1109/22.750222.
- [11] S. Amari, "Application of representation theory to dual-mode microwave bandpass filters," *IEEE Trans. Microw. Theory Techn.*, vol. 57, no. 2, pp. 430–441, Feb. 2009. doi: 10.1109/TMTT.2008.2011194.
- [12] S. Amari and U. Rosenberg, "New in-line dual- and triple-mode cavity filters with nonresonating nodes," *IEEE Trans. Microw. Theory Techn.*, vol. 53, no. 4, pp. 1272–1279, Apr. 2005. doi: 10.1109/TMTT.2005.845777.
- [13] Z. C. Guo et al., "Triple-mode cavity bandpass filter on doublet with controllable transmission zeros," *IEEE Access*, vol. 5, no. 3, pp. 6969–6977, 2017. doi: 10.1109/ACCESS.2017.2696120.
- [14] S. W. Wong, Z. C. Guo, J. Y. Lin, L. Zhu, and Q. Zhang, "Triple-mode and triple-band cavity bandpass filter on triplet topology with controllable transmission zeros," *IEEE Access*, vol. 6, pp. 29,452–29,459, May 2018. doi: 10.1109/ACCESS.2018.2837138.
- [15] S. W. Wong, S. F. Feng, Z. C. Zhang, B. L. Zheng, L. Zhu, and Q. X. Chu, "A compact triple-mode dielectric resonator in cylindrical cavity filter," *Microw. Opt. Techn.*, vol. 58, no. 7, pp. 1645–1647, July 2016. doi: 10.1002/mop.29878.
- [16] J. Y. Lin, M. Li, S. W. Wong, Y. Yang, and X. Zhu, "A cavity triple-mode filter with excitation of L-shape model," in *Proc. 2018 Aus. Microw. Symp. (AMS)*, Brisbane, QLD, pp. 17–18. doi: 10.1109/AUSMS.2018.8346960.
- [17] Z. Guo, S. W. Wong, J. Lin, L. Zhu, and Q. X. Chu, "Triple-mode cavity bandpass filter under excitation via U-shaped slots," *Electron. Lett.*, vol. 53, no. 24, pp. 1580–1582, 2017. doi: 10.1049/el.2017.3037.
- [18] D. R. Hendry and A. M. Abbosh, "Analysis of compact triple-mode ceramic cavity filters using parallel-coupled resonators approach," *IEEE Trans. Microw. Theory Techn.*, vol. 64, no. 8, pp. 2529–2537, Aug. 2016. doi: 10.1109/TMTT.2016.2577579.
- [19] D. R. Hendry and A. M. Abbosh, "Triple-mode ceramic cavity filters with wide spurious-free performance," *IEEE Trans. Microw. Theory Techn.*, vol. 65, no. 10, pp. 3780–3788, Oct. 2017. doi: 10.1109/TMTT.2017.2686859.
- [20] C. Kelleci and A. Atalar, "An analytical approach to the design of multiple mode rectangular cavity waveguide filters," *IEEE Trans. Microw. Theory Techn.*, vol. 65, no. 8, pp. 2857–2865, Aug. 2017. doi: 10.1109/TMTT.2017.2670000.
- [21] G. Basavarajappa and R. R. Mansour, "A high-Q quadruple-mode rectangular waveguide resonator," *IEEE Microw. Wireless Compon. Lett.*, vol. 29, no. 5, pp. 324–326, May 2019. doi: 10.1109/LMWC.2019.2906055.
- [22] X. Wang, G. Jang, B. Lee, and N. Park, "Compact quad-mode bandpass filter using modified coaxial cavity resonator with improved Q-factor," *IEEE Trans. Microw. Theory Techn.*, vol. 63, no. 3, pp. 965–975, Mar. 2015. doi: 10.1109/TMTT.2015.2389231.
- [23] M. Memarian and R. R. Mansour, "Quad-mode and dual-mode dielectric resonator filters," *IEEE Trans. Microw. Theory Techn.*, vol. 57, no. 12, pp. 3418–3426, Dec. 2009. doi: 10.1109/TMTT.2009.2034310.
- [24] L. Qian and Q. Chu, "A novel quadruple-mode cavity resonator filter with wide spurious-free window," in *Proc. 2018 IEEE MTT-S*

- Int. Wireless Symp. (IWS)*, Chengdu, pp. 1–3. doi: 10.1109/IEEE-IWS.2018.8400925.
- [25] S. W. Wong, S. F. Feng, L. Zhu, and Q. Chu, “Triple- and quadruple-mode wideband bandpass filter using simple perturbation in single metal cavity,” *IEEE Trans. Theory Techn.*, vol. 63, no. 10, pp. 3416–3424, Oct. 2015. doi: 10.1109/TMTT.2015.2460234.
- [26] S. W. Wong, S. F. Feng, F. Deng, L. Zhu, and Q. Chu, “A quintuple-mode wideband bandpass filter on single metallic cavity with perturbation cylinders,” *IEEE Microw. Wireless Compon. Lett.*, vol. 26, no. 12, pp. 975–977, Dec. 2016. doi: 10.1109/LMWC.2016.2623254.
- [27] S. F. Feng, S. W. Wong, L. Zhu, and Q. X. Chu, “A triple-mode wideband bandpass filter using single rectangular waveguide cavity,” *IEEE Microw. Wireless Compon. Lett.*, vol. 27, no. 2, pp. 117–119, Feb. 2017. doi: 10.1109/LMWC.2016.2647003.
- [28] B. L. Zheng, S. W. Wong, S. F. Feng, L. Zhu, and Y. Yang, “Multi-mode bandpass cavity filters and duplexer with slot mixed-coupling structure,” *IEEE Access*, vol. 6, pp. 16,353–16,362, Apr. 2018. doi: 10.1109/ACCESS.2017.2766293.
- [29] S. Amari and M. Bekheit, “A new class of dual-mode dual-band waveguide filters,” *IEEE Trans. Microwave Theory Techn.*, vol. 56, no. 8, pp. 1938–1944, Aug. 2008. doi: 10.1109/TMTT.2008.927411.
- [30] U. Naeem, S. Bila, M. Thevenot, T. Monediere, and S. Verdeyme, “A Dual-band bandpass filter with widely separated passbands,” *IEEE Trans. Microwave Theory Techn.*, vol. 62, no. 3, pp. 450–456, Mar. 2014. doi: 10.1109/TMTT.2014.2304361.
- [31] U. Naeem, A. Perigaud, and S. Bila, “Dual-mode dual-band bandpass cavity filters with widely separated passbands,” *IEEE Trans. Microwave Theory Techn.*, vol. 65, no. 8, pp. 2681–2686, Aug. 2017. doi: 10.1109/TMTT.2017.2723880.
- [32] L. Zhu, R. R. Mansour, and M. Yu, “Compact waveguide dual-band filters and duplexers,” *IEEE Trans. Microwave Theory Techn.*, vol. 65, no. 5, pp. 1525–1533, May 2017. doi: 10.1109/TMTT.2016.2642957.
- [33] Z. C. Guo, S. W. Wong, and L. Zhu, “Triple-passband cavity filters with high selectivity under operation of triple modes,” *IEEE Trans. Compon., Packag. Manuf. Technol.*, vol. 9, no. 7, pp. 1337–1344, 2019. doi: 10.1109/TCPMT.2018.2869854.
- [34] L. Zhu, R. R. Mansour, and M. Yu, “Compact triple-band bandpass filters using rectangular waveguide resonators,” in *Proc. 2016 IEEE MTT-S Int. Microw. Symp. (IMS)*, San Francisco, CA, 2016, pp. 1–3. doi: 10.1109/MWSYM.2016.7540059.
- [35] L. Zhu, R. R. Mansour, and M. Yu, “Triple-band cavity bandpass filters,” *IEEE Trans. Microwave Theory Techn.*, vol. 66, no. 9, pp. 4057–4069, Sept. 2018. doi: 10.1109/TMTT.2018.2846725.
- [36] J.-X. Chen, Y. Zhan, W. Qin, Z.-H. Bao, and Q. Xue, “Novel narrow-band balanced bandpass filter using rectangular dielectric resonator,” *IEEE Microw. Wireless Compon. Lett.*, vol. 25, no. 5, pp. 289–291, May 2015. doi: 10.1109/LMWC.2015.2409805.
- [37] J.-X. Chen, Y. Zhan, W. Qin, Z.-H. Bao, and Q. Xue, “Analysis and design of balanced dielectric resonator bandpass filter,” *IEEE Trans. Microwave Theory Techn.*, vol. 64, no. 5, pp. 1476–1483, May 2016. doi: 10.1109/TMTT.2016.2546260.
- [38] J.-X. Chen, Y. Zhan, W. Qin, and Z.-H. Bao, “Design of high-performance filtering balun based on TE_{01δ}-mode dielectric resonator,” *IEEE Trans. Ind. Electron.*, vol. 64, no. 1, pp. 451–458, Jan. 2017. doi: 10.1109/TIE.2016.2608788.
- [39] J.-X. Chen, J. Li, Y. Zhan, W. Qin, J. Shi, and Z.-H. Bao, “Design of balanced and balun filters using dual-mode cross-shaped dielectric resonators,” *IEEE Trans. Microwave Theory Techn.*, vol. 65, no. 4, pp. 1226–1234, Apr. 2017. doi: 10.1109/TMTT.2016.2635653.
- [40] S.-W. Wong et al., “Cavity balanced and unbalanced diplexer based on triple-mode resonator,” *IEEE Trans. Ind. Electron.*, vol. 67, no. 6, pp. 4969–4979, 2020. doi: 10.1109/TIE.2019.2928253.
- [41] J. M. Rebolgar, J. Esteban, and J. E. Page, “Fullwave analysis of three and four-port rectangular waveguide junctions,” *IEEE Trans. Microwave Theory Techn.*, vol. 42, no. 2, pp. 256–263, Feb. 1994. doi: 10.1109/22.275256.
- [42] L. Guo et al., “A waveguide magic-T with coplanar arms for high-power solid-state power combining,” *IEEE Trans. Microwave Theory Techn.*, vol. 65, no. 8, pp. 2942–2952, Aug. 2017. doi: 10.1109/TMTT.2017.2661741.
- [43] J. Y. Lin et al., “Cavity filtering magic-T and its integrations into balanced-to-unbalanced power divider and duplexing power divider,” *IEEE Trans. Microwave Theory Techn.*, vol. 67, no. 12, pp. 4995–5004, Dec. 2019. doi: 10.1109/TMTT.2019.2937772.
- [44] S. W. Wong, Z. C. Zhang, S. F. Feng, F. C. Chen, L. Zhu, and Q. X. Chu, “Triple-mode dielectric resonator diplexer for base-station applications,” *IEEE Trans. Microwave Theory Techn.*, vol. 63, no. 12, pp. 3947–3953, Dec. 2015. doi: 10.1109/TMTT.2015.2488658.
- [45] Z. C. Zhang et al., “Triple-mode dielectric-loaded cylindrical cavity diplexer using novel packaging technique for LTE base-station applications,” *IEEE Trans. Compon., Packag. Manuf. Technol.*, vol. 6, no. 3, pp. 383–389, Mar. 2016. doi: 10.1109/TCPMT.2016.2516820.
- [46] D. R. Hendry and A. M. Abbosh, “Compact high-isolation base-station diplexer using triple-mode ceramic cavities,” *IEEE Trans. Ind. Electron.*, vol. 65, no. 10, pp. 8092–8100, Oct. 2018. doi: 10.1109/TIE.2018.2803718.
- [47] J. Y. Lin, S. W. Wong, and L. Zhu, “High-isolation diplexer on triple-mode cavity filters,” in *Proc. 2017 IEEE MTT-S Int. Microw. Symp. (IMS)*, Honolulu, HI, pp. 1196–1199. doi: 10.1109/MWSYM.2017.8058817.
- [48] C. Carceller, P. Soto, V. Boria, M. Guglielmi, and J. Gil, “Design of compact wideband manifold-coupled multiplexers,” *IEEE Trans. Microwave Theory Techn.*, vol. 63, no. 10, pp. 3398–3407, Oct. 2015. doi: 10.1109/TMTT.2015.2460738.
- [49] X. Shang, Y. Wang, W. Xia, and M. J. Lancaster, “Novel multiplexer topologies based on all-resonator structures,” *IEEE Trans. Microwave Theory Techn.*, vol. 61, no. 11, pp. 3838–3845, Nov. 2013. doi: 10.1109/TMTT.2013.2284496.
- [50] G. Macchiarella and S. Tamiazzo, “Synthesis of star-junction multiplexers,” *IEEE Trans. Microwave Theory Techn.*, vol. 58, no. 12, pp. 3732–3741, Dec. 2010. doi: 10.1109/TMTT.2010.2086570.
- [51] J. Y. Lin, S. W. Wong, L. Zhu, and Q. X. Chu, “Design of miniaturized triplexers via sharing a single triple-mode cavity resonator,” *IEEE Trans. Microwave Theory Techn.*, vol. 65, no. 10, pp. 3877–3884, Oct. 2017. doi: 10.1109/TMTT.2017.2687424.
- [52] H. Hu and K. Wu, “A deterministic EM design technique for general waveguide dual-mode bandpass filters,” *IEEE Trans. Microwave Theory Techn.*, vol. 61, no. 2, pp. 800–807, Feb. 2013. doi: 10.1109/TMTT.2012.2231874.
- [53] H. Hu, K. Wu, and R. J. Cameron, “Stepped circular waveguide dual-mode filters for broadband contiguous multiplexers,” *IEEE Trans. Microwave Theory Techn.*, vol. 61, no. 1, pp. 139–145, Jan. 2013. doi: 10.1109/TMTT.2012.2227787.
- [54] B. Yassini and M. Yu, “Ka-band dual-mode super Q filters and multiplexers,” *IEEE Trans. Microwave Theory Techn.*, vol. 63, no. 10, pp. 3391–3397, Oct. 2015. doi: 10.1109/TMTT.2015.2462822.
- [55] J. Y. Lin, S. W. Wong, Y. M. Wu, L. Zhu, Y. Yang, and Y. He, “A new concept and approach for integration of three-state cavity diplexer based on TMRs,” *IEEE Trans. Microwave Theory Techn.*, vol. 66, no. 12, pp. 5272–5279, Dec. 2018. doi: 10.1109/TMTT.2018.2866858.
- [56] J. Y. Lin, S. W. Wong, Y. M. Wu, Y. Yang, L. Zhu, and Y. He, “Three-way multiple-mode cavity filtering crossover for narrowband and broadband applications,” *IEEE Trans. Microwave Theory Techn.*, vol. 67, no. 3, pp. 896–905, Mar. 2019. doi: 10.1109/TMTT.2018.2886835.
- [57] J. Xu and X. Y. Zhang, “Dual-channel dielectric resonator filter and its application to doherty power amplifier for 5G massive MIMO system,” *IEEE Trans. Microwave Theory Techn.*, vol. 66, no. 7, pp. 3297–3305, July 2018. doi: 10.1109/TMTT.2018.2829197.
- [58] J. Xu, X. Y. Zhang and Q. Xue, “Dual-channel filter based on dielectric resonator for 5G massive MIMO system,” in *Proc. 2018 IEEE MTT-S Int. Wireless Symp. (IWS)*, Chengdu, pp. 1–3. doi: 10.1109/IEEE-IWS.2018.8400849.
- [59] J. Xu, H. Li, X. Y. Zhang, Y. Yang, Q. Xue, and E. Dutkiewicz, “Compact dual-channel balanced filter and balun filter based on quad-mode dielectric resonator,” *IEEE Trans. Microwave Theory Techn.*, vol. 67, no. 2, pp. 494–504, Feb. 2019. doi: 10.1109/TMTT.2018.2886836.



©SHUTTERSTOCK.COM/IRMA KALLAS

Tunable Balanced Power Dividers

Feng Lin, Wenjie Feng, and Xiangguan Tan

Signal crosstalk and common-mode noise are two issues for engineers when designing today's increasingly complicated microwave integrated circuits [1]. Compared with single-ended circuits, balanced circuits can provide high immunity to environmental noise and broadband common-mode rejection capability [2]. Over the past few years, various balanced passive circuits, such as filters [3], antennas [4], power dividers, and couplers [5]–[17], have been extensively studied. Power dividers and couplers are widely used in microwave integrated circuits, such as antenna feeding networks, balanced mixers, and amplifiers. Balanced couplers are used in double-

balanced mixers [18] and balanced frequency doublers [19] to achieve higher efficiency and lower loss.

With recent advances in the development of 4G and 5G communication techniques, wireless services are in ever-increasing demand, which makes the radio spectrum increasingly overcrowded. To increase the efficiency of spectrum usage, modern transceiver systems are required to be frequency or function reconfigurable, which can also reduce the circuit size and cost. Thus, various reconfigurable devices [20], such as frequency-reconfigurable filters [21]; power-dividing, ratio-reconfigurable power dividers/couplers [22]–[30]; and frequency-reconfigurable couplers [31], [32], have been developed.

Feng Lin (linfeng.scut@gmail.com) and Xiangguan Tan (tanxiangguan@bit.edu.cn) are with the School of Information and Electronics, Beijing Institute of Technology, Beijing, China. Wenjie Feng (fengwenjie1985@163.com) is with the School of Electronic and Information Engineering, South China University of Technology, Guangzhou, China, and the Department of Communication Engineering, Nanjing University of Science and Technology, Nanjing, China.

Digital Object Identifier 10.1109/MMM.2020.3035864

Date of current version: 11 January 2021

Power dividers and couplers with tunable power-dividing ratios have been used to design polarization-reconfigurable and pattern-reconfigurable antennas [24], [34], [35] and Butler matrixes with improved sidelobe levels [36]. Traditionally, the power-dividing ratios of reconfigurable power dividers and couplers are tuned by adapting the switched transmission line configuration [23]–[25] or by varying the characteristic impedances [26]. In [27]–[30], continuous coupling tuning was realized by changing the capacitances of the varactor diodes. And, recently, balanced power dividers and couplers with tunable power-dividing ratios were proposed in [37]–[39].

This article provides an overview of recently developed balanced power dividers and couplers with fixed and tunable functions. The published tunable balanced power dividers and couplers have been developed with tunable power-dividing ratios that offer an electrically tunable power-dividing output, which can be used for beam steering, adaptive null forming, and target detection in fully balanced RF front ends (as shown in Figure 1). This article further discusses the progress being made in the primary research directions of tunable power dividers and couplers, which might be extended in the future to balanced circuits and system applications.

Balanced Power Dividers and Couplers

Figure 2(a) reviews the first balanced power divider without baluns, which is realized by a six-port network [Figure 2(b)] consisting of seven transmission lines and four resistances [5]. Due to its symmetrical structure, the power divider can be analyzed by the even-odd-mode method.

Figure 2(c) and (d) demonstrates the image and the simulated and measured differential mode S-parameters of the fabricated power divider. The measured fractional bandwidth is about 20.8%. Following this, other compact balanced power dividers [7] and balanced couplers [10] have been developed. Additionally, the 3-dB balanced power divider in [5] has been extended to support arbitrary power division [6], [11]. Other innovative designs include 1-way to 2N-way balanced power dividers [8] and impedance-transforming balanced couplers [15], [16].

On the other hand, filtering functions are widely integrated into balanced power dividers and couplers [12]–[14] for size miniaturization. Filtering responses can be achieved by using a transmission line resonator [12], a dielectric resonator [13], and a patch resonator [14]. At the same time, a more general balanced power divider [17] has been developed, where the functions of filtering, impedance transforming, and arbitrary power division output are integrated on the standalone device. Figure 3(a) depicts the block diagram of this general balanced power divider, which can reduce the number of passive components (i.e., filters, baluns, and impedance transformers) in an RF system [17]. Figure 3(b) illustrates the circuit model of this general balanced power divider, including a core block and four open-circuited stubs. The core block is like a two-stage asymmetric Wilkinson power divider supporting a differential response with an arbitrary power ratio, perfect common-mode suppression, and mode-conversion rejection. Open-circuited stubs are added to improve the frequency selectivity. Figure 3(c) displays the simulated differential-mode

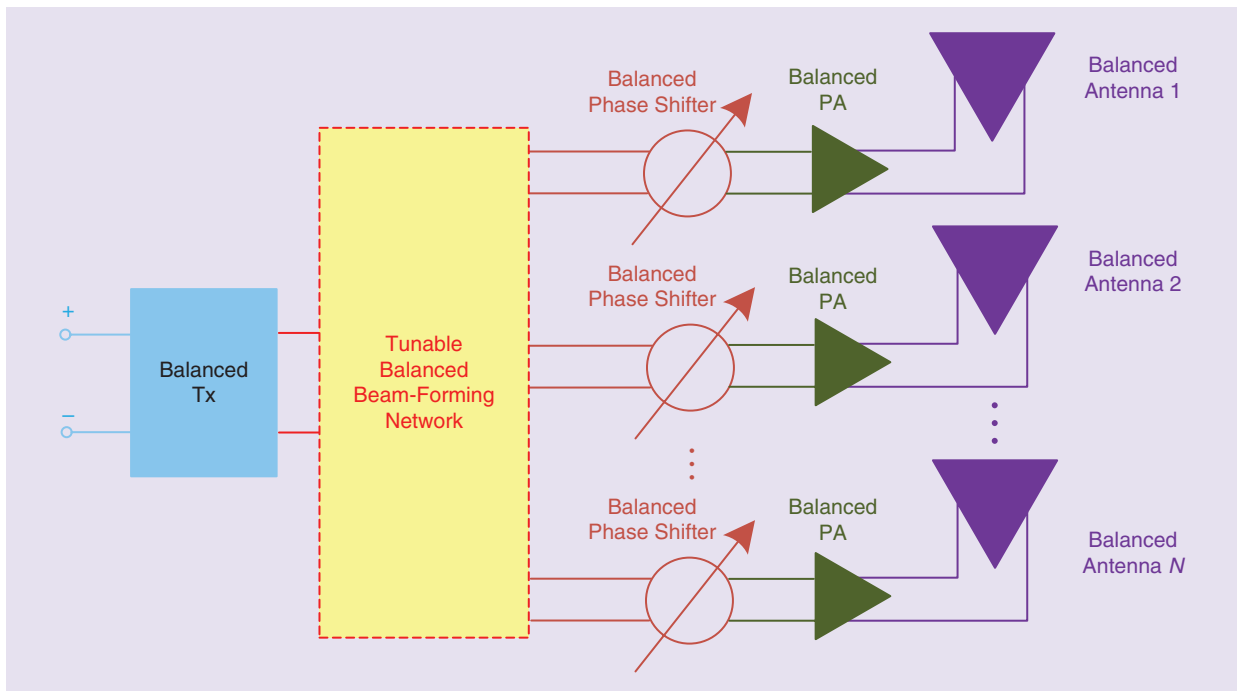


Figure 1. A fully balanced reconfigurable RF front end. Tx: transmitter; PA: power amplifier.

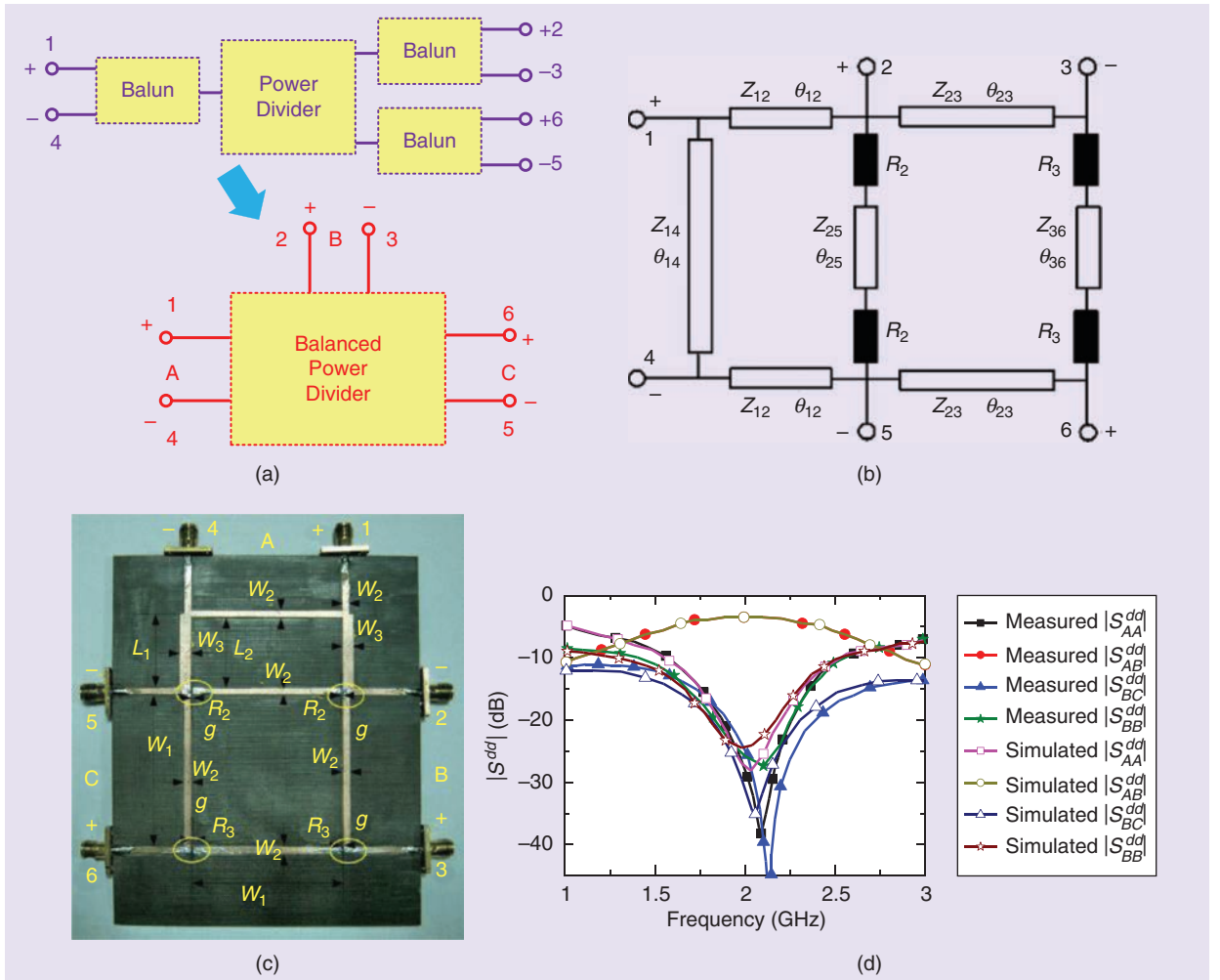


Figure 2. A balanced power divider [5]. The (a) power divider schematic, (b) circuit model, (c) image, and (d) simulated and measured differential-mode S -parameters.

parameters with different power-dividing ratios from 1 to 4. Two transmission zeros are located close to the pass-band to improve the frequency selectivity.

Tunable Balanced Power Dividers and Couplers

The first article on tunable balanced power dividers was published in 2017 [37]. Since then, both tunable balanced couplers and tunable balanced in-phase/out-of-phase power dividers have been reported.

Mixed-Mode Scattering Matrix of Six-Port Balanced Circuits

Figure 4(a) depicts a tunable balanced power divider, which is realized by a single-ended tunable power divider and three baluns. Figure 4(b) is a diagram of a balunless tunable balanced power divider. Due to the integrated design, the circuit size and loss caused by the baluns in the cascaded design [Figure 4(a)] will be reduced. The six-port balanced circuit in Figure 4(b) has three balanced ports (A, B, C, and D) consisting of the single-ended ports 1 and 4,

2 and 3, and 5 and 6, respectively. The mixed-mode scattering matrix (S_{mm}) [40] of a six-port balanced circuit can be defined as

$$S_{mm} = \begin{bmatrix} S_{AA}^{dd} & S_{AB}^{dd} & S_{AC}^{dd} & S_{AA}^{dc} & S_{AB}^{dc} & S_{AC}^{dc} \\ S_{BA}^{dd} & S_{BB}^{dd} & S_{BC}^{dd} & S_{BA}^{dc} & S_{BB}^{dc} & S_{BC}^{dc} \\ S_{CA}^{dd} & S_{CB}^{dd} & S_{CC}^{dd} & S_{CA}^{dc} & S_{CB}^{dc} & S_{CC}^{dc} \\ S_{AA}^{cd} & S_{AB}^{cd} & S_{AC}^{cd} & S_{AA}^{cc} & S_{AB}^{cc} & S_{AC}^{cc} \\ S_{BA}^{cd} & S_{BB}^{cd} & S_{BC}^{cd} & S_{BA}^{cc} & S_{BB}^{cc} & S_{BC}^{cc} \\ S_{CA}^{cd} & S_{CB}^{cd} & S_{CC}^{cd} & S_{CA}^{cc} & S_{CB}^{cc} & S_{CC}^{cc} \end{bmatrix} \quad (1)$$

and $S_{mm} = (S_{mm})^T$. The mixed-mode scattering matrix includes the differential-mode S -parameters of S^{dd} , the common-mode S -parameters of S^{cc} , and the cross-mode S -parameters of S^{dc} and S^{cd} . S^{dc} and S^{cd} represent the conversion of common-mode waves into differential-mode waves and the conversion of differential-mode waves into common-mode waves, respectively.

To meet the matching and isolation conditions of the tunable balanced power divider, the mixed-mode scattering matrix of S_{mm} should satisfy the following

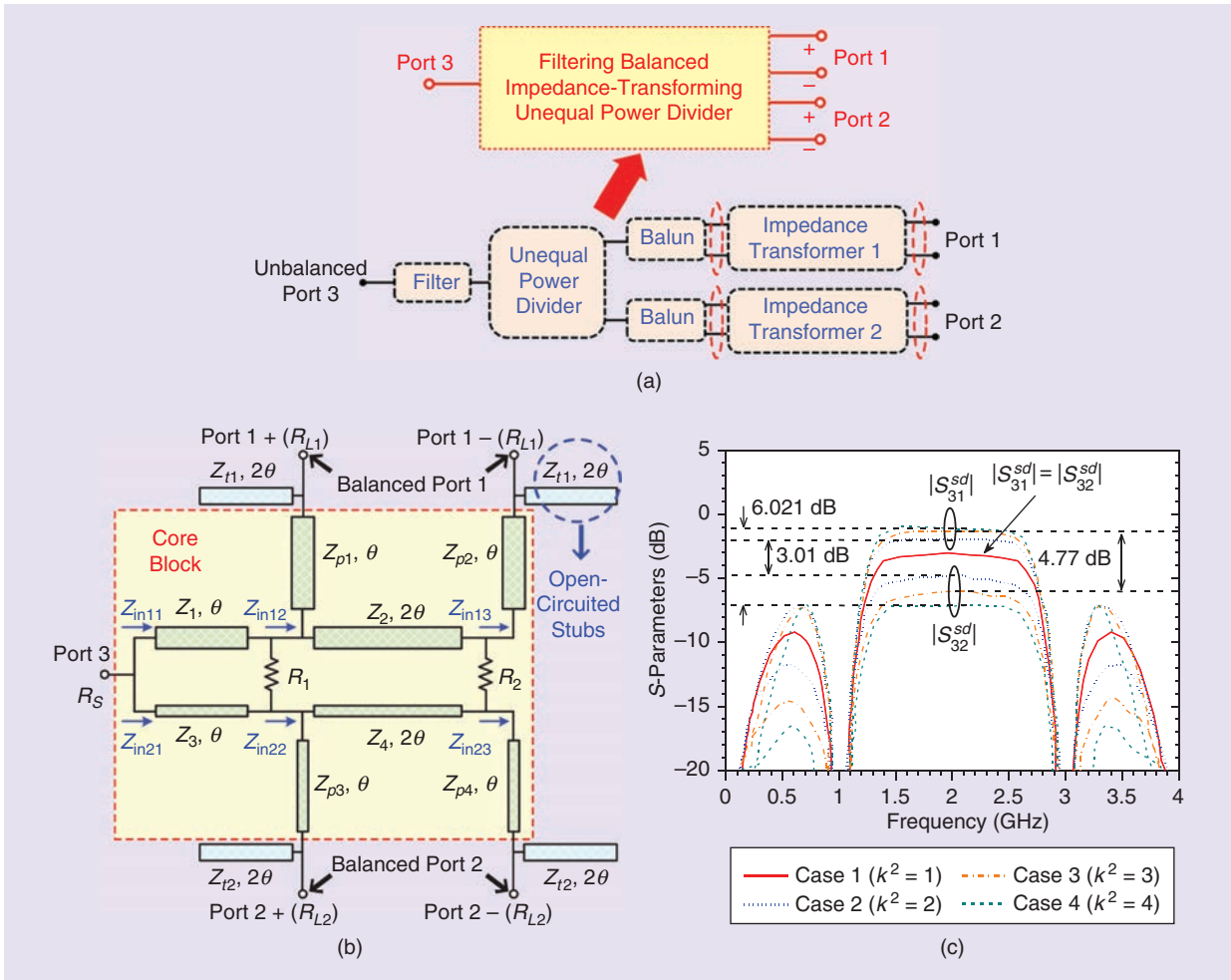


Figure 3. A filtering unbalanced-to-balanced impedance-transforming unequal power divider [17]. (a) The power divider schematic, (b) the circuit model, and (c) the simulated differential-mode S -parameters with different power-dividing ratios.

differential-mode operation, common-mode rejection, and cross-mode conversion suppression conditions across the entire tuning range:

$$S_{mm} = \begin{bmatrix} S^{dd} & S^{dc} \\ S^{cd} & S^{cc} \end{bmatrix} = \begin{bmatrix} 0 & ue^{j\varphi_1} & \sqrt{1-u^2}e^{j\varphi_2} & 0 & 0 & 0 \\ ue^{j\varphi_1} & 0 & 0 & 0 & 0 & 0 \\ \sqrt{1-u^2}e^{j\varphi_2} & 0 & 0 & 0 & 0 & 0 \\ 0 & 0 & 0 & e^{j\varphi_3} & 0 & 0 \\ 0 & 0 & 0 & 0 & e^{j\varphi_4} & 0 \\ 0 & 0 & 0 & 0 & 0 & e^{j\varphi_5} \end{bmatrix} \quad (2)$$

where φ_1 , φ_2 , φ_3 , φ_4 , and φ_5 are the phase constants of the S -parameters. Based on the definition of the mixed-mode scattering matrix, the S -parameters (standard matrix S_{std}) of the power divider can be derived in terms of the S_{mm} .

Tunable Balanced Power Dividers

Figure 5(a) displays the structure of a power-dividing, ratio-reconfigurable balanced power divider [37], which

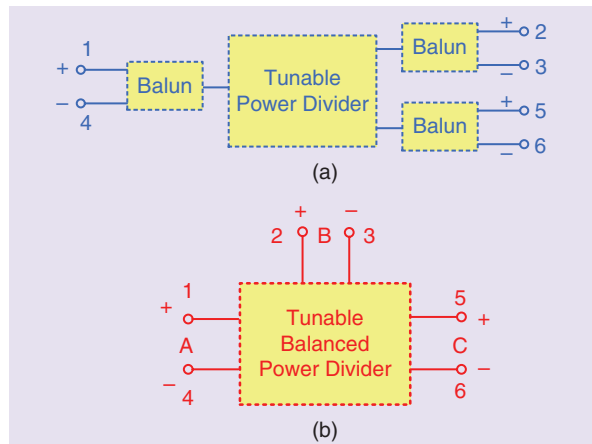


Figure 4. (a) A tunable single-ended power divider cascaded with three baluns. (b) A balunless tunable balanced power divider.

consists of five transmission lines, one isolation resistor, R_{iso} , and two varactor diodes, C_D . The transmission lines between the balanced two ports of port A (B and C) have the same characteristic impedance Z_2 and electrical

lengths of 180° at the center frequency. Figure 5(b) is a photograph of the fabricated tunable balanced power divider. The S -matrix of the balanced power divider in Figure 5 is derived, and then the design parameters of the balanced power divider are calculated by making the S -matrix meet the requirements of (2). The output differential-mode power-dividing ratio k^2 is tuned by the capacitance c of varactor diodes C_D .

Figure 6(a) and (b) represents the measured insertion losses at the center frequency and phase differences versus different bias voltages at the differential mode. The measured power-dividing ratio tuning range is from about -22.7 to 8.2 dB. The phase imbalances at the center frequency are smaller than 10° . Figure 6(c) depicts the measured mode-conversion suppression, which is better than

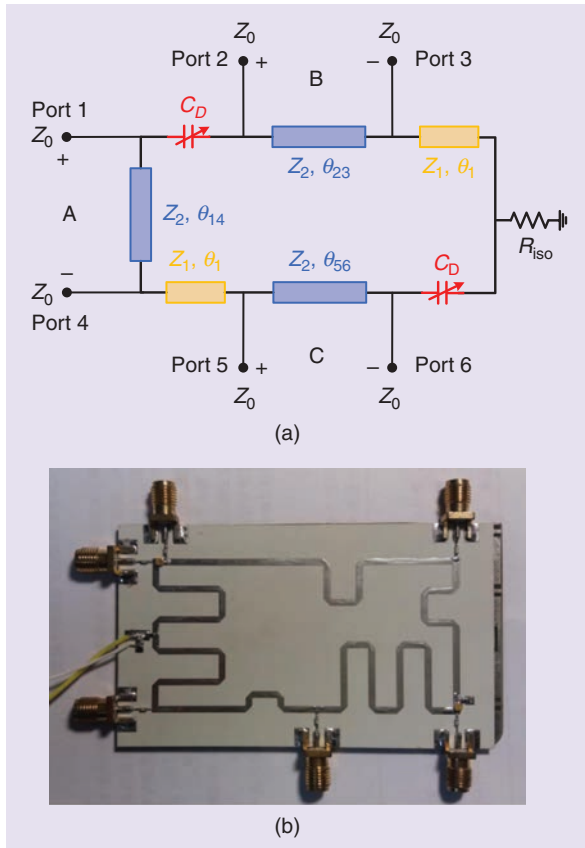


Figure 5. A reconfigurable balanced power divider [37]. (a) A power divider circuit and (b) the fabricated power divider.

20 dB. Figure 6(d) illustrates the measured common-mode return loss, which is better than 0.3 dB for all of the states.

Figure 7 details the schematic of a balanced in-phase/out-of-phase power divider with a tunable power-dividing ratio [38]. Two tunable networks, 1 and 2, with the same equivalent characteristic impedance of $Z_0/\sqrt{2}$ and electrical lengths of θ_1 and θ_1-90° , respectively, are used to tune the power-dividing ratio. The output differential-mode power-dividing ratio is determined by the electrical length θ_1 . When θ_1 is in the range of $0-90^\circ$, the power divider works in the in-phase mode. When θ_1 is from 90 to 180° , the power divider operates in the out-of-phase mode.

Mixed-Mode Scattering Matrix of Eight-Port Balanced Circuits

Figure 8(a) illustrates a tunable balanced coupler realized by a single-ended tunable coupler and four baluns. A balunless tunable balanced coupler reduces the circuit size and the loss caused by the baluns; a diagram of such a coupler is found in Figure 8(b). The eight-port balanced circuit in Figure 8(b) has four balanced ports (A, B, C, and D) consisting of the single-ended ports 1 and 2, 3 and 4, 5 and 6, and 7 and 8, respectively. The mixed-mode scattering matrix (S_{mm}) [40] of an eight-port balanced circuit can be defined as

$$S_{mm} = \begin{bmatrix} S^{dd} & S^{dc} \\ S^{cd} & S^{cc} \end{bmatrix}, \quad S^{ij} = \begin{bmatrix} S_{AA}^{ij} & S_{AB}^{ij} & S_{AC}^{ij} & S_{AD}^{ij} \\ S_{BA}^{ij} & S_{BB}^{ij} & S_{BC}^{ij} & S_{BD}^{ij} \\ S_{CA}^{ij} & S_{CB}^{ij} & S_{CC}^{ij} & S_{CD}^{ij} \\ S_{DA}^{ij} & S_{DB}^{ij} & S_{DC}^{ij} & S_{DD}^{ij} \end{bmatrix} \quad (3)$$

where ij is dd, dc, cd, or cc, and $S_{mm} = (S_{mm})^T$.

To meet the matching and isolation requirements for a tunable balanced coupler, S_{mm} should satisfy the mixed-mode conditions of (4) (see bottom of page) across the entire tuning range, where $\varphi_1, \varphi_2, \varphi_3, \varphi_4, \varphi_5,$ and φ_6 are the phase constants of the S -parameters.

Usually, a tunable balanced coupler is bisymmetric. By exciting two magnetic walls (H -walls), an electric wall (E -wall) and an H -wall, an H -wall and an E -wall, and two E -walls along the symmetry axes $A'A''$ and $B'B''$, respectively, four two-port reduced circuits of the tunable balanced coupler (Figure 9) can be obtained. The S -parameters of the reduced circuits are calculated first. Then the S -parameters (standard matrix S_{std}) of the coupler can

$$S_{mm} = \begin{bmatrix} S^{dd} & S^{dc} \\ S^{cd} & S^{cc} \end{bmatrix} = \begin{bmatrix} 0 & 0 & ue^{j\varphi_1} & \sqrt{1-u^2}e^{j\varphi_2} & 0 & 0 & 0 & 0 \\ 0 & 0 & \sqrt{1-u^2}e^{j\varphi_2} & ue^{j\varphi_1} & 0 & 0 & 0 & 0 \\ ue^{j\varphi_1} & \sqrt{1-u^2}e^{j\varphi_2} & 0 & 0 & 0 & 0 & 0 & 0 \\ \sqrt{1-u^2}e^{j\varphi_2} & ue^{j\varphi_1} & 0 & 0 & 0 & 0 & 0 & 0 \\ 0 & 0 & 0 & 0 & 0 & e^{j\varphi_3} & 0 & 0 \\ 0 & 0 & 0 & 0 & 0 & 0 & e^{j\varphi_4} & 0 \\ 0 & 0 & 0 & 0 & 0 & 0 & 0 & e^{j\varphi_5} \\ 0 & 0 & 0 & 0 & 0 & 0 & 0 & e^{j\varphi_6} \end{bmatrix} \quad (4)$$

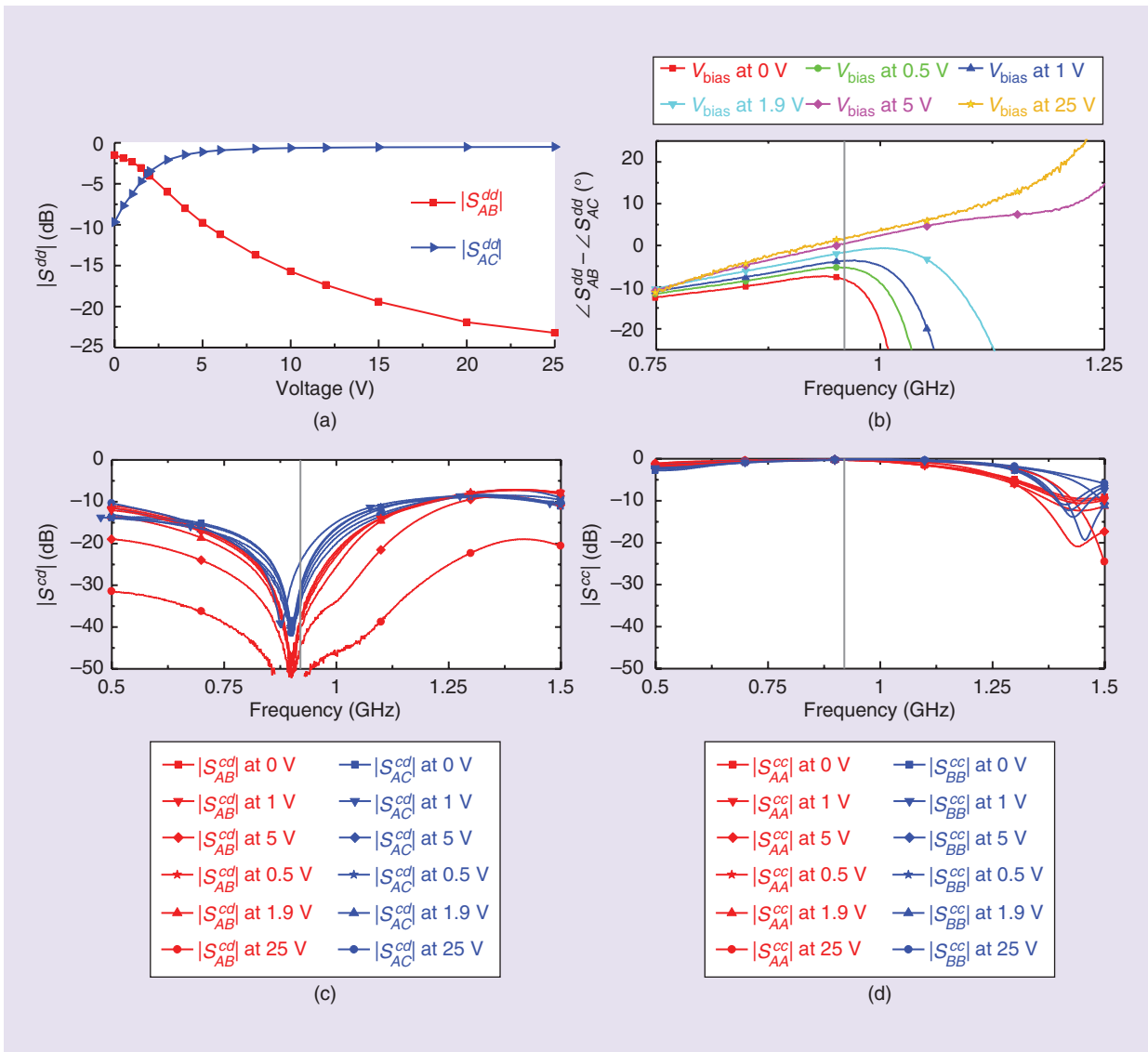


Figure 6. The measured mixed-mode S-parameters versus the bias voltage V_{bias} [37]. The (a) differential-mode insertion losses at f_0 , (b) differential-mode phase differences, (c) cross-mode conversion S-parameters, and (d) common-mode return loss.

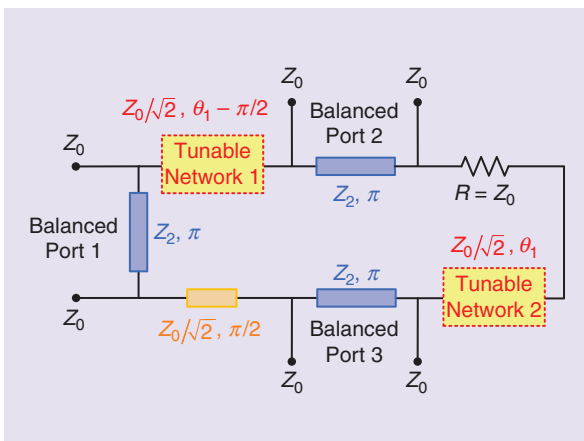


Figure 7. A schematic of a balanced in-phase/out-of-phase power divider with tunable power-dividing ratio [38].

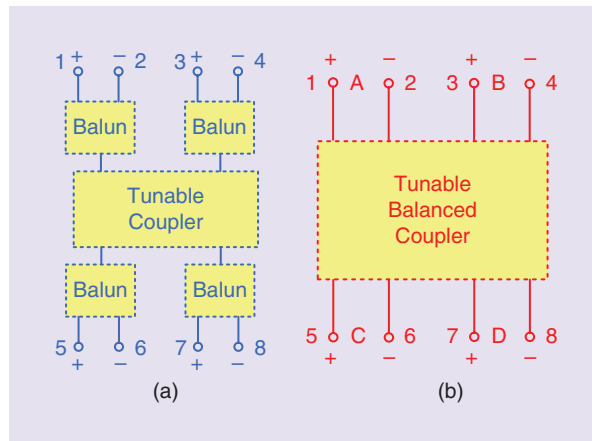


Figure 8. (a) A tunable single-ended coupler cascaded with four baluns. (b) A balunless tunable balanced coupler.

be expressed in terms of the S -parameters of the reduced circuits. Finally, the S_{mm} of the balanced eight-port circuit can be derived in terms of the S_{std} .

Tunable Balanced Couplers

Figure 10(a) depicts the structure of a coupling-ratio-reconfigurable balanced coupler [39], with three fixed capacitors C_0 and C_1 and two tunable capacitors C_d . The transmission lines between the two balanced ports of port A (B, C, and D) have the same characteristic impedance Z_2 and electrical lengths of 180° at the center frequency. Figure 10(b) is a photograph of the fabricated tunable balanced coupler. The S -matrix (S_{std}) of the balanced coupler in Figure 10 is derived first, and the design parameters of the balanced coupler are calculated by making the S_{mm} meet the requirements of (4). The output differential-mode power-dividing ratio K is tuned by the capacitance C_d .

Figure 11(a) illustrates the measured insertion losses at the center frequency and phase differences versus different bias voltages at the differential mode. The measured power-dividing ratio tuning range is from about -11.3 to 10.2 dB. The phase imbalances at the center frequency are smaller than 25° . Figure 11(b) indicates that the measured mode conversion suppression is better than 25 dB. Figure 11(c) demonstrates that the measured common-mode return loss and isolation are better than 0.2 dB and 45 dB, respectively, for all of the states.

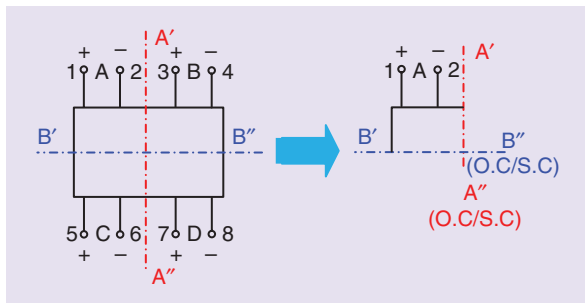


Figure 9. A simplified equivalent circuit of a tunable balanced coupler.

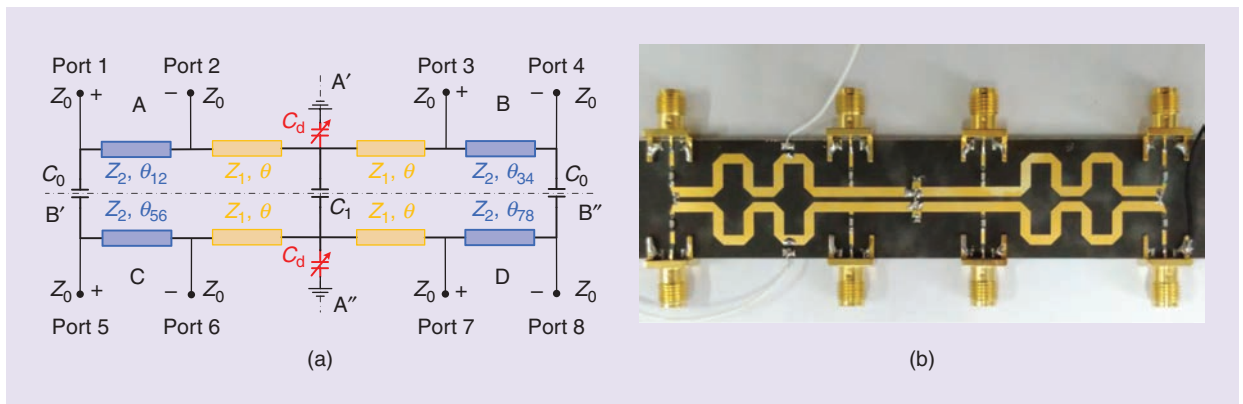


Figure 10. A reconfigurable balanced coupler [39]. (a) A coupler circuit and (b) the fabricated coupler.

Discussion of the Phase Imbalance Performance

Figures 6 and 11 depict the measured phase differences of balanced tunable power dividers and couplers, respectively. It can be observed that the phase imbalance becomes larger as the power-dividing ratio increases. Thus, the tuning range is limited by the phase imbalance performance. The phase imbalance is primarily caused by the resistive loss from the varactors and transmission lines. Considering the loss of varactors, the differential-mode power-dividing ratio of the power divider and coupler can be obtained and simplified as (5) and (6), respectively,

$$\frac{S_{AB}^{dd}}{S_{AC}^{dd}} = \frac{\omega C Z_0}{2(1 + j\omega C r_v)} \quad (5)$$

$$\frac{S_{AC}^{dd}}{S_{AD}^{dd}} = j \frac{C_d \omega Z_0 \cos^2 \theta - 2 \cos 2\theta}{1 + j C_d \omega r_v}, \quad (6)$$

where r_v represents the varactor resistance. Based on (5) and (6), the phase imbalance increases with increasing r_v , and also increases with the increasing capacitance of the varactors (c or C_d). For the state of 3-dB coupling, the measured additional insertion loss of a coupler is about 1.2 dB, and the phase imbalance is 9° [39]. Using high- Q varactors [e.g., microelectromechanical systems (MEMS) capacitors] can further improve the insertion loss and phase difference. In [39], an active capacitance circuit with negative impedance was used to improve the insertion loss and phase difference of the tunable balanced coupler.

Figure 12(a) illustrates the improved tunable balanced coupler with an active capacitance circuit [39]. The active capacitance circuit consists of a common-source field-effect transistor with an R - L - C series feedback structure, which can exhibit negative resistance and capacitance. The varactors C_d and the transistors are implemented by MA46H202 gallium arsenide diodes and ATF35143 transistors, respectively. Negative resistance is obtained at 2.0 GHz by choosing a C_d of 5 pF, an L_d of 3 nH, and an R_d of 2Ω in the feedback structure. The ATF35143 is biased by two 47-nH inductors (L_D , L_C). C_g and L_g are set to 100 pF and 6.6 nH, respectively. Figure 12(b) is a photograph

of the fabricated tunable balanced coupler with active capacitance circuits. Figure 13 presents the measured differential-mode insertion losses and phase differences results versus the power-dividing ratio at the center frequency of the tunable balanced coupler with and without active capacitance circuits. With active capacitance circuits, the insertion loss is improved by 1.2 dB for the 3-dB coupling state. The measured phase imbalances are improved from 25° to lower than 2° for all of the states.

Unbalanced Tunable Power Dividers and Couplers

This article focuses on the design of balanced power dividers and couplers with tunable power-dividing ratios. Unbalanced tunable power dividers and couplers are also a fruitful area of development [33], [41]–[49]. Recent research on unbalanced tunable power dividers and couplers has primarily centered on aspects such as frequency

reconfigurability [41], [42], simultaneous frequency and power-dividing ratio reconfigurability [43]–[45], phase reconfigurability [46], and frequency reconfigurability integrated with filtering functions [33], [48], [49]. Unbalanced tunable power dividers and couplers have approached these issues in the following ways:

- *Frequency reconfigurability:* Frequency tuning is usually realized by changing the capacitances of the varactors used in the couplers [32], [41], [42]. In [32], rat-race couplers with tunable frequency are achieved based on the port equivalent impedance method. Frequency-reconfigurable couplers would be suitable for multiband applications.
- *Simultaneous frequency and power-dividing ratio reconfigurability:* In [43] and [44], the power-dividing ratio and the operating frequency of monolithic microwave integrated circuit and CMOS couplers were tuned simultaneously by two kinds of tuning elements (i.e., varactors and tunable active inductors).

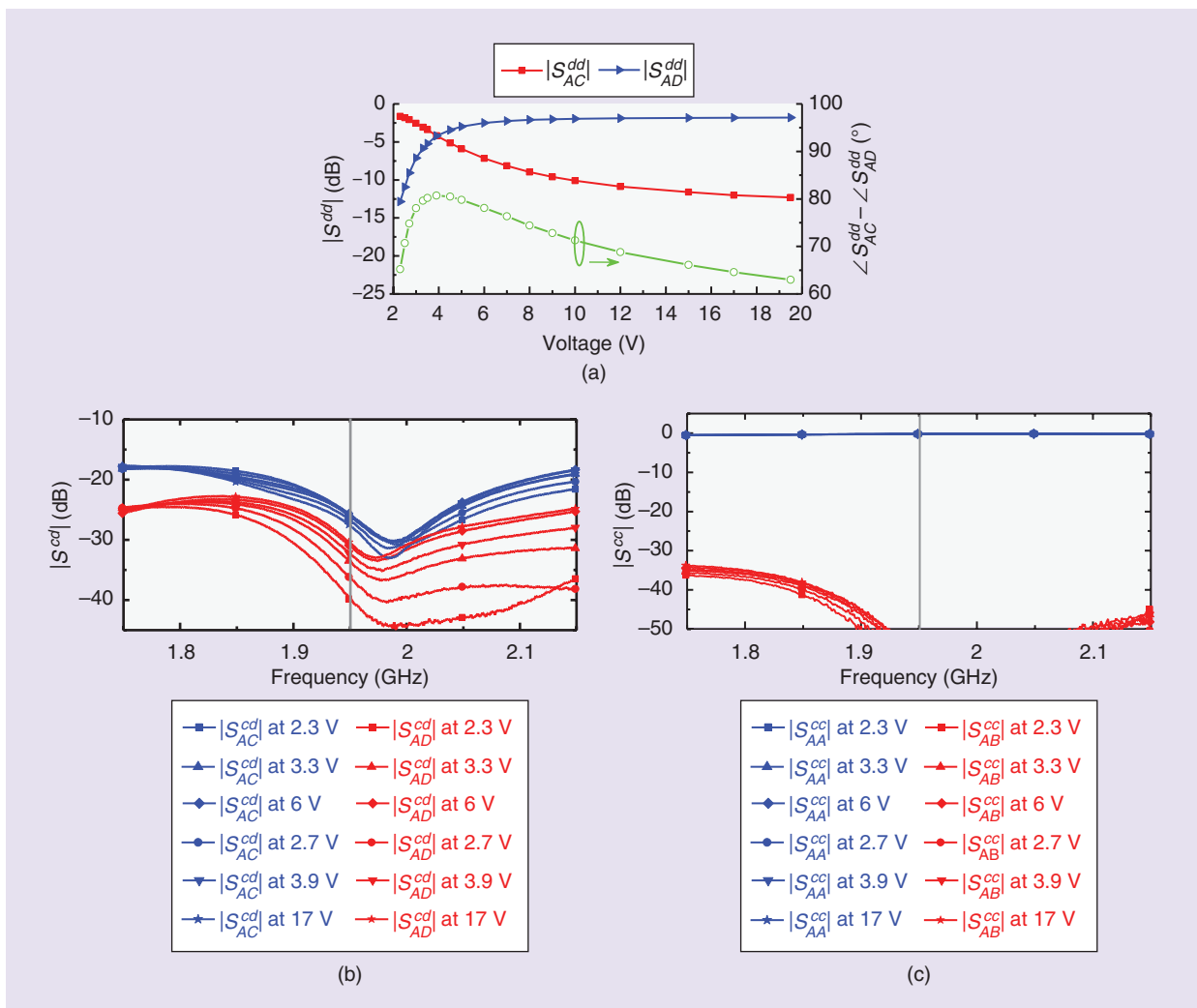


Figure 11. The measured mixed-mode S-parameters versus the bias voltage V_{bias} [39]. The (a) differential-mode insertion losses and phase differences, (b) cross-mode conversion S-parameters, and (c) common-mode return loss and isolation.

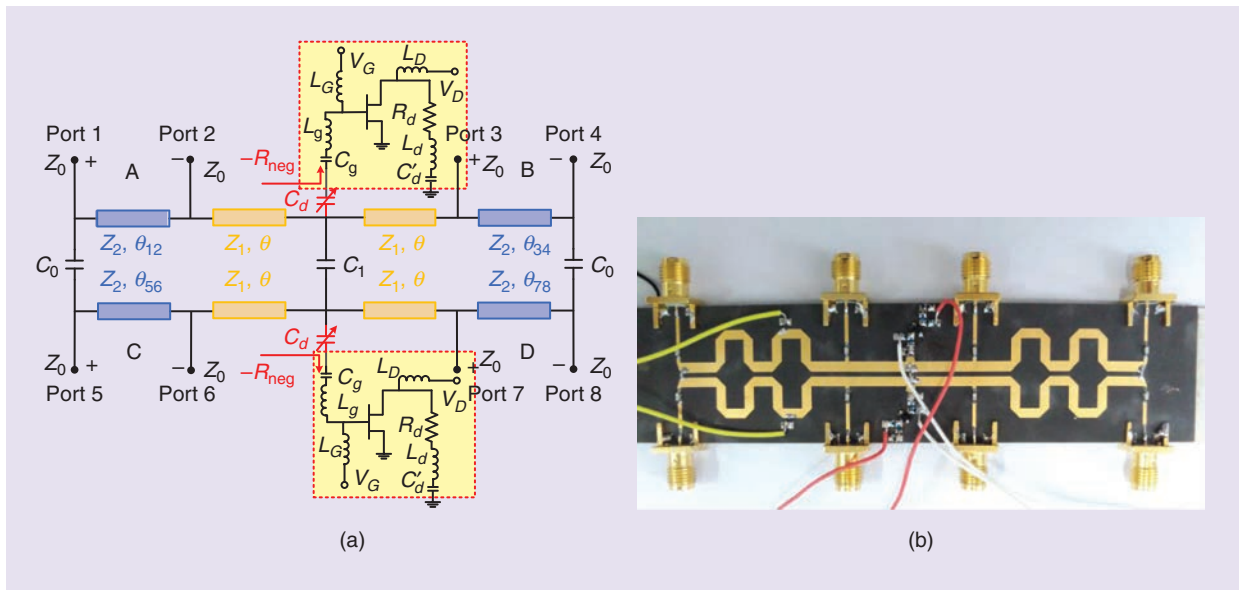


Figure 12. An improved tunable balanced coupler with active capacitance circuits [39]. (a) A coupler circuit and (b) the fabricated coupler.

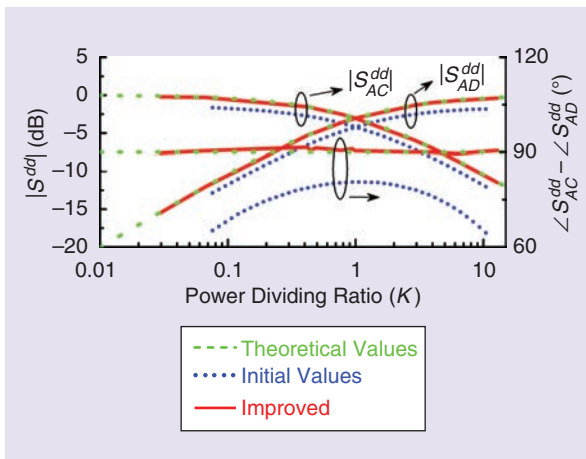


Figure 13. The measured differential-mode insertion losses and phase differences at the f_0 of the balanced coupler with and without active capacitance circuits [39].

One potential application of this kind of coupler is as a duplexer in a transceiver [43].

- **Phase reconfigurability:** In [46], the phase difference of the output ports of a coupler can be continuously tuned, which integrates the functions of the phase shifters and couplers.
- **Frequency reconfigurability integrated with filtering functions:** The integration of microwave components is critical for reducing the system size. Compared with the conventional cascaded design of filtering couplers, the codesigned dual-band filtering coupler [47] provides an alternative approach to reducing the size, loss, and cost of RF modules. In [48], a tunable filtering power divider is realized using tunable coupled resonators. In [31] and [49], a class of filtering couplers

with reconfigurable frequency is reported for the first time. The reconfigurable filtering couplers are constructed by substituting the quarter-wavelength ($\lambda/4$) transmission line in a conventional coupler with a reconfigurable filtering transmission line with a 90° or -90° phase shift. A reconfigurable filtering rat-race coupler and a quadrature coupler with constant fractional bandwidth and constant absolute bandwidth, respectively, are designed and demonstrated by measurement in [31] and [49]. To further improve the loss performance, a frequency-tunable quadrature coupler can be designed using substrate integrated waveguide cavities [33].

At present, research on tunable balanced power dividers and couplers has tended to focus on power-dividing-ratio reconfigurability. The aforementioned tunable functions will likely be further integrated into balanced and balanced-to-unbalanced devices in the future, which will expand their potential applications in balanced circuits and systems.

Conclusions and Future Development

This article presents an overview of recently developed tunable balanced power dividers and couplers. Comparisons with reported balanced power dividers and couplers with fixed power-dividing ratios are shown in Tables 1 and 2. The tunable balanced power dividers and couplers feature a wide tuning range of power division, moderate matching and isolation bandwidths, and compact circuit size.

The phase imbalance of balanced power dividers and couplers limits the tuning range of their power-dividing ratios. Thus, innovative circuit designs with improved phase imbalance are urgently needed. In addition, the

TABLE 1. A performance comparison of several reported balanced power dividers.

Balanced Power-Divider Architecture	Power-Dividing Ratio (Tuning Ratio)	Differential Mode				
		BW (RL > 15 dB)	IL (dB) at f_0	BW (Isolation > 20 dB)	Phase Imbalance at f_0	Size ($\lambda_g \times \lambda_g$)
[5], Planar	3 dB (fixed)	24%	0.2	25%	$< 1^\circ$	0.75×0.5
[6], Planar	10 dB (fixed)	18%	0.7	25%	$\sim 5^\circ$	0.75×0.5
[9], Planar	3 dB (fixed)	40%	1	4%	$< 1.5^\circ$	0.5×0.5
[37], Planar continuously tunable	-22.7–8.2 dB (0.01–3.61)	6.3%	0.7 (tuning ratio = 1)	15%	$< 10^\circ$	0.4×0.2

BW: bandwidth; RL: return loss; IL: insertion loss.

TABLE 2. A performance comparison of several reported balanced couplers.

Balanced Coupler Architecture	Power-Dividing Ratio (Tuning Ratio)	Differential Mode			
		BW (RL > 15 dB)	IL (dB) at f_0	Phase Imbalance at f_0	Size ($\lambda_g \times \lambda_g$)
[10], Planar balanced crossover	0 dB (fixed)	22% (RL > 22 dB)	0.85	N/A	0.95×0.95
[11], Planar balanced coupler	3 dB (fixed)	4.3%	0.45	$\sim 5^\circ$	0.52×0.5
[39], Planar tunable balanced coupler	-11.3–10.2 dB (0.07 ~ 11.2)	4.1–19.5%	1.2 (tuning ratio = 1)	$< 25^\circ$	0.88×0.21
[39], Planar improved tunable balanced coupler	-15.3–11.1 dB (0.03–12.9)	1.6–11.3%	0 (tuning ratio = 1)	$< 2^\circ$	0.88×0.25

bandwidths of balanced power dividers and couplers are narrow; hence, bandwidth extension is another design challenge. The balanced power dividers and couplers discussed in this article are primarily realized with single-layer microstrip structures. To further reduce the circuit size of balanced power dividers and couplers, MEMS and CMOS techniques can be utilized, which will benefit the integration with other balanced front-end components for practical high-density balanced communication systems. It is anticipated that more and more multifunctional tunable balanced devices with high performance will appear in the near future.

Acknowledgments

The authors are grateful for the support of the Key Area Research and Development Program of Guangdong Province under grant 2018B010115001, the National Natural Science Foundation of China (61601026, 61822110), the Open Project of the State Key Laboratory of Millimeter Waves under grant K202021, the Guangdong Important Fields Research Program (2018B010115001), and the Guangdong Innovative and Entrepreneurial Research Team Program (2017ZT07X032).

References

[1] W. J. Feng, W. Q. Che, and Q. Xue, "New balance—Applications for dual-mode ring resonators in planar balanced circuits," *IEEE Microw. Mag.*, vol. 20, no. 7, pp. 15–23, July 2019. doi: 10.1109/MMM.2019.2909519.

[2] W. J. Feng, W. Q. Che, and Q. Xue, "The proper balance: Overview of microstrip wideband balanced circuits with wideband common mode suppression," *IEEE Microw. Mag.*, vol. 16, no. 5, pp. 55–68, June 2015. doi: 10.1109/MMM.2015.2408275.

[3] W. J. Feng and W. Q. Che, "Novel wideband differential bandpass filter based on T-shaped structure," *IEEE Trans. Microw. Theory Techn.*, vol. 60, no. 6, pp. 1560–1568, June 2012. doi: 10.1109/TMTT.2012.2188538.

[4] Y.-P. Zhang, "Design and experiment on differentially driven microstrip antennas," *IEEE Trans. Antennas Propag.*, vol. 55, no. 10, pp. 2701–2708, Oct. 2007. doi: 10.1109/TAP.2007.905832.

[5] B. Xia, L.-S. Wu, and J. F. Mao, "A new balanced-to-balanced power divider/combiner," *IEEE Trans. Microw. Theory Techn.*, vol. 60, no. 9, pp. 287–295, Sept. 2012.

[6] B. Xia, L. S. Wu, S. W. Ren, and J. F. Mao, "A balanced to balanced power divider with arbitrary power division," *IEEE Trans. Microw. Theory Techn.*, vol. 61, no. 8, pp. 287–295, Aug. 2013.

[7] W. W. Zhang et al., "Novel planar compact coupled-line single-ended-to-balanced power divider," *IEEE Trans. Microw. Theory Techn.*, vol. 65, no. 8, pp. 2953–2963, Aug. 2017. doi: 10.1109/TMTT.2017.2685389.

[8] X. Gao, W. J. Feng, W. Q. Che, and Q. Xue, "Wideband balanced-to-unbalanced filtering power dividers based on coupled lines," *IEEE Trans. Microw. Theory Techn.*, vol. 65, no. 1, pp. 86–95, Jan. 2017. doi: 10.1109/TMTT.2016.2614668.

[9] S. Chen, W.-C. Lee, and T.-L. Wu, "A balanced-to-balanced power divider with common-mode noise absorption," in *Proc. IEEE/MTT-S Int. Microw. Symp.*, June 2016, pp. 1–4. doi: 10.1109/MWSYM.2016.7540282.

[10] Y.-H. Pang, E. D. Lin, and Y.-Y. Chen, "A planar balanced crossover," *IEEE Trans. Microw. Theory Techn.*, vol. 64, no. 6, pp. 1812–1821, June 2016. doi: 10.1109/TMTT.2016.2551703.

[11] W. J. Feng et al., "Balanced rat-race couplers with wide-band common-mode suppression," *IEEE Trans. Microw. Theory Techn.*, vol. 67, no. 12, pp. 4724–4732, Dec. 2019. doi: 10.1109/TMTT.2019.2946158.

[12] L.-S. Wu, Y.-X. Guo, and J.-F. Mao, "Balanced-to-balanced Gysel power divider with bandpass filtering response," *IEEE Trans. Microw.*

- Theory Techn.*, vol. 61, no. 12, pp. 4052–4062, Dec. 2013. doi: 10.1109/TMTT.2013.2287684.
- [13] W. Yu and J.-X. Chen, “Multiport in-phase/antiphase power dividing network with bandpass response based on dielectric resonator,” *IEEE Trans. Microw. Theory Techn.*, vol. 66, no. 11, pp. 4773–4782, Nov. 2018. doi: 10.1109/TMTT.2018.2860969.
- [14] Q. Liu, J. Wang, L. Zhu, G. Zhang, and W. Wu, “Design of a new balanced-to-balanced filtering power divider based on square patch resonator,” *IEEE Trans. Microw. Theory Techn.*, vol. 66, no. 12, pp. 5280–5289, Dec. 2018. doi: 10.1109/TMTT.2018.2871180.
- [15] L. Jiao, Y. Wu, and W. Zhang, “Design methodology for six-port equal/unequal quadrature and rat-race couplers with balanced and unbalanced ports terminated by arbitrary resistances,” *IEEE Trans. Microw. Theory Techn.*, vol. 66, no. 3, pp. 1249–1262, Mar. 2018. doi: 10.1109/TMTT.2017.2778108.
- [16] L. Li, J.-F. Mao, and L.-S. Wu, “A single-ended-to-balanced impedance-transforming branch-line coupler with arbitrary power division ratio,” *IEEE Trans. Microw. Theory Techn.*, vol. 67, no. 3, pp. 949–956, Mar. 2019. doi: 10.1109/TMTT.2019.2892433.
- [17] Y. Wu, Z. Zhuang, M. Kong, L. Jiao, Y. Liu, and A. A. Kishk, “Wide-band filtering unbalanced-to-balanced independent impedance-transforming power divider with arbitrary power ratio,” *IEEE Trans. Microw. Theory Techn.*, vol. 66, no. 10, pp. 4482–4496, Oct. 2018. doi: 10.1109/TMTT.2018.2856259.
- [18] H. J. Ng; M. Jahn, R. Feger, C. Wagner, and A. Stelzer, “An efficient SiGe double-balanced mixer with a differential rat-race coupler,” in *Proc. European Microw. Conf.*, 2013, pp. 1551–1554.
- [19] J. Wan, Z. Chen, Q. An, and X. Wang, “A truly balanced Q-band CMOS frequency doubler based on hybrid quadrature coupler,” *IEEE Wireless Compon. Lett.*, vol. 27, no. 2, pp. 165–167, Feb. 2017. doi: 10.1109/LMWC.2016.2646909.
- [20] E. Lourandakis, R. Weigel, H. Mextorf, and R. Knoechel, “Circuit agility,” *IEEE Microw. Mag.*, vol. 13, no. 1, pp. 111–121, Jan./Feb. 2012. doi: 10.1109/MMM.2011.2173987.
- [21] F. Lin and M. Rais-Zadeh, “Continuously tunable 0.55–1.9 GHz bandpass filter with a constant bandwidth using switchable varactor-tuned resonators,” *IEEE Trans. Microw. Theory Techn.*, vol. 65, no. 3, pp. 792–803, Mar. 2017. doi: 10.1109/TMTT.2016.2633270.
- [22] F. Lin, S. W. Wong, and Q.-X. Chu, “Compact design of planar continuously tunable crossover with two-section coupled lines,” *IEEE Trans. Microw. Theory Techn.*, vol. 62, no. 3, pp. 408–415, Mar. 2014. doi: 10.1109/TMTT.2014.2300444.
- [23] S. Oh et al., “An unequal Wilkinson power divider with variable dividing ratio,” in *Proc. Int. Microw. Symp. Dig. (IEEE MTT-5)*, 2007, pp. 411–414. doi: 10.1109/MWSYM.2007.380475.
- [24] K. M. J. Ho and G. M. Rebeiz, “A 0.9–1.5 GHz microstrip antenna with full polarization diversity and frequency agility,” *IEEE Trans. Antennas Propag.*, vol. 62, no. 5, pp. 2398–2406, May 2014. doi: 10.1109/TAP.2014.2307295.
- [25] J.-S. Row and M.-J. Hou, “Design of polarization diversity patch antenna based on a compact reconfigurable feeding network,” *IEEE Trans. Antennas Propag.*, vol. 62, no. 10, pp. 5349–5352, Oct. 2014. doi: 10.1109/TAP.2014.2341271.
- [26] S. Y. Zheng, W. S. Chan, and Y. S. Wong, “Reconfigurable RF quadrature patch hybrid coupler,” *IEEE Trans. Ind. Electron.*, vol. 60, no. 8, pp. 3349–3359, Aug. 2013. doi: 10.1109/TIE.2012.2200224.
- [27] K. M. Cheng and S. Yeung, “A novel rat-race coupler with tunable power dividing ratio, ideal port isolation, and return loss performance,” *IEEE Trans. Microw. Theory Techn.*, vol. 61, no. 1, pp. 55–60, Jan. 2013. doi: 10.1109/TMTT.2012.2228219.
- [28] M. Zhou, J. Shao, B. Arigong, H. Ren, R. Zhou, and H. Zhang, “A varactor based 90 directional coupler with tunable coupling ratios and reconfigurable responses,” *IEEE Trans. Microw. Theory Techn.*, vol. 62, no. 3, pp. 416–421, Mar. 2014. doi: 10.1109/TMTT.2014.2299522.
- [29] F. Lin, “Compact design of planar quadrature coupler with improved phase responses and wide tunable coupling ratios,” *IEEE Trans. Microw. Theory Techn.*, vol. 66, no. 3, pp. 1263–1272, Mar. 2018. doi: 10.1109/TMTT.2017.2783375.
- [30] L. L. Jie, Q. Cui, and F. Lin, “Reconfigurable HMSIW quadrature coupler,” *IEEE Microw. Wireless Compon. Lett.*, vol. 29, no. 10, pp. 648–651, Oct. 2019. doi: 10.1109/LMWC.2019.2937651.
- [31] F. Lin and H. Ma, “Design of a class of filtering couplers with reconfigurable frequency,” *IEEE Trans. Microw. Theory Techn.*, vol. 66, no. 9, pp. 4017–4028, Sept. 2018. doi: 10.1109/TMTT.2018.2842755.
- [32] X. Tan and F. Lin, “A novel Rat-Race coupler with widely tunable frequency,” *IEEE Trans. Microw. Theory Techn.*, vol. 67, no. 3, pp. 957–967, Mar. 2019. doi: 10.1109/TMTT.2018.2889453.
- [33] M. F. Hagag, R. Zhang, and D. Peroulis, “High-performance tunable narrowband SIW cavity-based quadrature hybrid coupler,” *IEEE Microw. Wireless Compon. Lett.*, vol. 29, no. 1, pp. 41–43, Jan. 2019. doi: 10.1109/LMWC.2018.2884238.
- [34] K. Fathy, E. Mansour, N. Nasr, M. Emad, M. Ali, and H. Hammad, “Adaptable reconfigurable antenna array system with multi-angle and tri-polarization diversity,” *IEEE Antennas Propag. Mag.*, vol. 56, no. 5, pp. 223–237, Oct. 2014. doi: 10.1109/MAP.2014.6971956.
- [35] Y.-S. Liu and J.-S. Row, “Back-to-back microstrip antenna fed with tunable power divider,” *IEEE Trans. Antennas Propag.*, vol. 63, no. 5, pp. 2348–2353, May 2015. doi: 10.1109/TAP.2015.2407377.
- [36] T. Djeraji, J. Gauthier, and K. Wu, “Variable coupler for Butler beamforming matrix with low sidelobe level,” *IET Microw. Antennas Propag.*, vol. 6, no. 9, pp. 1034–1039, June 2012. doi: 10.1049/iet-map.2011.0297.
- [37] Y. Xiao, F. Lin, H. Ma, X. Tan, and H. Sun, “A planar balanced power divider with tunable power-dividing ratio,” *IEEE Trans. Microw. Theory Techn.*, vol. 65, no. 12, pp. 4871–4882, Dec. 2017. doi: 10.1109/TMTT.2017.2722403.
- [38] P.-L. Chi and C.-P. Chien, “Balanced-to-balanced power divider with tunable in-phase/out-of phase power-dividing ratio,” in *Proc. Asia-Pacific Microw. Conf.*, 2018, pp. 1483–1485.
- [39] F. Lin, “A planar balanced quadrature coupler with tunable power-dividing ratio,” *IEEE Trans. Ind. Electron.*, vol. 65, no. 8, pp. 6515–6526, Aug. 2018. doi: 10.1109/TIE.2017.2786290.
- [40] D. E. Bockelman and W. R. Eisenstadt, “Combined differential and common-mode scattering parameters: Theory and simulation,” *IEEE Trans. Microw. Theory Techn.*, vol. 43, no. 7, pp. 1530–1539, July 1995. doi: 10.1109/22.392911.
- [41] S. Y. Zheng, W. S. Chan, and K. F. Man, “Frequency-agile patch element using varactor loaded patterned ground plane,” *IEEE Trans. Microw. Theory Techn.*, vol. 59, no. 3, pp. 619–626, Mar. 2011. doi: 10.1109/TMTT.2010.2098038.
- [42] Q. Cui and F. Lin, “Continuously tunable crossover based on HMSIW,” *Electron. Lett.*, vol. 53, no. 24, pp. 1582–1583, 2017. doi: 10.1049/el.2017.3221.
- [43] M. A. Y. Abdalla, K. Phang, and G. V. Eleftheriades, “A compact highly reconfigurable CMOS MMIC directional coupler,” *IEEE Trans. Microw. Theory Techn.*, vol. 56, no. 2, pp. 305–319, Feb. 2008. doi: 10.1109/TMTT.2007.913360.
- [44] J. Sun, C. Li, Y. Geng, and P. Wang, “A highly reconfigurable low-power CMOS directional coupler,” *IEEE Trans. Microw. Theory Techn.*, vol. 60, no. 9, pp. 2815–2822, Sept. 2012. doi: 10.1109/TMTT.2012.2204275.
- [45] R. Zhang, M. F. Hagag, L. Yang, R. Gómez-García, and D. Peroulis, “A flexible quadrature coupler with reconfigurable frequency and coupling ratio in switchable coupling direction,” *IEEE Trans. Microw. Theory Techn.*, vol. 67, no. 8, pp. 3391–3402, Aug. 2019. doi: 10.1109/TMTT.2019.2918528.
- [46] H. Zhu and A. M. Abbosh, “A compact tunable directional coupler with continuously tuned differential phase,” *IEEE Microw. Wireless Compon. Lett.*, vol. 28, no. 1, pp. 19–21, Jan. 2018. doi: 10.1109/LMWC.2017.2779819.
- [47] F. Lin, Q. X. Chu, and S. W. Wong, “Design of dual-band filtering quadrature coupler using $\lambda/2$, and $\lambda/4$ resonators,” *IEEE Microw. Wireless Compon. Lett.*, vol. 22, no. 11, pp. 565–567, Nov. 2012. doi: 10.1109/LMWC.2012.2224650.
- [48] L. Gao, X. Y. Zhang, and Q. Xue, “Compact tunable filtering power divider with constant absolute bandwidth,” *IEEE Trans. Microw. Theory Techn.*, vol. 63, no. 10, pp. 3505–3513, Oct. 2015. doi: 10.1109/TMTT.2015.2454731.
- [49] F. Lin and H. Ma, “Design method of frequency-reconfigurable filtering couplers,” in *Proc. Microw. Conf. Asia Pacific (APMC)*, Dec. 2018, pp. 1501–1503.



OPEN FOR PAPER SUBMISSION



IEEE Journal of Microwaves

"Expanding science, technology and connectivity across the globe."

IEEE Journal of Microwaves has launched and is open for new manuscript submission at:
<https://mtt.org/publications/journal-of-microwaves>

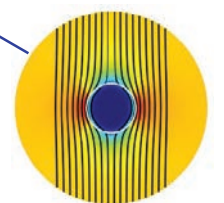
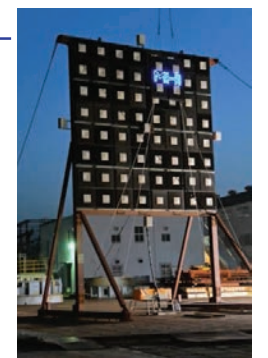
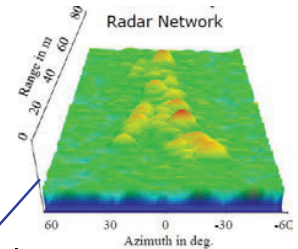
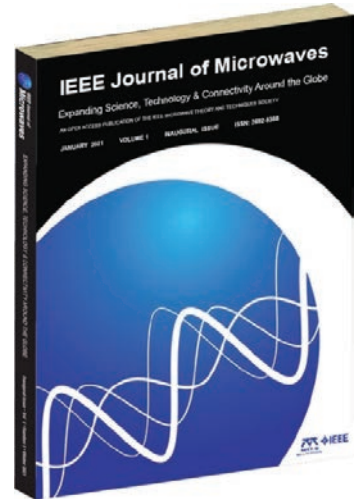
IEEE Journal of Microwaves (JMW) is our new Gold Open Access publication covering the complete scope of the Microwave Theory and Techniques Society: MHz to THz.

Get a **FREE** copy of our **500+ page INAUGURAL ISSUE** mailed directly to you by signing up at:
<https://mtt.org/publications/journal-of-microwaves/inaugural-issue>

You will NOT want to miss having this archival volume on your shelf!

IEEE JOURNAL OF MICROWAVES INAUGURAL ISSUE TABLE OF CONTENTS

INTRODUCTION TO THE IEEE JOURNAL OF MICROWAVES	<i>P.H. Siegel</i>
SPECIAL EDITORIAL ARTICLES	
Microwaves are Everywhere: "CMB: Hiding in Plain Sight"	<i>P.H. Siegel</i>
Microwave Pioneers: John C. Mather, "A Singular Purpose"	<i>P.H. Siegel</i>
Microwaves in Chemistry	<i>D.R. Slocombe and A. Porch</i>
Instrumentation for THz Spectroscopy in the Laboratory and in Space	<i>J. Pearson, B. Drouin et al.</i>
Innovative RFID Sensors for Internet of Things Applications	<i>P. Mezzanotte et al.</i>
Sensing of Life Activities at the Human-Microwave Frontier	<i>C. Li et al.</i>
SPECIAL EDITORIAL ARTICLE	
On the Shoulders of Giants: Reflections on the Creators and Uses of Radio	<i>Tom Lewis</i>
Implementation Challenges and Opportunities in Beyond-5G and 6G Communication	<i>U. Gustavsson et al.</i>
The Role of Millimeter-Wave Technologies in 5G/6G Wireless Communications	<i>W.Hong et al.</i>
Packaging and Antenna Integration for Silicon-Based Millimeter-Wave Phased Arrays: 5G and Beyond	<i>X. Gu et al.</i>
Automotive Radar – From First Efforts to Future Systems	<i>C. Waldschmidt et al.</i>
Coherent Automotive Radar Networks: The Next Generation of Radar-Based Imaging and Mapping	<i>M. Gottinger et al.</i>
RF Systems Design for Simultaneous Wireless Information and Power Transfer (SWIPT) in Automation and Transportation	<i>D. Masotti et al.</i>
Microwave Photonic Array Radars	<i>S. Pan et al.</i>
Microwave Imaging in Security – Two Decades of Innovation	<i>S. Ahmed</i>
Millimeter Sensing with Microwaves: Precise Radar Systems for Innovative Measurement Applications	<i>F. Michler et al.</i>
History and Innovation of Wireless Power Transfer via Microwaves	<i>N. Shinohara</i>
Microwave and Millimeter Wave Power Beaming	<i>C. Rodenbeck et al.</i>
Russian Gyrotrons: Achievements and Trends	<i>A. Litvak et al.</i>
SPECIAL EDITORIAL ARTICLE	
Carver Mead: "It's All About Thinking." A Personal Account Leading up to the First Microwave Transistor ...	<i>P.H. Siegel</i>
CNTFET Technology for RF Applications: Review and Future Perspective	<i>M. Hartmann et al.</i>
SiGe HBTs and BiCMOS Technology for Present and Future Millimeter-wave systems	<i>T. Zimmer et al.</i>
Millimeter-Wave Power Amplifier Integrated Circuits for High Dynamic Range Signals	<i>H. Wang et al.</i>
Emerging Trends in Techniques and Technology as Applied to Filter Design	<i>R. Snyder et al.</i>
Substrate Integrated Transmission Lines: Review and Applications	<i>K. Wu et al.</i>
Connecting Chips with more than 100 GHz Bandwidth	<i>W. Heinrich et al.</i>
Microwave Huygen's Metasurfaces: Fundamentals and Applications	<i>G. Eleftheriades et al.</i>
Microwave Superconductivity	<i>S. Anlage</i>
Microwaves in Quantum Computing	<i>J. Bardin et al.</i>
MID-Radio Telescope, Single Pixel Feed Packages for the Square Kilometer Array: An Overview	<i>A. Pellegrini et al.</i>
Microwave Magnetics and Considerations for Systems Design	<i>M. Geiler et al.</i>
Non-Magnetic Non-Reciprocal Microwave Components – State of the Art and Future Directions	<i>A. Nagulu and H. Krishnaswamy</i>
On the Benefits of Glide Symmetries for Microwave Devices	<i>O. Quevedo-Teruel et al.</i>
Sommerfeld Integrals and their Relation to the Development of Planar Microwave Devices	<i>J. Mosig and K. Michalski</i>
Advanced RF and Microwave Design Optimization: A Journey and a Vision of Future Trends	<i>J. Rayas-Sanchez et al.</i>
Simulation and Automated Modeling of Microwave Circuits: State-of-the-Art and Emerging Trends	<i>Q.J. Zhang et al.</i>
Supply Modulation Behavior of a Doherty Power Amplifier	<i>D. Fishler, Z. Popovic and T. Barton</i>





Application Notes

Revisiting the Binomial Multisection Transformer

■ Zubair Ahmed

Presented here is an intuitive method for synthesizing the binomial multisection quarter-wave transformer. I discovered this method while teaching an undergraduate course in microwave engineering and termed it the *Z-method*. I have found that, compared to the approximate method based on the theory of small reflections [1], the *Z-method* is easier for students to grasp. The technique employs successive geometric means for finding the characteristic impedances of a binomial multisection transformer. It can be thought of as an extension of single-section, quarter-wave transformer design.

The *Z-method* uses an iterative process in which an N -section transformer design requires N iterations. When it is compared with the approximate method based on the theory of small reflections [1] for synthesizing a binomial multisection transformer, it shows excellent correlation.

Stepped-impedance transformers are routinely used for broadband impedance matching of resistive loads. Two common methods for multisection transformer design are binomial (maximally flat) and Chebyshev (equal ripple). The binomial transformer method gives the monotonic or flattest passband reflection coefficient, whereas the Chebyshev transformer provides a better bandwidth.

Zubair Ahmed (zubair.ahmed@ee.ceme.edu.pk) is with the College of Electrical and Mechanical Engineering, National University of Sciences and Technology, Islamabad, Pakistan.

Digital Object Identifier 10.1109/MMM.2020.3035865
Date of current version: 11 January 2021



The main idea behind using multisection transformers for improving the bandwidth of a single-section transformer is that smaller contrast or discontinuity between load Z_L and the transmission line characteristic impedance Z_0 gives a larger bandwidth. This is based on the fact that, in general, a transformer's voltage standing-wave ratio (VSWR) variation with frequency depends on mismatch before inserting the transformer. The larger mismatch between the load and line impedance results in greater VSWR variation with frequency.

A binomial transformer is also known as an *optimum maximally flat stepped-impedance transformer* [2], and its design concept has been used in various wide-band applications, such as Wilkinson dividers, filters, antennas, and array feed networks [3]–[7]. The design of a binomial multisection quarter-wave transformer involves finding the impedances of N sections located between Z_0 and Z_L , as shown in Figure 1. In the past, different techniques have been employed for the synthesis of a binomial transformer. A common method used by early microwave designers was to express the logarithmic impedance ratio for different sections of a multisection transformer as being proportional to the binomial coefficients, according to the following empirical formula [8]–[9]:

$$\log \frac{Z_{n+1}}{Z_n} = kC_n^N$$

$$n = 0, 1, 2, 3, \dots, N, \quad (1)$$

where k is a constant and C_n^N are binomial coefficients. However, this method does not give the maximally flat response [10].

Another approach is to express the partial reflection coefficients of each section proportional to binomial coefficients [11], [12] (i.e., $\Gamma_n = AC_n^N$, where A is a constant). In this method, the theory of small reflections is used to express the total input reflection coefficient as a polynomial, comprising terms representing the first bounce from each junction.

The desired frequency response (i.e., the binomial frequency response) can also be expressed as a polynomial. This requires the selection of roots that satisfy the constraint placed on the frequency behavior of the total input reflection coefficient Γ . For binomial transformers, all of the roots are placed at a common location: -1 on a unit circle in the complex plane [12]. Γ_n can be synthesized by equating the coefficients of both aforementioned polynomials. Once reflection coefficients at the junctions of the multisection transformer are known, corresponding line impedances can be calculated.

However, because there are N impedances and $N + 1$ reflection coefficients, the last reflection coefficient cannot be controlled, which results in inconsistency in the load check: $Z_{N+1} \neq Z_L$. Moreover, multisection transformer impedances are different when they are calculated for the source side or the load side. In addition, this technique cannot guarantee a maximally flat response.

An improved method using the theory of small reflections and an additional approximation for calculating the characteristic impedances is presented in [1]. This method is more consistent and is used as a standard approach today in many microwave engineering textbooks [13]–[17]. It is worthwhile to point out that, without additional approximations for calculating the

The design of a binomial transformer can be greatly simplified if it is possible to extend the simple geometric mean-based approach to a multisection transformer.

characteristic impedances, the methods in both [1] and [12] are identical.

In [18], an alternate formulation for the derivation of the same result given in [1] is presented. As the theory used in [1] is approximate, it will not hold for large steps in impedances between Z_0 and Z_L . An exact method, which takes into account multiple reflections and involves a numerical solution, is provided in [19]. The results of such calculations are available in tabular form, providing ease of use for engineering applications [13], [19].

It is well known that the design of a single-section quarter-wave transformer can be carried out by taking the geometric mean of the load and line impedances. However, to the best of my knowledge, no such procedure exists for the design of a binomial multisection transformer. The design of a binomial transformer can be greatly simplified if it is possible to extend the simple geometric mean-based approach to a multisection transformer.

The purpose of this article is to present a simple method for synthesizing the characteristic impedances of a binomial multisection transformer. The proposed method, called the *Z-method* as previously noted, does not involve any complex design formulas; instead, it uses successive geometric means for the synthesis of a binomial multisection transformer.

Design Procedure and Theoretical Background

Consider a general impedance matching problem of synthesizing the unknown characteristic impedances Z_1, Z_2, \dots, Z_N between some resistive load Z_L and transmission line impedance Z_0 using an N -section binomial quarter-wave transformer, as shown in Figure 1. The design procedure employing the *Z-method* can be understood with the help of Figure 2. To better explain the design process, it is divided into two steps. In

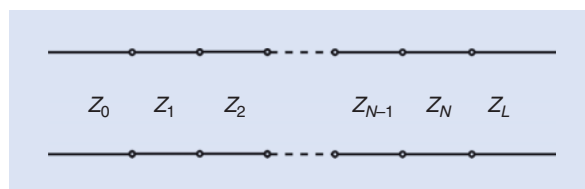


Figure 1. A general N -section binomial transformer.

the first step, N is arbitrarily restricted to a fixed value $N = 4$; in the second step, this restriction is relaxed based on observations from the first step, leading to a generalized design formula.

It is important to note that the main purpose of this article is to simplify the calculation of a multisection binomial impedance transformer. In fact, the design of a binomial transformer can be carried out by simply taking the successive geometric means without the need for a generalized formula. However, as is shown later in this section, the generalized design formula can be used to compare the Z -method with the approximate method based on the theory of small reflections [1].

Figure 2 shows the design of a four-section binomial transformer using the Z -method. The Z -method

employs an iterative process that requires N iterations. In the first iteration ($N = 1$), we synthesize the single-section transformer by taking the geometric mean of load Z_L and transmission line impedance Z_0 . In the second iteration ($N = 2$), the characteristic impedance of a single-section transformer acts as an input impedance at the junction between two sections of the transformer, as indicated by the dashed line in Figure 2. The design of the two-section transformer is completed by taking the geometric mean of the input impedance with Z_L and Z_0 , respectively.

In the third iteration ($N = 3$), characteristic impedances of two-section transformers serve as input impedances at the junctions among the three sections of the transformer, as indicated by the dashed lines in

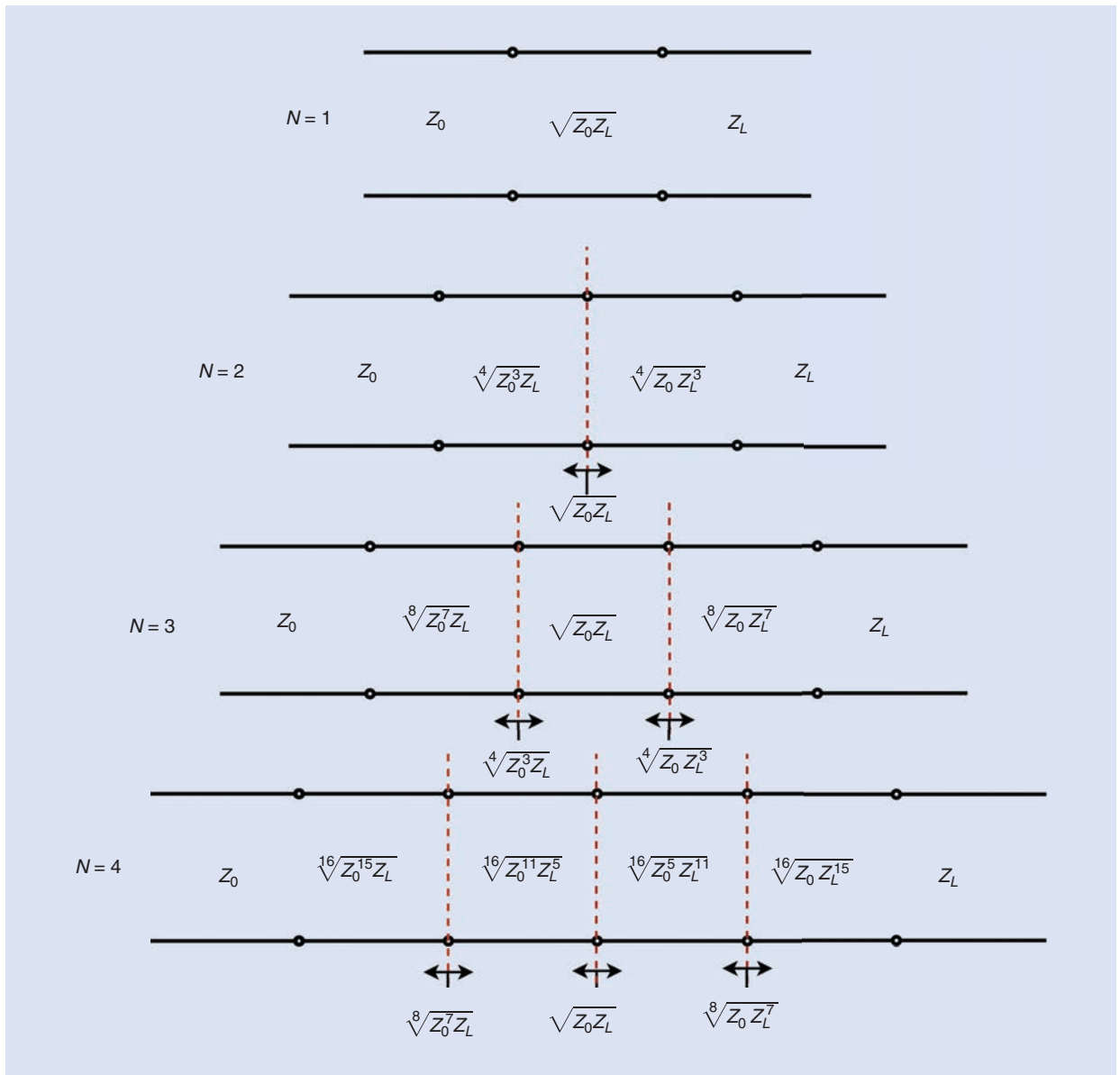


Figure 2. A general four-section binomial transformer design using the Z -method.

Figure 2. The design of the three-section transformer is completed by taking three geometric means, as shown in Figure 2. In the fourth iteration ($N = 4$), characteristic impedances of the three-section transformer act as input impedances at the junctions among the four sections of the transformer, as indicated by dashed lines in Figure 2. The design of the desired four-section binomial transformer can now be completed by taking four geometric means, as shown in Figure 2.

The following observations can be made from the four-section binomial transformer design using the Z-method:

- For odd iterations $N = 1, 3, 5, \dots$, the center element characteristic impedance is always $Z_{(N+1)/2} = \sqrt{Z_0 Z_L}$.
- For each iteration, the characteristic impedance of the first transformer close to Z_0 is $Z_1 = 2^N \sqrt{Z_0^{2^{N-1}} Z_L}$, whereas the characteristic impedance of the last transformer close to Z_L is $Z_N = 2^N \sqrt{Z_0 Z_L^{2^{N-1}}}$.
- For each iteration, the powers of Z_0 and Z_L within the 2^N root follow a specific pattern based on binomial coefficients corresponding to row N of Pascal's triangle. For $N = 4$, binomial coefficients are given by 1, 4, 6, 4, and 1. It can be seen from Table 1 that, for the first transformer, the power of Z_0 is the sum of 1, 4, 6, and 4 and the power of Z_L is 1. For the second transformer, the power of Z_0 is the sum of 1, 4, and 6, and the power of Z_L is the sum of 4 and 1. Similarly, the powers of Z_0 and Z_L for Z_3 and Z_4 can be found as indicated in Table 1.
- These observations can be used to find the generalized design formula for synthesizing the binomial transformer impedances using the Z-method as given in (2):

$$Z_{n+1} = 2^N \sqrt{Z_0^{2^N - M_n} Z_L^{M_n}}$$

$$n = 0, 1, 2, 3, \dots, N - 1$$

$$M_n = \sum_n C_n^N, \quad (2)$$

where N is the number of sections and C_n^N are binomial coefficients.

Using (2), the impedances of an N -section binomial transformer can be calculated. As shown in "Proof Using the Theory of Small Reflections," (2) can also be derived using the theory of small reflections and additional approximations for calculating the characteristic impedances. It is worthwhile to compare the Z-method with the approximate method based on the theory of small reflections. In [14], the following expression for calculating the characteristic impedances of a binomial multisection transformer is given using the theory of small reflections:

$$Z_{n+1} = Z_0 \left(\frac{Z_L}{Z_0} \right)^{\frac{M_n}{2^N}}$$

$$n = 0, 1, 2, 3, \dots, N - 1. \quad (3)$$

This expression is equivalent to generalized formula (2) derived for the Z-method, an intuitively appealing result. Thus, in addition to its simplicity, the Z-method is mathematically equivalent to the results of a more mathematically involved technique based on the theory of small reflections [1].

Design Examples

The design of a binomial multisection transformer using the Z-method is illustrated by two examples.

Example 1: Three-Section Binomial Transformer ($Z_0 = 100 \Omega$, $Z_L = 50 \Omega$)

Consider a load $Z_L = 50 \Omega$ that needs to be matched with a transmission line having characteristic impedance $Z_0 = 100 \Omega$ using a three-section ($N = 3$) binomial transformer. The design problem is to find three impedances, Z_1 , Z_2 , and Z_3 , as shown in Figure 3.

The design procedure can be explained with the help of Figure 4. First, we find the single-section quarter-wave transformer impedance by taking the geometric mean of 100Ω and 50Ω . The impedance of the single-section transformer (i.e., 70.71Ω) now serves as the input impedance at the center of a two-section transformer indicated by the dashed line. The impedances of the two-section transformer can be calculated by taking the geometric mean of 70.71Ω with $100\text{-}\Omega$ line and $50\text{-}\Omega$ load, as shown in Figure 4. The two-section transformer impedances come out to be 84.09 and 59.46Ω , respectively.

The desired three-section transformer can now be designed, with the impedances of the two-section transformer acting as input impedances at the junctions

TABLE 1. The trend for the power of Z_0 (blue color) and Z_L (peach color) for a four-section binomial transformer.

	$C_0^4 = 1$	$C_1^4 = 4$	$C_2^4 = 6$	$C_3^4 = 4$	$C_4^4 = 1$
$Z_1 = {}^{16}\sqrt{Z_0^{15} Z_L^1}$	1	4	6	4	1
$Z_2 = {}^{16}\sqrt{Z_0^{11} Z_L^5}$	1	4	6	4	1
$Z_3 = {}^{16}\sqrt{Z_0^5 Z_L^{11}}$	1	4	6	4	1
$Z_4 = {}^{16}\sqrt{Z_0^1 Z_L^{15}}$	1	4	6	4	1

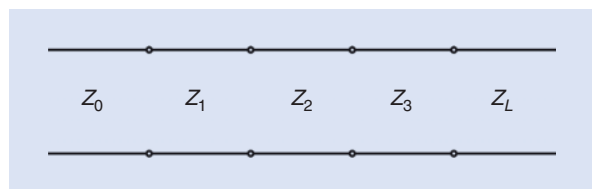


Figure 3. A three-section binomial transformer.

Proof Using the Theory of Small Reflections

Using the theory of small reflections (Figure S1), the total input reflection coefficient Γ of a multisection transformer can be written as a polynomial:

$$\begin{aligned}\Gamma &= \Gamma_0 + \Gamma_1 e^{-j2\theta} + \dots + \Gamma_{N-1} e^{-j2(N-1)\theta} + \Gamma_N e^{-j2N\theta} \\ &= \sum_{n=0}^N \Gamma_n e^{-j2n\theta},\end{aligned}\quad (S1)$$

where partial reflection coefficients Γ_n are given by

$$\Gamma_n = \frac{Z_{n+1} - Z_n}{Z_{n+1} + Z_n}.\quad (S2)$$

The reflection coefficient of the desired binomial response can be expressed as the following polynomial:

$$\Gamma = A(1 + e^{-j2\theta})^N = A \sum_{n=0}^N C_n^N e^{-j2n\theta},\quad (S3)$$

where the binomial coefficients C_n^N are given by

$$C_n^N = \frac{N!}{(N-n)!n!}.$$

Comparing (S1) and (S3), we get

$$\Gamma_n = AC_n^N.\quad (S4)$$

The constant A can be found by equating (S1) and (S3) at dc (i.e., $\theta = 0$). This makes the electrical length of all of the sections zero, and we get

$$A = \frac{\Gamma_0}{2^N} = \frac{1}{2^N} \frac{Z_L - Z_0}{Z_L + Z_0}.\quad (S5)$$

The characteristic impedances of the multisection transformer can now be computed using

$$Z_{n+1} = Z_n \frac{1 + \Gamma_n}{1 - \Gamma_n}.$$

However, due to the approximate nature of the theory, load consistency is not achieved (i.e., $Z_{N+1} \neq Z_L$). The following approximation can be used to improve the accuracy:

$$\frac{y-x}{y+x} \approx \frac{1}{2} \ln\left(\frac{y}{x}\right) \text{ for small } |y-x| \text{ that is } \frac{y}{x} \approx 1. \quad (S6)$$

Using (S6), we can rewrite (S5) and (S2) as

$$A \approx \frac{1}{2^{N+1}} \ln\left(\frac{Z_L}{Z_0}\right)\quad (S7)$$

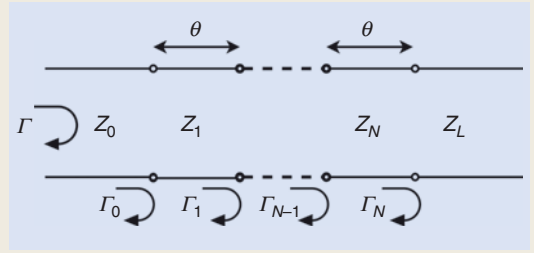


Figure S1. A multisection transformer using the theory of small reflections.

$$\Gamma_n \approx \frac{1}{2} \ln\left(\frac{Z_{n+1}}{Z_n}\right).\quad (S8)$$

Entering (S7) and (S8) in (S4), we get

$$\begin{aligned}\frac{1}{2} \ln\left(\frac{Z_{n+1}}{Z_n}\right) &= \frac{C_n^N}{2^{N+1}} \ln\left(\frac{Z_L}{Z_0}\right) \\ Z_{n+1} &= Z_n \left(\frac{Z_L}{Z_0}\right)^{\frac{C_n^N}{2^N}}.\end{aligned}\quad (S9)$$

We can calculate the multisection transformer line impedances using iterative (S9). To obtain a noniterative equation, we can express (S9) in N equations given by

$$Z_1 = Z_0 \left(\frac{Z_L}{Z_0}\right)^{\frac{C_0^N}{2^N}}\quad (S9.1)$$

$$Z_2 = Z_1 \left(\frac{Z_L}{Z_0}\right)^{\frac{C_1^N}{2^N}}\quad (S9.2)$$

⋮

$$Z_N = Z_{N-1} \left(\frac{Z_L}{Z_0}\right)^{\frac{C_{N-1}^N}{2^N}}.\quad (S9.N)$$

Entering (S9.1) in (S9.2), we get

$$Z_2 = Z_0 \left(\frac{Z_L}{Z_0}\right)^{\frac{C_0^N + C_1^N}{2^N}}.$$

In general, we can write the characteristic impedance of any section as

$$\begin{aligned}Z_{n+1} &= Z_0 \left(\frac{Z_L}{Z_0}\right)^{\frac{C_0^N + C_1^N + \dots + C_n^N}{2^N}} \\ Z_{n+1} &= Z_0 \left(\frac{Z_L}{Z_0}\right)^{\frac{M_n}{2^N}},\end{aligned}\quad (S10)$$

where $M_n = C_0^N + C_1^N + \dots + C_n^N$.

We can also write (S10) as

$$Z_{n+1} = 2^N \sqrt[Z_0^{2^N - M_n} Z_L^{M_n}].\quad (S11)$$

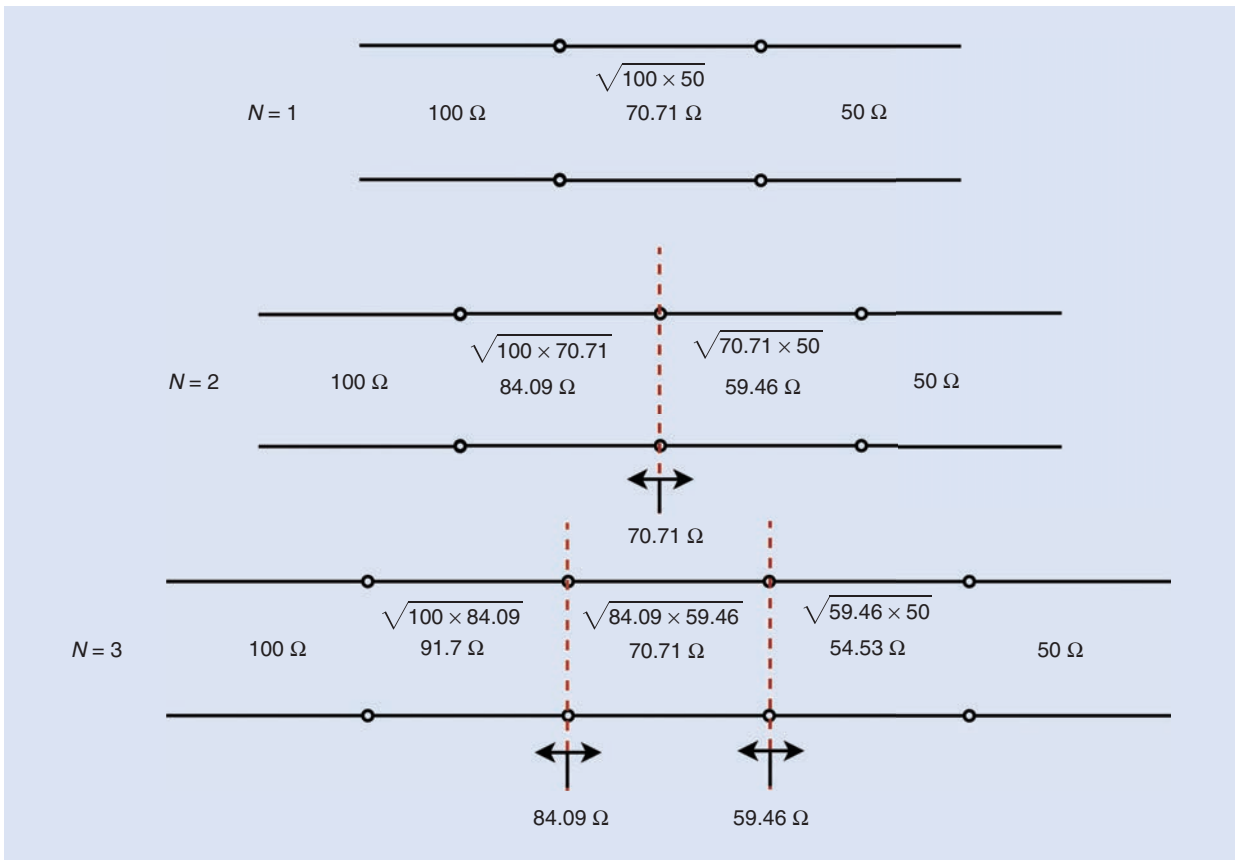


Figure 4. A three-section binomial transformer design using the Z-method.

of the three-section transformer, as indicated by the dashed lines in Figure 4. The impedances of the three-section transformer can be calculated by taking three geometric means, as shown in Figure 4. This completes the design of a three-section binomial transformer. The final impedances are $Z_1 = 91.7 \Omega$, $Z_2 = 70.71 \Omega$, and $Z_3 = 54.53 \Omega$.

Table 2 shows a comparison of impedances calculated using the Z-method with four methods available in the literature, namely, the empirical method [8], approximate methods using the theory of small reflections without additional approximation [12] and with additional approximation [1],

TABLE 2. The three-section binomial transformer impedances: $Z_0 = 100 \Omega$, and $Z_L = 50 \Omega$.

	$Z_1 (\Omega)$	$Z_2 (\Omega)$	$Z_3 (\Omega)$
Empirical method [8]	91.69	70.71	54.53
Approximate method 1 [12]	89.85	69.88	54.35
Approximate method 2 [1]	91.7	70.71	54.53
Exact method [13]	91.69	70.71	54.54
Z-method	91.7	70.71	54.53

and the exact method [13]. It can be seen that the Z-method results are identical to the approximate method given in [1].

The reflection coefficient-versus-frequency plot of a three-section binomial transformer is shown in Figure 5. In the figure, approximate method 1 deviates from the desired binomial response, whereas all of the other methods give almost identical results.

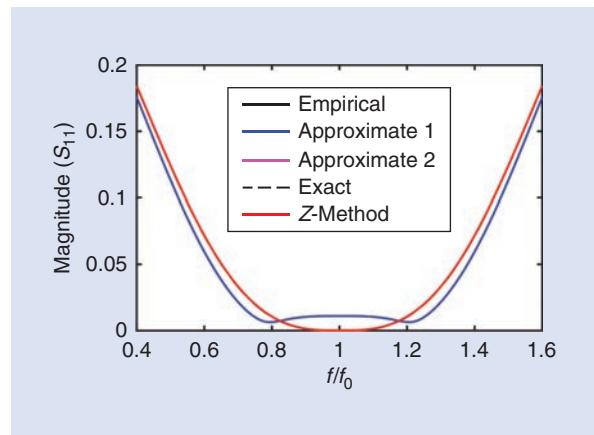


Figure 5. The S_{11} of a three-section binomial transformer.

Example 2: Five-Section Binomial Transformer ($Z_0 = 50 \Omega$, $Z_L = 200 \Omega$)

Given a load $Z_L = 200 \Omega$ that needs to be matched with a transmission line having characteristic impedance

$Z_0 = 50 \Omega$ using a five-section ($N = 5$) binomial transformer, the design problem is to find five impedances $Z_1, Z_2, Z_3, Z_4,$ and Z_5 , as shown in Figure 6.

The design procedure can be understood with the help of Figure 7. The design steps are identical to Example 1 and are, for the sake of brevity, not repeated here. The final impedances are $Z_1 = 52.22 \Omega$, $Z_2 = 64.84 \Omega$, $Z_3 = 100 \Omega$, $Z_4 = 154.22 \Omega$, and $Z_5 = 191.52 \Omega$.

A comparison of impedances calculated using the Z-method with four methods, namely, the empirical method [8], approximate methods using the theory of small reflections without [12] and with additional approximation [1], and the exact method [13], is shown

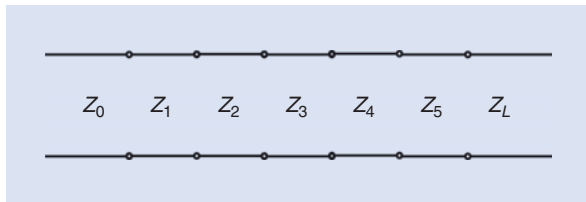


Figure 6. A five-section binomial transformer.

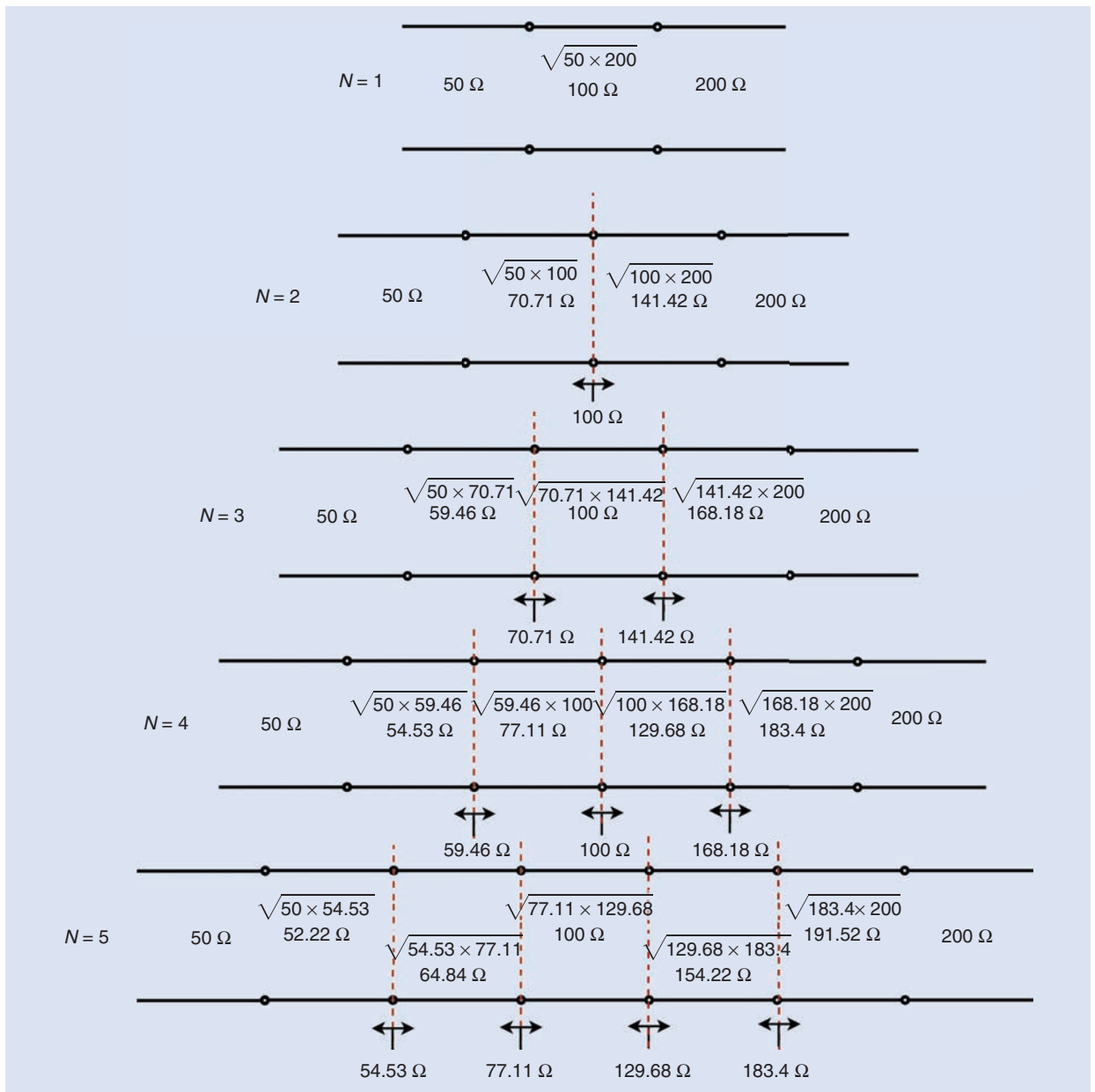


Figure 7. A five-section binomial transformer design using the Z-method.

TABLE 3. The five-section binomial transformer impedances: $Z_0 = 50 \Omega$, and $Z_L = 200 \Omega$.

	$Z_1 (\Omega)$	$Z_2 (\Omega)$	$Z_3 (\Omega)$	$Z_4 (\Omega)$	$Z_5 (\Omega)$
Empirical method [8]	52.21	64.81	100	154.3	191.53
Approximate method 1 [12]	51.91	62.65	91.56	133.83	161.52
Approximate method 2 [1]	52.21	64.84	100	154.22	191.52
Exact method [13]	52.26	64.98	100	153.91	191.35
Z-method	52.22	64.84	100	154.22	191.52

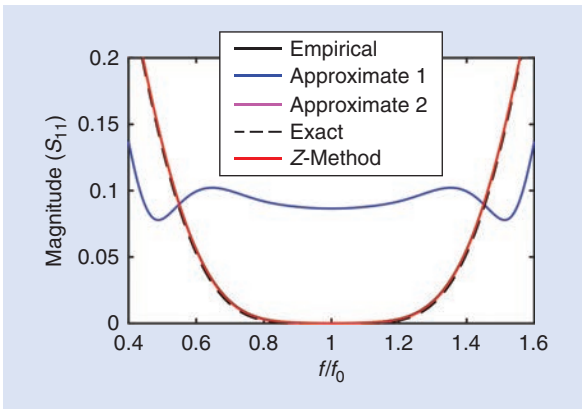


Figure 8. The S_{11} of a five-section binomial transformer.

in Table 3. The Z-method results are identical to the approximate method 2 [1]. The small discrepancy in Z_1 is due to numerical error, which can be easily reduced by increasing the number of significant digits.

Figure 8 shows the reflection coefficient-versus-frequency plot of a five-section binomial transformer. Approximate method 1 does not match the desired maximally flat response, whereas all of the other methods closely match the exact method.

Conclusions

This article presents a simple method for synthesizing a binomial multisection quarter-wave transformer. Inspired by single-section quarter-wave transformer design, successive geometric means are employed for the design of a binomial multisection transformer. The proposed Z-method gives identical results to those obtained using an approximate method based on the theory of small reflections [1]. Further investigation shows that both methods are mathematically equivalent. By avoiding mathematical complexity, the proposed method makes the design of binomial multisection quarter-wave transformers much simpler, and it can be

By avoiding mathematical complexity, the proposed method makes the design of binomial multisection quarter-wave transformers much simpler.

used by microwave designers as an alternative to the theory of small reflections for the synthesis of binomial multisection transformers.

References

- [1] R. E. Collin, *Foundations for Microwave Engineering*. Hoboken, NJ: Wiley, 2007.
- [2] H. J. Riblet, "A general theorem on an optimum stepped impedance transformer," *IRE Trans. Microw. Theory Techn.*, vol. 8, no. 2, pp. 169–170, Mar. 1960. doi: 10.1109/TMTT.1960.1124718.
- [3] G. S. Makinen and W. T. Joines, "Comparison of broadband performance of two-way power dividers and combiners," *Microw. Opt. Technol. Lett.*, vol. 17, no. 1, pp. 29–37, Jan. 1998. doi: 10.1002/(SICI)1098-2760(199801)17:1<29::AID-MOP7>3.0.CO;2-L.
- [4] L. Young, "Stepped-impedance transformers and filter prototypes," *IRE Trans. Microw. Theory Techn.*, vol. MTT-10, pp. 339–359, Sept. 1962.
- [5] J. M. Drozd and W. T. Joines, "Using the binomial transformer to approximate the Q distribution for maximally flat quarter-wave-length-coupled filters," *IEEE Trans. Microw. Theory Techn.*, vol. 46, no. 10, pp. 1495–1500, Oct. 1998. doi: 10.1109/22.721153.
- [6] Y. Charoensiri, W. Thaiwirot and P. Akkarakethalin, "Design of ultra-wideband tapered slot antenna by using binomial impedance transformer," in *Proc. IEEE Conf. Antenna Measurements & Applications (CAMA)*, Chiang Mai, pp. 1–4. 2015. doi: 10.1109/CAMA.2015.7428129.
- [7] K. Ding and A. A. Kishk, "Multioctave bandwidth of parallel feeding network based on impedance transformer concept," *IEEE Trans. Antennas Propag.*, vol. 67, no. 4, pp. 2803–2808, Apr. 2019. doi: 10.1109/TAP.2019.2893893.
- [8] M. H. Johnson and W. W. Hansen, "Wave guide impedance transformer," U.S. Patent 2 531 437, Nov. 28, 1950.
- [9] G. C. Southworth, *Principles and Application of Waveguide Transmission*. New York: Van Nostrand, pp. 272–273, 1950.
- [10] R. Collin, "Theory and design of wideband multisection quarter-wave transformers," *Proc. IRE*, vol. 43, no. 2, pp. 179–185, 1955. doi: 10.1109/JRPROC.1955.278076.
- [11] G. J. Halford, "A wide-band waveguide phase-shifter," in *Proc. IEE-Part III: Radio and Commun. Eng.*, vol. 100, pp. 117–124, May 1953. Doi: 10.1049/pi-3.1953.0029.
- [12] R. S. Elliott, *An Introduction To Guided Waves and Microwave Circuits*. Englewoods Cliffs, NJ: Prentice-Hall, 1993.
- [13] D. M. Pozar, *Microwave Engineering*. Hoboken, NJ: Wiley, 2009.
- [14] P. A. Rizzi, *Microwave Engineering—Passive Circuits*. Englewoods Cliffs, NJ: Prentice-Hall, 1988.
- [15] M. Steer, *Microwave and RF Design: Networks*. vol. 3. NC State Univ., 2019.
- [16] M. A. Morgan, *Principles of RF and Microwave Design*. Norwood, MA: Artech House, 2019.
- [17] R. Sorrentino and G. Bianchi, *Microwave and RF Engineering*. Hoboken, NJ: Wiley, 2010.
- [18] I. D. Coster, E. Van Lil, and A. Van de Capelle, "Comparison of design methods for binomial matching transformers," *J. Electromagn. Waves Appl.*, vol. 14, no. 9, pp. 1229–1239, 2000. doi: 10.1163/156939300X01139.
- [19] G. Matthaei, L. Young, and E. M. T. Jones, *Microwave Filters, Impedance-Matching Networks, and Coupling Structures*. Norwood, MA: Artech House, 1980.





IMS

Connecting Minds. Exchanging Ideas.

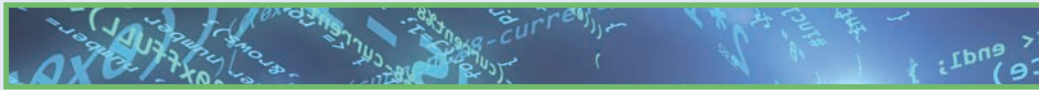
IEEE MTT-S
INTERNATIONAL
MICROWAVE
SYMPOSIUM
IMS2021

EXHIBITION & SPONSORSHIP PREVIEW



6-11 June 2021
ATLANTA • GEORGIA
www.ims-ieee.org/ims2021





Join us in Atlanta, as we come together once again for the world's premier RF and microwave industry conference and tradeshow: IMS2021. Now in its 64th year, IMS is the place to be each year for professionals buying and developing materials, devices, components, systems, design & simulation software, and test & measurement equipment for products operating from RF to THz.

9000 participants from over 50 countries include senior management, engineering management, engineers, and R&D personnel from academia, commercial industry, and government/military. Participating exhibitors can establish new US and international connections, present products directly to industry leaders, and see the state of the art in a showcase of the best developments for applications that enable us to connect for a smarter, safer world.

Georgia World Congress Center

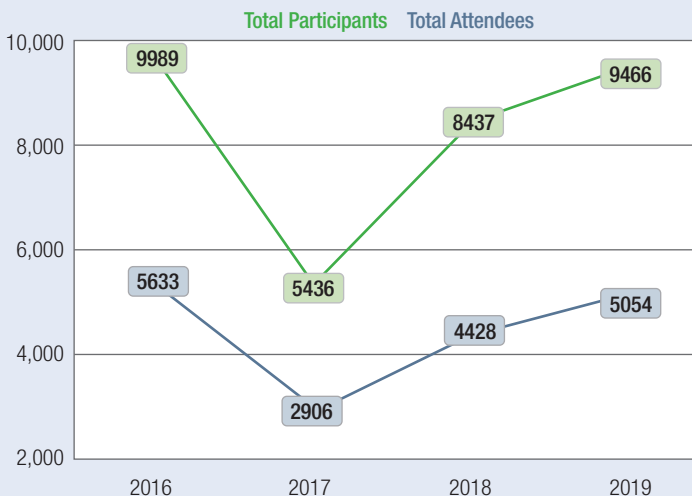
In the heart of Atlanta, the Georgia World Congress Center is at the forefront of the meeting industry, on the vanguard of event health and safety, and offers these features and benefits:

- Largest combined convention, sports, and entertainment campus in North America
- 220 acres anchored by Georgia World Congress Center, Centennial Olympic Park, and Mercedes-Benz Stadium
- 12,000 hotel rooms within walking distance
- 1.5 million square feet of prime exhibit space
- World's largest LEED certified convention center
- Ample meeting space for exhibitor meetings
- Branding opportunities within the facility
- Wi-Fi throughout the facility
- Inexpensive Public Transportation via Metropolitan Atlanta Rapid Transit Authority (MARTA) from Atlanta area and Hartsfield-Jackson Atlanta International Airport to GWCC/CNN Station (W-1)

Reserve your IMS exhibition booth today!

Attendee Snapshot

IMS Four Year Attendance Numbers



Why Become a Sponsor at IMS 2021?

Beyond the Booth:

Market to attendees throughout the convention center, inviting them to your booth on the show floor. Whether you are looking to promote a product, build your brand, or connect with customers, a sponsorship helps raise your profile. Our expert sales team can help you construct the sponsorship plan that best meets your marketing goals.

Contact your sales representative or exhibits@horizonhouse.com to discuss exhibit and sponsorship opportunities at IMS2021.

Exhibitor Benefits

Exhibitors will enjoy the following benefits before, during and after the conference:

Pre-Show:

- An IMS exhibitor console. Dedicated area to showcase your profile.
- Access to 2021 promotional opportunities
- Choice of hotel accommodations including hospitality suites and meeting space

On-Site:

- A listing in the official Conference Program/Exhibition Catalog
- Priority space selection for the IMS2022
- Access to discounted conference registrations
- General exhibit hall security service
- Daily aisle cleaning service

Post-Show:

- Post-event report with conference audit and attendee demographics

STANDARD EXHIBIT BOOTH

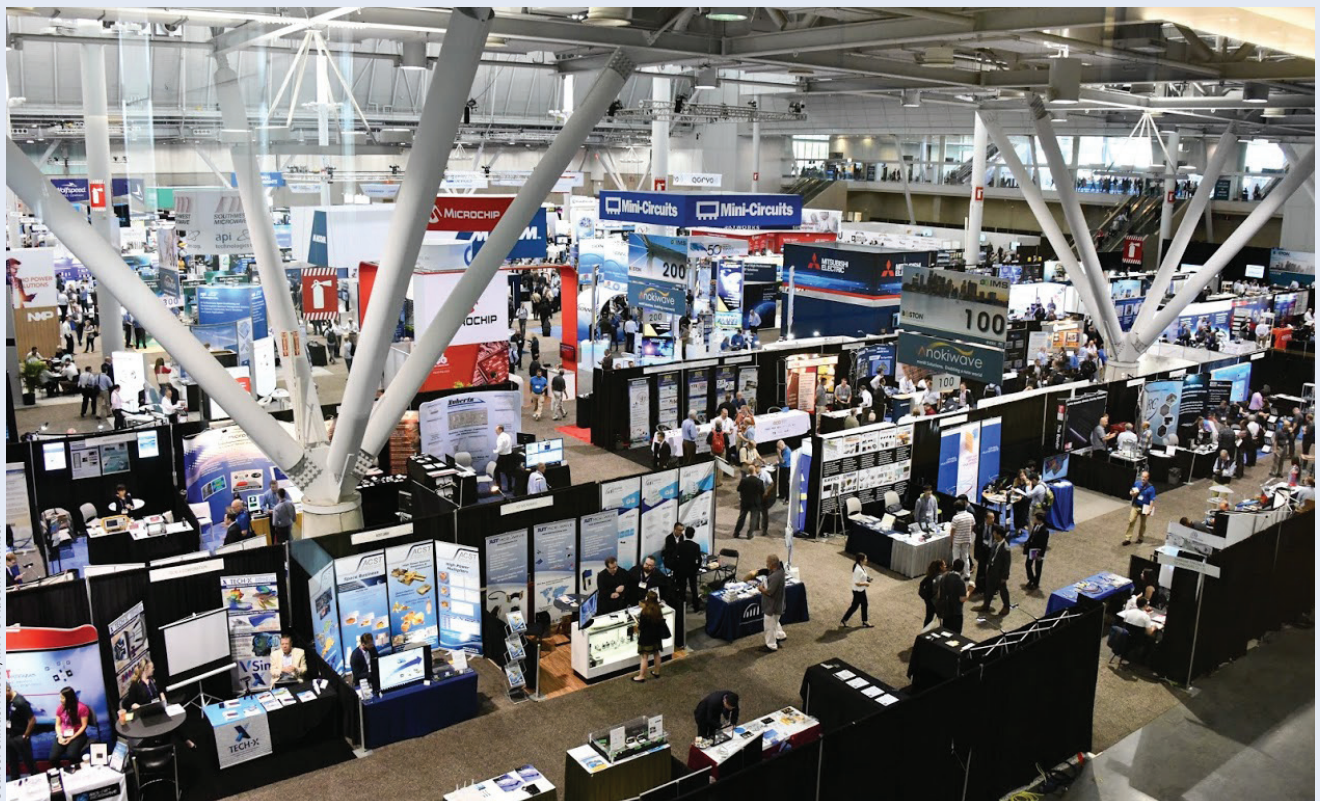
IMS2021 Exhibit Space is \$3,800 per 10x10 booth.

- Illuminated exhibit space with 8' high backwall drape if needed and 3' high side rails (in-line booths only).
- A 7" x 44" identification sign with the exhibitor's name and booth number (in-line booths only).
- Furnished booth packages and booth decor available in the Exhibitor Manual through the event decorator.

5G Pavilion

The 5G pavilion offers a special turnkey position on the show floor to introduce and showcase your 5G products. All participants receive the following for \$3,400:

- 6ft draped table, 2 chairs and electrical
- Identified as a 5G Pavilion participant on all 5G signage
- Promotional listing on the 5G web page, pages in the printed Conference Program/Exhibition Catalog
- Highlighted in IMS attendee promotions and featured on IMS website
- Option to lead a talk in the theater on 5G



Source: Samuel Auster, MTT-S AdCom member



IMS

Connecting Minds. Exchanging Ideas.

For details, visit: <https://ims-ieee.org/ims2021>



SALES REPRESENTATIVES

For General Inquiries

Call (781) 619-1994
or email
exhibits@horizonhouse.com

Eastern and Central Time Zones

Michael Hallman
Sales Manager
4 Valley View Court
Middletown, MD 21769
Tel: (301) 371-8830
FAX: (301) 371-8832
mhallman@horizonhouse.com

Pacific and Mountain Time Zones

Brian Landy
Western Reg. Sales Mgr.
(CA, AZ, OR, WA, ID, NV, UT, NM, CO, WY,
MT, ND, SD, NE & Western Canada)
144 Segre Place
Santa Cruz, CA 95060
Tel: (831) 426-4143
FAX: (831) 513-5444
blandy@horizonhouse.com

International Sales

Richard Vaughan
International Sales Manager
16 Sussex Street
London SW1V 4RW, England
Tel: +44 207 596 8742
FAX: +44 207 596 8749
rvaughan@horizonhouse.co.uk

Germany, Austria, and Switzerland

(German-speaking)
WMS.Werbe- und Media Service
Brigitte Beranek
Gerhart-Hauptmann-Street 33,
D-72574 Bad Urach
Germany
Tel: +49 7125 407 31 18
FAX: +49 7125 407 31 08
bberanek@horizonhouse.com

France

Gaston Traboulsi
Tel: 44 207 596 8742
gtraboulsi@horizonhouse.com

Israel

Dan Aronovic
Tel: 972 50 799 1121
aronovic@actcom.co.il

Korea

Young-Seoh Chinn
JES MEDIA, INC.
F801, MisahausD EL Tower
35 Jojeongdae-Ro
Hanam City, Gyeonggi-Do 12918 Korea
Tel: +82 2 481-3411
FAX: +82 2 481-3414
yschinn@horizonhouse.com

China

Shenzhen
Michael Tsui
ACT International
Tel: 86-755-25988571
FAX: 86-755-25988567
michaelt@actintl.com.hk

Shanghai

Linda Li
ACT International
Tel: 86-021-62511200
lindali@actintl.com.hk

Beijing
Cecily Bian
ACT International
Tel: +86 135 5262 1310
cecilyb@actintl.com.hk

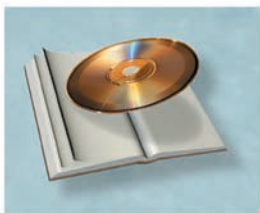
Hong Kong, Taiwan, Singapore

Mark Mak
ACT International
Tel: 852-28386298
markm@actintl.com.hk

Japan

Katsuhiko Ishii
Ace Media Service Inc.
12-6, 4-Chome,
Nishiiko, Adachi-Ku
Tokyo 121-0824, Japan
Tel: +81 3 5691 3335
FAX: +81 3 5691 3336
amskatsu@dream.com

CONNECTING FOR A SMARTER, SAFER WORLD



Book/Software Reviews

CMOS Loves 5G

■ Alfy Riddle

As CMOS has entered millimeter-waves, low-cost communications and radar applications have opened up. CMOS keeps pushing the limits, and *Millimeter-Wave Circuits for 5G and Radar*, edited by Gernot Hueber and Ali M. Niknejad, is very convincing about how well CMOS is pushing the frequency boundary. After an introductory chapter, the book splits into three parts: eight chapters on systems, four chapters on components, and a final chapter on fin field-effect transistors (FinFETs) and process technology. It is a fascinating tour of applications, critical components, and technology.

The book has 14 chapters and almost 30 different authors, representing a mix of universities, research centers, and businesses. Each chapter has a different lead author, which makes for a wide variety of perspectives. Almost all of the chapters have background, measurements, and design examples, which create a very practical work. With

Alfy Riddle (alfred.riddle@quanergy.com)
is with Quanergy Systems, Inc., Sunnyvale,
California, USA.

Digital Object Identifier 10.1109/MMM.2020.3035973
Date of current version: 11 January 2021

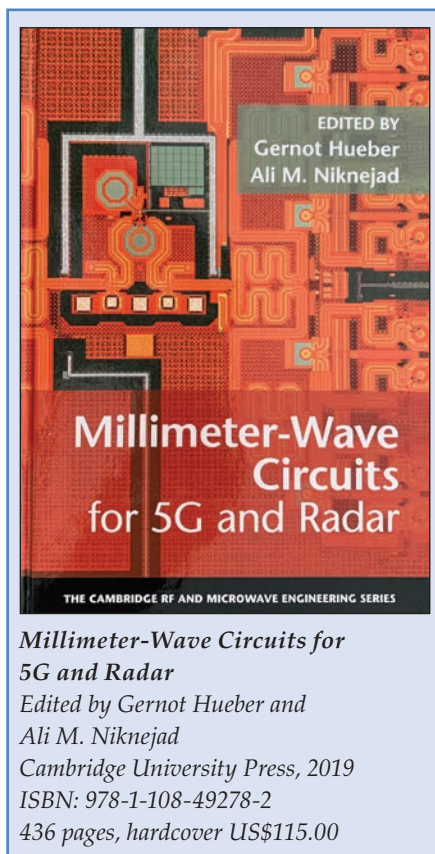
all that said, this book is not exactly coherent, as there is much overlap and some duplication. All in all, however, this is an excellent overview and

starting point for further study and work. I am sure you will enjoy it.

This book begins with a nice summary of 5G evolution from previous systems and a view toward automotive radars. The second chapter offers a very interesting overview, from high-level system goals to chip details and alternative methods. One minor issue is that the choice of symbols in some of the figures in several chapters makes it difficult to discern which line is which. Chapter 3 follows along the system theme with a good multiple input/multiple output (MIMO) overview.

The rest of the book gets further into circuit details. Chapters 4 and 5 focus on full duplex systems, cancellation of one's own transmitter at one's receiver, and circuit designs for realizing full duplex. This is where having chapters on similar subjects by different authors is a benefit, as it adds perspective. Chapter 4 has an extensive set of references, while Chapter 5 has many details on noise issues. Chapter 6 revisits MIMO from a packaging and antenna perspective and also covers spatial filtering.

Chapters 7 and 8 represent a transition from systems to chip details, with a focus on radar as applied to



*Millimeter-Wave Circuits for
5G and Radar*

Edited by Gernot Hueber and
Ali M. Niknejad
Cambridge University Press, 2019
ISBN: 978-1-108-49278-2
436 pages, hardcover US\$115.00

automotive and biometric systems. Frequency-modulated continuous-wave radar is covered, along with several chip architectures and even phase-locked loop (PLL) design. Measurements are included. Chapter 8 focuses on transceiver design, which reinforces the transition from systems to chips and gives a coherent background for individual circuits. Details on mixer design and calibration are covered as well.

The rest of the book is focused on circuit designs and devices. Chapter 9 reinforces Chapter 6's antennas discussion with more circuit details and measurements. Chapters 10–12 are all about frequency sources, with a tour of frequency synthesis, digital PLLs (including using time-to-digital converters), voltage-controlled oscillator design, and, of course, phase noise.

Once again, this book is full of practical details, and it would not be

complete without a chapter on power amplifier design. Chapter 13 provides a good overview, with measurements and many references. Finally, Chapter 14 offers a practical tour of FinFETs and how their differences and large gate-to-drain capacitance (C_{gd}) change one's designs. This book is an excellent and timely reference for anyone getting into this area or actively researching this field.



Correction

Due to a production error, the caption text for Figure 7 in [1] is incomplete. The correct

caption is included with Figure 7 here. We apologize for any confusion this may have caused.

Strategies for the estimation of digital predistortion linearization parameters," *IEEE Microw. Mag.*, vol. 21, no. 12, pp. 34–46, Dec. 2020. doi: 10.1109/MMM.2020.3023220.

Digital Object Identifier 10.1109/MMM.2020.3040092
Date of current version: 11 January 2021

Reference

[1] P. L. Gilibert, R. N. Braithwaite, and G. Montoro, "Beyond the Moore-Penrose inverse:

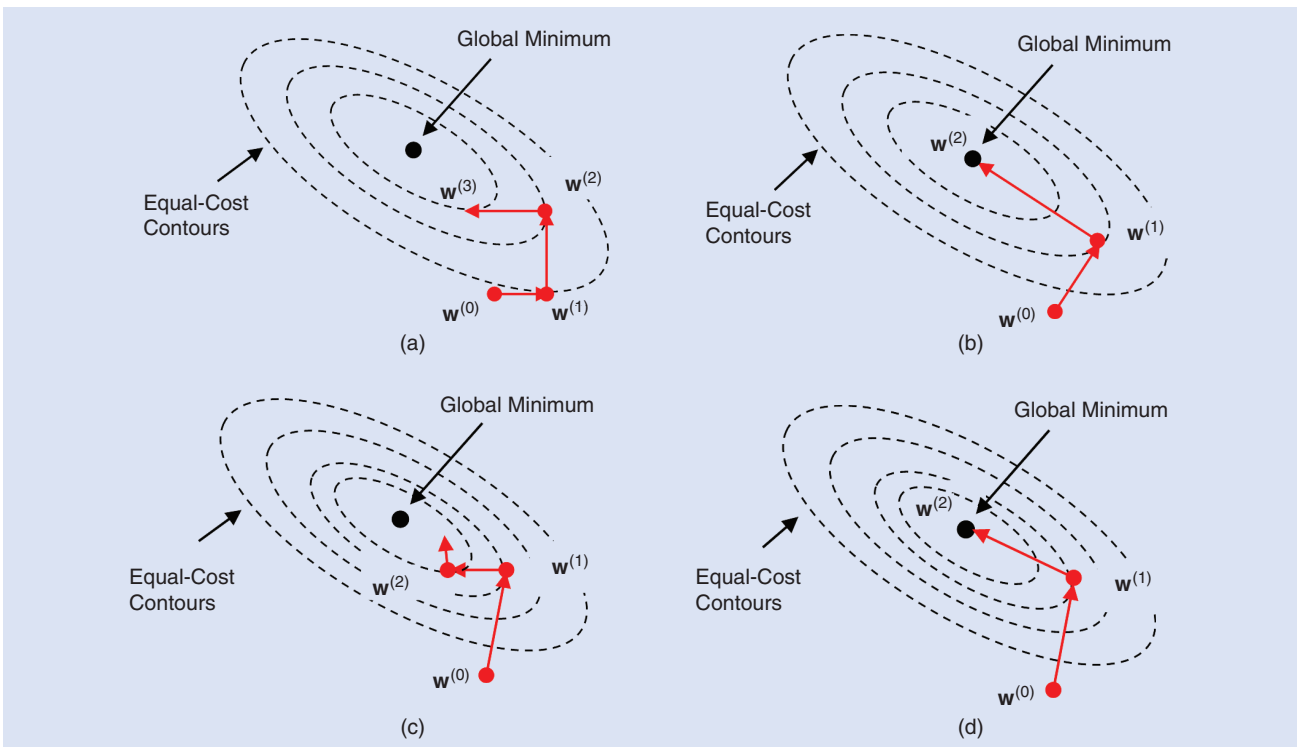


Figure 7. The descent trajectory, i.e., the sequence of directions selected, for different error-minimization methods. The (a) coordinate, (b) eigenvector, (c) gradient, and (d) conjugate gradient descents.



Education News

Continuing Our IEEE MTT-S Webinar Series

■ Robert H. Caverly, Michael C. Hamilton, and Rashaunda Henderson

The IEEE Microwave Theory and Techniques Society (MTT-S) Education Committee continues to offer high-quality webinars from experts in their respective fields through a series that started in 2016 [1]–[3]. These webinars have continued through 2020 and provided collaborative learning opportunities to our MTT-S membership as well as to the global microwave/RF community. The members of the MTT-S Education Committee are grateful to our webinar speakers for their efforts in preparing and delivering cutting-edge educational content through our popular MTT-S webinar series.

The current webinars scheduled for the first half of 2021 can be found in Table 1. These speakers represent a diverse group of leading subject-matter experts from around the globe, including current or emeritus Distinguished Microwave Lecturers. The past webinars,

Robert H. Caverly (r.caverly@ieee.org), editor-in-chief of IEEE Microwave Magazine, is with Villanova University, Villanova, Pennsylvania, USA. Michael C. Hamilton (mchamilton@auburn.edu) is with Auburn University, Auburn, Alabama, USA. Rashaunda Henderson (rmh072000@utdallas.edu) is with the University of Texas Dallas, Richardson, Texas, USA.

Digital Object Identifier 10.1109/MMM.2020.3037386

Date of current version: 11 January 2021

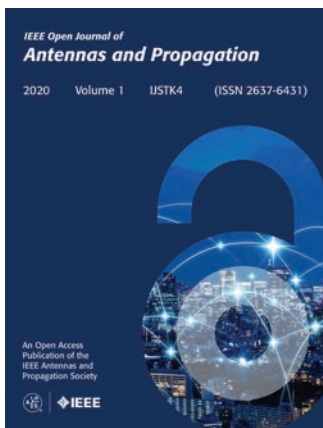


©SHUTTERSTOCK.COM/FABER14

as well as other MTT-S-related resources, can be found at the MTT-S Resource Center, <https://resourcecenter.mtt.ieee.org/>. Viewing of previous MTT-S webinars is free for MTT-S members. IEEE professional development hours are also available.

If you would like to be considered as a potential webinar speaker and present a topic of current interest to the MTT-S community in the 2022 webinar series, please send an email to either Dr. Hamilton or Dr. Henderson outlining your topic and





IEEE Open Journal of Antennas and Propagation

Full peer review | rapid publication | open access

The IEEE Open Journal of Antennas and Propagation (OJAP), the first gold fully open access journal of the IEEE Antennas and Propagation Society, accelerates the publication of rigorously peer-reviewed research from across the antennas and propagation field, augmented by immediate, worldwide, barrier-free access and maximum exposure. Having placed rigorous standards, innovation and openness at the heart of its publishing strategy, OJAP celebrates its one-year anniversary by delivering its niche and broader audience a 650-page yearly volume of the highest quality. The volume comprises 65 articles that cover the entire range from technical results and applied engineering innovations to topical review and perspective articles. Expanding article collections are featured in Special Sections, providing reference material on timely topics as well as future directions on developing fields.

2020 Volume highlights

Millimeter-wave Power Harvesting: A Review

M. Wagih, A. S. Weddell, and S. Beeby

Screen-Printed, Flexible, Parasitic Beam-Switching Millimeter-Wave Antenna Array for Wearable Applications

A. Meredov, K. I. Klionovski, and A. Shamim

Physics-Informed Deep Neural Networks for Transient Electromagnetic Analysis

O. Noakoasteen, S. Wang, Z. Peng, and C. Christodoulou

Eight-Element Compact UWB-MIMO/Diversity Antenna with WLAN Band Rejection for 3G/4G/5G Communications

M. S. Khan, A. Iftikhar, R. M. Shubair, A.-D. Capobianco, B. D. Braaten, and D. E. Anagnostou

Terahertz Antenna Array Based on a Hybrid Perovskite Structure

A. Abohmra, H. Abbas, M. Al-Hasan, I. B. Mabrouk, A. Alomainy, M. A. Imran, and Q. H. Abbasi

Patch Antenna and Antenna Array on Multilayer High-Frequency PCB for D-Band

A. Lamminen, J. Säily, J. Ala-Laurinaho, J. de Cos, and V. Ermolov

Analysis and Design of Checkerboard Leaky-Wave Antennas with Low Radar Cross Section

S. Ramalingam, C. A. Balanis, C. R. Birtcher, and S. Pandi

An Accurate Equivalent Circuit Model of Metasurface-Based Wireless Power Transfer Systems

D. Brizi, N. Fontana, S. Barmada, and A. Monorchio

Isolation Improvement of Two Tightly Coupled Antennas Operating in Adjacent Frequency Bands Using Filtering Structures

J. Guo, F. Liu, L. Zhao, G.-L. Huang, Y. Li, and Y. Yin

Bandwidth Enhancement Technique for Broadside Tri-Modal Patch Antenna

C.-Y. Chiu, B. K. Lau, and R. Murch

Eddy Current Modeling in Multiply Connected Regions Via a Full-Wave Solver Based on the Quasi-Helmholtz Projectors

T. L. Chhim, A. Merlini, L. Rahmouni, J. E. Ortiz Guzman, and F. P. Andriulli

Fast Semi-Analytical Design for Single-FSS-Layer Circuit-Analog Absorbers

X. Lv, S. J. Chen, A. Galehdar, W. Withayachumnankul, and C. Fumeaux

Microwave Detection of Brain Injuries by Means of a Hybrid Imaging Method

A. Fedeli, C. Estatico, M. Pastorino, and A. Randazzo

Techniques for Achieving High Isolation in RF Domain for Simultaneous Transmit and Receive

S. B. Venkatakrishnan, A. Hovsepian, A. Johnson, T. Nakatani, E. Alwan, and J. Volakis

Fast facts

	Submission to first decision	21 days		Content enrichment	Images, videos, podcasts
	Submission to publication	4-6 weeks		APC	\$1750, discounts available
	Article usage	33,000 downloads (until October 2020)		Creative Commons Attribution licenses	Plan S compliance

Submit your article today
<https://ieeeps.org/ieee-objap>

TABLE 1. Current MTT-S webinars scheduled for the first half of 2021.

2021 Webinar Dates	Title	Presenters	Affiliation
9 February	The Future of Battery-Free RF/Microwave Systems	Prof. Alessandra Costanzo	University of Bologna
11 March	Exploring Online Presentation Skills for Engaging Your Audience	Dr. John Bandler and Dr. Erin Kiley	McMaster University and Massachusetts College of Liberal Arts
13 April	Quantum Computing with Microwaves	Prof. Joseph Bardin	University of Massachusetts, Amherst
11 May	Power Amplifiers for High Efficiency Above 100 GHz	Prof. Jim Buckwalter	University of California, Santa Barbara
22 June	Measured System Point-Spread Functions Enable Real-Time Quantitative Imaging	Prof. Natalia Nikolova	McMaster University
13 July	Time-Varying Transmission Line (TVTL) for Broadband, Low Noise, Nonreciprocal, and Cross-Frequency RF Applications	Prof. Y. Ethan Wang	University of California, Los Angeles

providing a brief abstract, biography, and sample slides.

References

[1] R. K. Gupta and M. Hamilton, "MTT-S Education Committee Launches successful 2016 webinar series [Education News]," *IEEE Microw. Mag.*, vol. 17, no. 11, pp. 84–91, Nov. 2016. doi: 10.1109/MMM.2016.2601539.

[2] R. K. Gupta and M. C. Hamilton, "MTT-S 2017 webinar series: Another successful year of collaborative learning [Education News]," *IEEE Microw. Mag.*, vol. 19, no. 2, pp. 100–101, Mar./Apr. 2018. doi: 10.1109/MMM.2017.2781159.

[3] R. K. Gupta and M. C. Hamilton, "IEEE MTT-S 2018 webinar series: Speaker biographies and webinar abstracts [Education News]," *IEEE Microw. Mag.*, vol. 20, no. 3, pp. 93–100, Mar. 2019. doi: 10.1109/MMM.2018.2885672.



President’s Column (continued from page 11)

including *Intermodulation in Microwave and Wireless Circuits*, *Microwave and Wireless Measurement Techniques*, *White Space Communication Technologies*, and *Wireless Power Transmission for Sustainable Electronics*. He is the editor-in-chief of *Wireless Power Transfer Journal* (Cambridge University Press), an associate editor of *IEEE Microwave Magazine*, and a former associate editor of *IEEE Transactions on Microwave Theory and Techniques*. He is a member of the MTT-S AdCom, past chair of the IEEE Portuguese Section, past chair of MTT-S Technical Committees MTT-20 and MTT-11, and a member of Technical Committees MTT-24 and MTT-26.

He is vice chair of the International Union of Radio Science Commission A (Metrology Group). He received the 2000 Institution of Electrical Engineers Measurement Prize and has been a DML for the MTT-S.

AdCom Member Perspectives

The MTT-S has made a huge impact in my research life. Participating in the IEEE MTT-S International Microwave Symposium is an achievement in and of itself. I see the MTT-S as the RF and microwave hardware community. All new emerging hardware technologies have a voice in MTT-S conferences and journals. Participating in MTT-S meet-

ings and publishing in journals such as *IEEE Transactions on Microwave Theory and Techniques* and *IEEE Microwave Magazine* allow us to be among the technology visionaries who will shape our future. This is why I am motivated to be actively involved in improving awareness within IEEE of the importance of RF/microwave hardware design. Encouraging students and drawing engineers to participate in our conferences, meetings, and publications will allow them to recognize that the MTT-S is the true source of information and a driving force for hardware research within the engineering community.





IEEE MTT-S Resource Center

A premier collection of online technical webinars and related content for technical professionals.

MITT TO THE COMMUNITY



On-Demand Professional Development



Cost Effective and Convenient

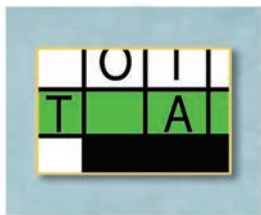


Library of Technical Resources



Visit resourcecenter.mttts.ieee.org





Enigmas, etc.

Turn-On Surge

■ Takashi Ohira

Last month's circuit scheme is shown again in Figure 1. Remember the sawtooth-like waveform, where a surge current flows from the charged capacitor into the transistor every time it turns on. Find how much power dissipation is caused by this surge current. Which of the following is correct? Note that f stands for the switching frequency: $f = 1/T$.

- a) fVV_{dc}^2
- b) $2fCV_{dc}^2$
- c) $4fCV_{dc}^2$
- d) $8fCV_{dc}^2$

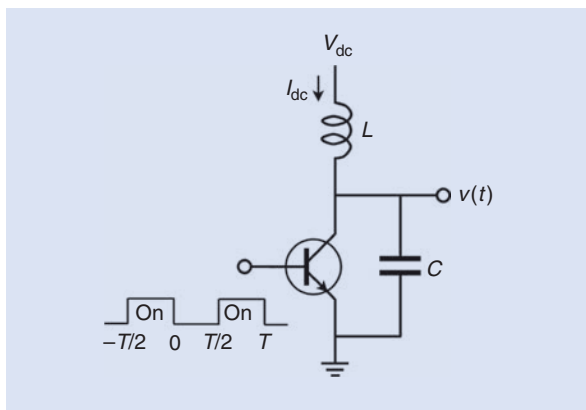


Figure 1. A switching transistor circuit scheme.

Takashi Ohira (ohira@tut.jp) is with the Toyohashi University of Technology, Toyohashi, Aichi, Japan. He is a Life Fellow of IEEE.

Digital Object Identifier 10.1109/MMM.2020.3035933
Date of current version: 11 January 2021

Solution to the January 2021 Puzzle

When voltage V_{dc} is applied to the circuit, the choke coil L conducts current I_{dc} , which charges capacitor C at a constant rate. This makes the output voltage a linearly increasing function of time as

$$v(t) = \frac{1}{C} \int_0^t I_{dc} dt = \frac{I_{dc}}{C} t. \quad (1)$$

From this calculation, we notice that C is indispensable to this circuit. If C were removed, $v(t)$ would steeply rise and possibly destroy the transistor when it turns off at $t = 0$.

The choke coil exhibits zero-ohm dc resistance; therefore, the average $v(t)$ for one cycle balances with the dc supply voltage V_{DC} ; that is,

$$V_{dc} = \frac{1}{T} \int_0^{T/2} v(t) dt = \frac{I_{dc}}{TC} \left[\frac{1}{2} t^2 \right]_0^{T/2} = \frac{TI_{dc}}{8C}. \quad (2)$$

Note that the integral is truncated halfway because $v(t)$ vanishes right after the transistor turns on at $t = T/2$. From (2), we can quickly find

$$I_{dc} = \frac{8CV_{dc}}{T}. \quad (3)$$

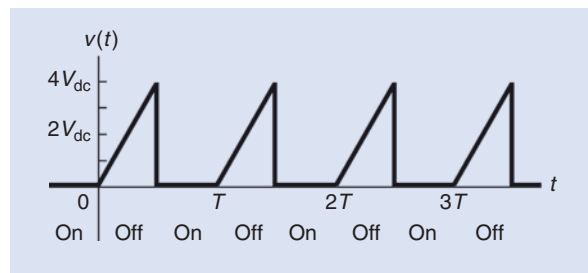


Figure 2. The output voltage waveform in the time domain.

This signifies the dc voltage–current relation of the switching circuit. Reflecting this relation to (1), the output voltage is determined as

$$v(t) = \frac{8V_{dc}}{T}t \quad (4)$$

during the OFF state $0 < t < T/2$.

Equation (4) indicates that the voltage starts from zero at $t=0$, linearly increases with t , and reaches its peak,

$$v(T/2) = \frac{8V_{dc}}{T} \frac{T}{2} = 4V_{dc} \quad (5)$$

at $t=T/2$. The voltage is kept at zero during the ON state because the capacitor C is held short-circuited by the transistor. This ON/OFF cycle is periodically repeated in every interval T , as shown in Figure 2. In conclusion, the output voltage waveform resembles a sawtooth. The correct answer to last month's quiz is c).

As the switch-mode operation can achieve an extremely high dc–RF power conversion efficiency, we could exploit this mode in power amplifiers for radio and wireless systems.

As the switch-mode operation can achieve an extremely high dc–RF power conversion efficiency, we could exploit this mode in power amplifiers for radio and wireless systems. However, if we employ the circuit as it is, the described sawtooth-like waveform will cause

two serious problems: heavy power loss and strong multiple harmonics (both due to the steep voltage drop down at the turn-on moment). We will explore a viable solution to these problems in forthcoming puzzles.



CMC
MICROSYSTEMS

Microelectronics

CAD
RF, antenna design and simulation tools, such as Ansys, Cadence, Keysight, Mentor Graphics, Synopsys, and more, and access to foundry PDKs

FAB
MPW, manufacturability checks, and custom prototype services. Global supply partnerships with GlobalFoundries, TSMC, AMS & ST

LAB
Prototype validation, test equipment, and development systems

www.CMC.ca/microelectronics

in | | f | | |



Conference Calendar

Editor's Note: Please check the website of each conference for any changes to paper or workshop deadlines or conference dates and modality (in person, virtual, or hybrid).

JANUARY 2021

2021 IEEE Radio and Wireless Week (RWW2021, Colocated with ARFTG)
17–20 January 2021
(Virtual Conference)

APRIL 2021

2021 IEEE 21st Annual Wireless and Microwave Technology Conference (WAMICON)
10–15 April 2021
Location: Sand Key, Florida, United States

MAY 2021

2021 IEEE MTT-S Latin America Microwave Conference (LAMC)
26–28 May 2021
Location: Cali, Colombia

JUNE 2021

2021 IEEE Wireless Power Transfer Conference (WPTC); 2021 IEEE PELS Workshop on Emerging Technologies: Wireless Power Transfer (WoW)
1–4 June 2021
Location: San Diego, California, United States

2021 IEEE Radio Frequency Integrated Circuits Symposium (RFIC)
6–8 June 2021
Location: Atlanta, Georgia, United States

2021 IEEE/MTT-S International Microwave Symposium—IMS 2021
6–11 June 2021
Location: Atlanta, Georgia, United States

2021 97th ARFTG Microwave Measurement Conference (ARFTG)
11 June 2021
Location: Atlanta, Georgia, United States

2021 32nd International Symposium on Space Terahertz Technology (ISSTT)
27 June–1 July 2021
Location: Baeza, Spain

JULY 2021

2021 Fourth International Workshop on Mobile Terahertz Systems (IWMTS)
5–6 July 2021
Location: Essen, Germany

2021 IEEE MTT-S International Conference on Numerical Electromagnetic and Multiphysics Modeling and Optimization (NEMO)
7–9 July 2021
Location: Limoges, France

IEEE MTT-S International Conference on Microwave Acoustics and Mechanics (IC-MAM)
19–21 July 2021
Location: Munich, Germany

AUGUST 2021

2021 IEEE 19th International Symposium on Antenna Technology and Applied Electromagnetics (ANTEM)
8–11 August 2021
Location: Winnipeg, Manitoba, Canada

2021 46th International Conference on Infrared, Millimeter and Terahertz Waves (IRMMW-THz)
29 August–3 September 2021
Location: Chengdu, China

OCTOBER 2021

2021 51st European Microwave Conference (EuMC), 2021 16th European Microwave Integrated Circuits Conference (EuMIC), and 2021 18th European Radar Conference (EuRAD)
11–15 October 2021
Location: London, United Kingdom



Digital Object Identifier 10.1109/MMM.2020.3035934
Date of current version: 11 January 2021



CALL FOR PAPERS

General Chair:

Andrés Navarro, Universidad Icesi
anavarrocadavid@ieee.org

General Co-Chair:

Felix Vega, Universidad Nacional, Colombia
fvegas@unal.edu.co

Technical Program Committee Chair:

Jose María Molina, Cartagena Polytechnic University,
Spain
josemaria.molina@upct.es

Technical Program Committee Co-Chair:

María Teresa Martínez-Ingles, University Center of
Defense, San Javier Air Force Base, Cartagena,
Spain
mteresa.martinez@tud.upct.es

Publications Chair:

Carlos Lozano, Universidad de Los Andes, Bogotá,
Colombia
calozanog@ieee.org

Financial Chair:

José David Cely, Universidad Distrital FJDC
j.d.cely@ieee.org

Webmaster:

Fabian Martínez, IEEE
fabianemartinez@ieee.org

Students Coordinator:

Dinael Guevara, Universidad Francisco de Paula
Santander, Colombia
dinaelgi@ufps.edu.co

Due to the COVID-19 Pandemic, IEEE MTT-S has approved changing the original dates of LAMC 2020, now celebrating it in May 26-28, 2021, in an attempt to make it face-to face, but keeping the possibility to going virtual. IEEE MTT-S reconfirmed Cali, Colombia, as the venue for the 3rd IEEE MTT-S Latin America Microwave Conference (now LAMC 2021). During the past decade, Cali has gained national and international recognition for its potential to become one of the most important cities in Latin America and the Pacific in terms of logistics, manufacturing and creative industry. Cali, main city of the Pacific region of Colombia, known as a commercial, service and cultural hub, offers a vivid and dynamic environment for creation of innovative solutions, a wide variety of economic sectors, including both small and large companies as well as agricultural industry, a growing ICT ecosystem and high-quality universities. Looking for synergy, LAMC 2021 will be co-located with IEEE Colcom 2021 (IEEE Colombian Conference on Communications and Computing). We encourage the submission of original, unpublished research focused on (but not limited to) the following topics of interest:

- Passive components, circuits and devices** (planar and nonplanar components and circuits, filters and multiplexers, tunable devices, and metamaterials).
- Active components and measurements systems** (RFICs & MMIC design, power amplifiers, linearization techniques, low-noise circuits, signal generation, conversion & control modules, linear and non-linear modeling and characterization).
- RF systems and applications** (microwave systems and front-ends industrial scientific and medical applications, navigation systems, intelligent transportation systems, imaging, sensors, wireless power transmission).
- Communication systems** (terrestrial, vehicular, satellite and indoor applications, wireless and cellular communication systems).
- Active antennas** (phase arrays, integrated antennas, smart antennas, digital-beam forming and MIMO).
- Signal-power integrity and high-speed digital techniques** (EM interference and compatibility, high speed interconnects, post-silicon validation techniques, power delivery networks, computer simulations and measurements).
- CAD techniques for RF and microwave engineering** (surrogate –based modeling and optimization, space mapping-based methods, model order reduction techniques, statistical analysis and design, EM based and multi physics design optimization, EM field theory, time and frequency-domain numerical techniques).

IMPORTANT DATES

Proposals for special sessions and tutorials:	December 20, 2020
Submission regular papers:	January 25, 2021
Notification:	March 1, 2021
Camera-ready	March 22, 2021
Author registration:	March 22, 2021

PAPER SUBMISSION

Papers submitted to LAMC 2021 will be peer reviewed and evaluated based on originality, quantitative contents, clarity, and interest to the audience. The review process will be single-blind. LAMC will use EDAS as the electronic paper management system. All accepted and presented papers will be published in the LAMC Conference Proceedings and submitted for inclusion in the IEEE Xplore Digital Library.

English will be the official language of the conference. Prospective authors are cordially invited to submit a three-page two-column manuscript (maximum 4 pages), following the instructions available at the conference website.

Advertisers Index

ADVERTISER	PAGE	URL	PHONE
Applied Interconnect	11	OnlineCables.com	
Cadence Design Systems	2	cadence.com/go/awr/try	
CMC Microsystems	77	www.CMC.ca/microelectronics	
Comsol	7	comsol.blog/microwave-filters	
Mini-Circuits	1, 9	www.minicircuits.com	+1 718 934 4500
Remcom	5	www.remcom.com/communications	+1 888 7 REMCOM
Sonnet Software	CVR 4	www.sonnetsoftware.com	+1 877 7 SONNET

445 Hoes Lane, Piscataway, NJ 08854

IEEE MICROWAVE MAGAZINE REPRESENTATIVE

Erik Henson
Naylor Association Solutions
Phone: +1 352 333 3443
Fax: +1 352 331 3525
ehenson@naylor.com

Digital Object Identifier 10.1109/MMM.2020.3043858

Are You Moving?

Don't miss an issue of this magazine—
update your contact information now!

Update your information by:

E-MAIL: address-change@ieee.org

PHONE: +1 800 678 4333 in the United States
or +1 732 981 0060 outside
the United States

If you require additional assistance
regarding your IEEE mailings,
visit the IEEE Support Center
at supportcenter.ieee.org.

IEEE publication labels are printed six to eight weeks
in advance of the shipment date, so please allow sufficient
time for your publications to arrive at your new address.



© IStockPhoto.com/BRIANAJACKSON



Conference Committees

General Chairs

Jenshan Lin, Univ. of Florida, USA
 Chris Mi, San Diego State Univ., USA

Technical Program Chairs

J.-C. Chiao, SMU, USA
 Amir Mortazawi, Univ. of Michigan, USA

Publications Chairs

Joe Qiu, Army Research Office, USA
 Changzhi Li, Texas Tech Univ., USA

Finance Chair/Treasurer

Aasrith Ganti, Philips, USA

Award and Competition Chairs

Zhizhang David Chen, Dalhousie Univ., Canada
 Simon Hemour, Univ. Bordeaux, France
 Zoya Popovic, Univ. of Colorado- Boulder, USA

Industry/Government Liaison Chairs

Christopher Rodenbeck, NRL, USA
 Souvik Dubey, Abbott Lab., USA
 Paul Jaffe, NRL, USA
 Chris Davlantes, Reach Labs, USA

Poster Chair

Hung Cao, UC, Irvine, USA

Website Chair

Ryan Miyamoto, Oceanit Laboratories, USA

Publicity Chair

Yanghyo Rod Kim, Stevens Inst. of Tech., USA

Member at Large

Ali Darwish, Johns Hopkins Univ., USA

WPTC Executive Committee

Alessandra Costanzo, Univ. of Bologna, Italy
 Nuno Borges Carvalho, U. of Aveiro, Portugal
 Dominique Schreurs, KU Leuven, Belgium
 Naoki Shinohara, Kyoto Univ., Japan
 Huib Visser, IMEC, Netherlands
 Ke Wu, École Polytechnique, Canada
 Goutam Chattopadhyay, NASA JPL, USA
 Jenshan Lin, Univ. of Florida, USA

Contact Information

WPTC2021@gmail.com

Important Dates

Deadline for paper submission:
 Jan. 15, 2021

Notification of acceptance:
 Feb. 28, 2021

Deadline for final manuscripts:
 March 31, 2021

The 2021 **IEEE Wireless Power Transfer Conference (WPTC)** will be held in San Diego on June 1-4, 2021, in parallel with the IEEE Workshop on Emerging Technologies: Wireless Power (WoW), in the **IEEE Wireless Power Week (WPW2021)**. WPW is the largest event in the world for wireless power research, financially co-sponsored by IEEE Microwave Theory and Techniques Society (MTT-S) and Power Electronics Society (PELS). WPW is technically co-sponsored by MTT-S, PELS, and Antenna Propagation Society (APS). The Wireless Power Transfer School, supported by the IEEE Wireless Power Transfer Project Initiative, will be held during the event.

WPTC2021 covers a wide range of topics related to wireless power technologies across the electromagnetic spectrum. In addition to high-quality technical sessions, the conference will feature keynote speeches, tutorials, workshops, student competition, and industry exhibitions.

Keynote Speakers

- Dr. Alex Lidow, CEO and Co-founder of Efficient Power Conversion
“Wireless Power 2.0: What will it take to get there and when will it happen?”
- Prof. James C. Lin, Professor Emeritus, Department of Electrical and Computer Engineering, University of Illinois at Chicago
“Safety of RF Wireless Power Transfer Technology”
- Dr. Paul Jaffe, Spacecraft Engineering Department/Space Electronics Systems Development, U.S. Naval Research Laboratory
“Wireless Power and Power Beaming”
- Dr. W. Bernard Carlson, Vaughan Professor of Humanities, Department of Engineering and Society, University of Virginia
“To get a Grip on the Earth and Shake it:’ Nikola Tesla’s Scheme for Wireless Power Transmission”

Conference Scope

- Theories and techniques for wireless power transfer
- Devices and systems for short-distance wireless power transfer
- Industrial applications, issues and regulations
- Microwave/mm-Wave wireless power transfer and RF energy harvesting
- Biomedical and healthcare applications
- Emerging techniques and applications



Visit the conference website (<https://wptc-ieee.org>) for details and updates.

SONNET® v17

17.56 is available now!

